



TESI DI DOTTORATO

UNIVERSITÀ DEGLI STUDI DI NAPOLI “FEDERICO II”

DIPARTIMENTO DI INGEGNERIA ELETTRICA  
E TECNOLOGIE DELL'INFORMAZIONE

DOTTORATO DI RICERCA IN  
INGEGNERIA ELETTRONICA  
E  
DELLE TELECOMUNICAZIONI

---

TECHNIQUES FOR INVERSE  
SYNTHETIC APERTURE RADAR  
IMAGING AND MONITORING OF  
DEFORMATION WITH DIFFERENTIAL  
INTERFEROMETRIC SYNTHETIC  
APERTURE RADAR

---

Carlo Noviello

Il Coordinatore  
del Corso di Dottorato  
Ch.mo Prof. Daniele RICCIO

Il Tutore  
Ch.mo Prof. Ernesto CONTE  
Il Co-Tutore  
Ch.mo Dr. Gianfranco FORNARO

XXVII Ciclo



*“I have no special talent.  
I am only passionately curious.”  
Albert Einstein*



# Contents

<b>List of Figures</b>	<b>XVIII</b>
<b>List of Tables</b>	<b>XIX</b>
<b>Introduction</b>	<b>1</b>
References . . . . .	8
<b>1 Inverse Synthetic Aperture Radar Imaging</b>	<b>9</b>
1.1 Synthetic Aperture Radar (SAR) and Inverse Synthetic Aperture Radar (ISAR) Concepts . . . . .	9
1.2 Fundamental of radar imaging . . . . .	12
1.2.1 Doppler Effect . . . . .	12
1.2.2 Radar backscattering from a point-like target . . . . .	14
1.3 Imaging Radar System . . . . .	16
1.4 Point Spread Function of ISAR system . . . . .	19
1.5 ISAR image Resolution . . . . .	22
1.5.1 Range Resolution . . . . .	22
1.5.2 Cross-Range and Doppler Resolution . . . . .	22
References . . . . .	25
<b>2 Inverse Synthetic Aperture Radar Image Processing</b>	<b>27</b>
2.1 ISAR processing background . . . . .	27
2.2 SAR and ISAR Range-Doppler processing . . . . .	29
2.3 ISAR Motion Compensation . . . . .	32
2.3.1 ISAR Translational Motion Compensation . . . . .	34
2.3.2 ISAR Rotational Motion Compensation . . . . .	36
2.3.3 ISAR Polar Formatting . . . . .	37
2.4 ISAR Image Autofocusing Techniques . . . . .	39
2.4.1 Image Contrast Based Autofocus . . . . .	40

References . . . . .	44
<b>3 Inverse Synthetic Aperture Radar Doppler Parameters</b>	
<b>Autofocus Technique</b>	<b>45</b>
3.1 ISAR Doppler Parameters Model . . . . .	46
3.2 Doppler Centroid Estimation . . . . .	48
3.3 Doppler Rate Estimation . . . . .	50
3.4 Doppler Parameters Estimation Algorithm for SAR Re- Focusing . . . . .	53
3.4.1 Numerical Results of refocusing SAR moving target	55
3.5 Doppler Parameters Estimation Algorithm for ISAR Static Sensor . . . . .	60
3.5.1 Numerical Results of focusing ISAR moving targets	62
3.6 Acknowledgment . . . . .	67
References . . . . .	70
<b>4 Synthetic Aperture Radar Principles and Interferome- try</b>	<b>71</b>
4.1 Synthetic Aperture Radar principle . . . . .	71
4.1.1 SAR processing . . . . .	75
4.1.2 SAR Image . . . . .	80
4.2 SAR Interferometry . . . . .	82
4.2.1 InSAR height sensitivity . . . . .	85
4.2.2 Decorrelation effects . . . . .	87
4.3 Differential SAR Interferometry . . . . .	89
4.3.1 Main limitation of DInSAR technique . . . . .	90
4.4 Multipass SAR Interferometry . . . . .	93
References . . . . .	98
<b>5 Integration of GPS-Derived Atmospheric Propagation Delay in DInSAR Data Processing</b>	<b>99</b>
5.1 Atmospheric Propagation Delay Characterization . . . . .	100
5.1.1 Hydrostatic Component Models . . . . .	101
5.1.2 Wet Component Models . . . . .	102
5.2 GPS Zenith Delay Estimation . . . . .	103
5.3 Impact of the Atmospheric Propagation Delay on Multi- pass DInSAR data . . . . .	105
5.4 Integration of GPS Tropospheric Delay Measurement in DInSAR Data Processing . . . . .	108

---

5.5	Experimental Results . . . . .	110
5.6	Acknowledgment . . . . .	122
	References . . . . .	125
<b>Appendix A</b>		<b>127</b>
<b>Appendix B</b>		<b>129</b>
<b>Conclusions and Future Developments</b>		<b>131</b>



# Acronym

**2-D** two-dimensional

**3-D** three-dimensional

**APD** Atmospheric Propagation Delay

**A-DInSAR** Advanced-DInSAR

**ALOS** Advanced Land Observation Satellite

**ASI** Italian Space Agency

**APS** Atmospheric Phase Screen

**CMRE** Centre for Maritime Research & Experimentation

**CPI** Coherent Processing Interval

**CNR** National Research Council

**CSK** Cosmo-SkyMed

**DEM** Digital Elevation Model

**DoY** Day-Of-Year

**DPEA** Doppler Parameter Estimation Algorithm

**DInSAR** Differential SAR Interferometry

**DLR** German Space Agency

**EM** ElectroMagnetic

**EMBA** Entropy Minimization Based Autofocus

<b>ESD</b>	Enhanced Spatial Differences
<b>FT</b>	Fourier Transform
<b>FMCW</b>	Frequency Modulated Continuous Wave
<b>FFT</b>	Fast Fourier Transform
<b>GPS</b>	Global Positioning System
<b>IC</b>	Image Contrast
<b>ICBA</b>	Image Contrast Based Autofocus
<b>ICBT</b>	Image Contrast Based Technique
<b>IDFT</b>	Inverse Discrete Fourier Transform
<b>IFT</b>	Inverse Fourier Transform
<b>IFFT</b>	Inverse Fast Fourier Transform
<b>ISAR</b>	Inverse Synthetic Aperture Radar
<b>InSAR</b>	SAR Interferometry
<b>IREA</b>	Institute for the Electromagnetic Sensing of the Environment
<b>JPL</b>	Jet Propulsion Laboratory
<b>LOS</b>	Line-of-Sight
<b>MLBF</b>	Multi-Look Beat Frequency
<b>PFA</b>	Polar Format Algorithm
<b>PS</b>	Persistent Scatterer
<b>PSF</b>	Point Spread Function
<b>PSI</b>	Persistent Scatterer Interferometry
<b>PRF</b>	Pulse Repetition Frequency
<b>PPP</b>	Prominent Point Processing
<b>PGA</b>	Phase Gradient Autofocus

---

<b>PhU</b>	Phase Unwrapping
<b>PWV</b>	Precipitable Water Vapour
<b>PFA</b>	Polar Format Algorithm
<b>PRI</b>	Pulse Repetition Interval
<b>RCS</b>	Radar Cross Section
<b>RD</b>	Range Doppler
<b>RDA</b>	Range Doppler Algorithm
<b>RT</b>	Radon Transform
<b>RCM</b>	Range Cell Migration
<b>RCMC</b>	Range Cell Migration Correction
<b>RMTRC</b>	Residual Motion Through Resolution Cells
<b>SAR</b>	Synthetic Aperture Radar
<b>SBAS</b>	Small BAseLine Subset
<b>SCR</b>	Signal to Clutter Ratio
<b>SLC</b>	Single Look Complex
<b>SNR</b>	Signal to Noise Ratio
<b>SRTM</b>	Shuttle Radar Topography Mission
<b>SVD</b>	Single Value Decomposition
<b>TMC</b>	Translational Motion Compensation
<b>TDX</b>	Tandem-X
<b>ZHD</b>	Zenith Hydrostatic Delay
<b>ZWD</b>	Zenith Wet Delay
<b>ZD</b>	Zenith Delay



## List of Symbols

$\Omega$	Angular velocity
$\gamma$	Angular acceleration
$X$	Antenna footprint
$B_x$	Azimuth Bandwidth
$x$	Azimuth Direction
$\Delta x$	Azimuth Resolution
$\rho$	Backscattering or Reflectivity function
$\alpha$	Chirp rate
$v$	Cross-Range direction
$\Delta r_{cr}$	Cross-range Resolution
$B_D$	Doppler Bandwidth
$\Delta f_D$	Doppler Resolution
$f_{DC}$	Doppler centroid
$f_{DR}$	Doppler rate
$\varepsilon$	Elevation angle
$f_D$	Doppler Frequency
$f_0$	Carrier Frequency
$r_g$	Ground range direction
$\Delta r_g$	Ground range resolution
$z$	Height variable
$m_h$	Hydrostatic mapping function
$\varphi$	Interferometric phase
$W_{cloud}$	Liquid (cloud) water content
$\phi$	Latitude
$\theta$	Looking angle
$b_{\perp}$	Orthogonal baseline
$T_{obs}$	Observation Interval
$b_{//}$	Parallel baseline
$L$	Physical antenna length along the azimuth direction

$v_s$	Platform velocity
$P$	Pressure
$\Delta T$	Pulse duration
$T_{PRI}$	Pulse Repetition Interval
$a_r$	Radial Acceleration
$r$	Range SAR direction
$\varsigma$	Range ISAR direction
$f_{samp}$	Range sampling frequency
$B_W$	Signal Bandwidth
$\lambda$	Signal wavelength
$L_{sa}$	Synthetic Aperture length
$\Delta r$	Slant range resolution
$SD$	Slant tropospheric Delay
$b$	Spatial baseline
$c$	Speed of light
$T$	Temperature
$v$	target velocity
$v_r$	Radial velocity
$e$	Water vapour partial pressure
$m_w$	Wet Mapping function
$ZD$	Zenith Delay
$ZHD$	Zenith Hydrostatic Delay
$ZWD$	Zenith Wet Delay

# List of Figures

1.1	Commonly SAR modes . . . . .	10
1.2	From SAR Spotlight configuration to ISAR configuration	11
1.3	From an ISAR configuration to a circular SAR configuration	11
1.4	Synthetic aperture formed by non cooperative target motion	12
1.5	Geometry of a radar and a rotating target . . . . .	16
1.6	ISAR raw data matrix formation. . . . .	18
1.7	The concept of ISAR system. . . . .	18
2.1	Equivalence between the SAR spotlight imaging system and an ISAR imaging rotating target. . . . .	28
2.2	The process of SAR imaging of a stationary point target.	29
2.3	SAR imaging in range-azimuth domain and ISAR imaging in range-cross-range domain. . . . .	30
2.4	SAR raw data matrix formation. . . . .	30
2.5	Block diagram of SAR range-Doppler algorithm. . . . .	31
2.6	Block diagram of ISAR range-Doppler algorithm. . . . .	32
2.7	Geometry of a moving target with respect to radar. . . . .	33
2.8	De-ramping procedure . . . . .	35
2.9	De-ramping effects. . . . .	35
2.10	Radar and a rotating target. . . . .	36
2.11	Polar reformatting mapping from polar to rectangular do- main. . . . .	37
2.12	ISAR Polar Format Algorithm (PFA) block diagram . . .	38
2.13	PFA effect for rotational motion compensation. . . . .	39
2.14	Range Profiles of the received signal after range-compression.	42
3.1	Reference geometry of the ISAR system with the sensor centred reference system and the reference system moving solidly with the target. . . . .	46

3.2	Slow-Time and Doppler Frequency relation. . . . .	51
3.3	Block diagram of Doppler Parameters Estimation for SAR re-focusing non-cooperative targets. The dashed line connections indicate that the estimated Doppler rate is updated at each iteration. . . . .	54
3.4	First unfocused ship cropped from the SLC image of CSK in Spotlight mode. . . . .	57
3.5	First focused ship with Doppler Parameters Estimation Algorithm. . . . .	57
3.6	First focused ship with Image Contrast Based Technique. . . . .	58
3.7	Second unfocused ship cropped from the SLC image of CSK in spotlight mode. . . . .	59
3.8	Second focused ship with Doppler Parameters Estimation Algorithm. . . . .	59
3.9	Second focused ship with Image Contrast Based Technique. . . . .	60
3.10	Block diagram of Doppler Parameters Estimation and compensation for focusing non-cooperative targets for static ISAR system. . . . .	61
3.11	Range-Doppler Frequency Modulated Continuous Wave (FMCW) radar data. . . . .	62
3.12	View of the test site area in the Gulf of La Spezia (Italy). . . . .	63
3.13	First unfocused ship cropped from the radar data in Polarization HH and HV . . . . .	64
3.14	First focused ship with Doppler Parameter Estimation Algorithm (DPEA) in Polarization HH and HV . . . . .	64
3.15	First focused ship with Image Contrast Based Technique (ICBT) in Polarization HH and HV . . . . .	65
3.16	First unfocused ship cropped from the radar data in Polarization VV and VH . . . . .	66
3.17	First focused ship with DPEA in Polarization HH and HV . . . . .	66
3.18	First focused ship with ICBT in Polarization VV and VH . . . . .	67
4.1	Radar side-looking imaging geometry . . . . .	72
4.2	Chirp signal . . . . .	74
4.3	Synthetic aperture principle . . . . .	75
4.4	Block diagram of SAR focusing operations . . . . .	80
4.5	Layover effect . . . . .	81
4.6	SAR geometry in the plane orthogonal to the flight direction with a single sensor: schematic picture of the layover . . . . .	82

---

4.7	Interferometric acquisition geometry . . . . .	84
4.8	ESAR interferogram relevant to the Stromboli volcano superimposed to the 3D model of topography . . . . .	86
4.9	(left side) A temporal multilook SAR image of the Naples (Italy) bay area (average of 30 CSK images); (center) An interferogram and (right side) the corresponding coher- ence map . . . . .	88
4.10	(left side) Adaptive spatial filtered interferogram and (right side) the corresponding coherence map . . . . .	89
4.11	DInSAR geometry (zero baseline configuration) . . . . .	90
4.12	DInSAR geometry (no zero baseline configuration), where it has been introduced also the atmospheric effect due to possible inhomogeneities of the atmospheric refraction index, which is responsible of an incorrect estimation of the deformation signal. . . . .	91
5.1	Diagram schematically showing the observations of points located at different heights on the ground in two passes of the SAR system. . . . .	106
5.2	Block diagram of the compensation procedure. . . . .	109
5.3	Distribution of the GPS stations (red dots) overlaid on a DEM of L'Aquila area. . . . .	112
5.4	Atmospheric (zenith) wet delays measured by two GPS stations; on the horizontal axis are reported the days from the 1st Jan. 2009 . . . . .	113
5.5	Upper image: GPS-derived atmospheric signal for a cer- tain acquisition time (October 5, 2009). Bottom image: plot of the estimated Global Positioning System (GPS) delay over the different stations with respect to the height 2009 . . . . .	114
5.6	Plots of the estimated GPS delay over the different sta- tions with respect to the height. The different images correspond to different days . . . . .	115

- 5.7 Postseismic interferogram (April 20, 2009 and July 2, 2009) before (upper image) and after (lower image) the compensation of the atmospheric phase delay from GPS data. Azimuth is vertical and is approximately coincident with the S-N direction, range is horizontal and is approximately coincident with the W-E direction: the area covered is of about  $40 \text{ km} \times 40 \text{ km}$ . . . . . 116
- 5.8 Postseismic velocity maps, overlaid on a grayscale Digital Elevation Model (DEM), corresponding to the Differential SAR Interferometry (DInSAR) processing of the ASCENDING COSMO-SkyMed dataset (a) without and (b) with the GPS-aided compensation module. The axes report longitude and latitude values of the imaged area. . 117
- 5.9 (Upper image) The same postseismic velocity map of 5.9(b) corresponding to the GPS-aided processing overlaid to a DEM in grayscale; (middle image) the same as the upper image but for the velocity map of Figure 5.9(a) corresponding to the result obtained without the integration of GPS measurements; (bottom image) distribution of the GPS stations on the 3-D map in which colors encode the height according to hypsometric tints. The axes report longitude and latitude values of the L'Aquila area. . . . . 118
- 5.10 Postseismic velocity maps, overlaid on a grayscale DEM, corresponding to the DInSAR processing of the DESCENDING COSMO-SkyMed dataset (a) without and (b) with the GPS-aided compensation module. The axes report longitude and latitude values of the imaged area. . . . . 120
- 5.11 (Upper image) The same postseismic velocity map of Figure 5.10(b) corresponding to the GPS-aided processing overlaid to a DEM in grayscale; (middle image) the same as the upper image but for the velocity map of Figure 5.10(a) corresponding to the result obtained without the integration of GPS measurements; (bottom image) distribution of the GPS stations on the 3D map in which colors encode the height according to hypsometric tints. The axes report longitude and latitude values of the imaged area. . . . . 121

# List of Tables

3.1	SAR Image Specification . . . . .	56
3.2	Comparison Parameters for Image 1 . . . . .	58
3.3	Comparison Parameters for Image 2 . . . . .	60
3.4	Sensor Specifications. . . . .	63
3.5	Comparison Parameters for I case study Polarization HH	65
3.6	Comparison Parameters for I case study Polarization HV	65
3.7	Comparison Parameters for II case study Polarization VV	67
3.8	Comparison Parameters for II case study Polarization VH	67
5.1	Description of the dataset acquired by the COSMO-SkyMed constellation in ascending mode. Temporal and spatial baselines are measured with respect to the acquisition of August 2, 2009. The spatial baselines refer to the perpendicular baselines exploited to compute the interferograms; they are measured in meters [m]. Temporal baselines are measured in days [d] elapsed from the reference acquisition.	111
5.2	Description of the dataset acquired by the COSMO-SkyMed constellation in descending mode. Temporal and spatial baseline are measured with respect to the acquisition of 21st July 2009. The spatial baselines refer to the perpendicular baselines exploited to compute the interferograms and are measured in meters [m]. Temporal baselines are measured in days [d] elapsed from the reference acquisition.	119



# Introduction

The term “remote sensing”, first used in the United States in the 1950s by Ms. Evelyn Pruitt of the U.S. Office of Naval Research, is now commonly used to describe the science of identifying, observing, and measuring an object without coming into direct contact with it. This process involves the detection and measurement of radiation at different wavelengths reflected or emitted from distant objects or materials, by which they may be identified and categorized by class/type, substance, and spatial distribution. The instruments involved in remote sensing science can be divided into two groups: (1) passive and (2) active. Passive instruments detect natural energy that is reflected or emitted from the observed scene; passive instruments sense only the radiation emitted by the object being viewed or reflected by the object from a source other than the instrument. Reflected sunlight is the most common external source of radiation sensed by passive instruments. On the other hand, active instruments provide their own energy (electromagnetic radiation) to illuminate the object or scene they observe. They send a pulse of energy from the sensor to the object and then receive the radiation that is reflected or backscattered from that object. Scientists use many different types of active remote sensors. The most popular and the most attractive active sensor which had a huge spread in the last decades is the Radar (Radio Detection and Ranging). Radar is capable of detecting, tracking and imaging targets with high accuracy at long range distance, day and night, and in all weather condition. Mainly because of these reasons, radar has been widely used for military and civil purposes, such as, wide-area surveillance, air defense and weapon control, high-resolution imaging, remote sensing of the environment, weather and earth observation, air traffic control, vehicle collision avoidance and cruise control, harbor and river traffic surveillance, and industry automation [1–4].

In the last years, the growing interest in the field of homeland secu-

rity and the risk monitoring, associated with natural and human induced hazards, has boosted the development of advanced radar techniques for generating high resolution radar images. In this context, the latest scientific researches led to the born of a new radar technology: the Synthetic Aperture Radar (SAR) sensor. SAR is an active microwave sensor, usually mounted on satellites or aircraft. The SAR sensor, moving along a track, transmits and receives impulses in such a way an improvement of the resolution along the flight direction can be obtained by exploiting the principle of antenna synthesis, i.e. of synthesizing an antenna whose size along the moving direction (azimuth) is much greater than the real onboard antenna. In this way is possible to generate microwave images with spatial resolutions of the order of meters even by satellite, which are comparable to the optical systems. On the other hand, a larger aperture can be also synthesized based on the hypothesis that the target moves while the radar remains stationary called Inverse Synthetic Aperture Radar (ISAR). In order to extract high-resolution images for both SAR and ISAR systems what really matter is the relative motion between the sensor and the target and collecting data from different aspect angles [5]. The huge potentiality of such a system has become a very attracting feature of modern radar that aims at providing more detailed geometric information about the target of interest.

In this thesis two relevant issues for radar remote sensing have been addressed by exploiting both SAR and ISAR techniques:

- focusing of moving targets using the ISAR imaging technique;
- correction of the atmospheric propagation delay in multipass Differential SAR Interferometry.

With regard to the first issue, it has been analyzed the problem of focusing ISAR non cooperative targets. When the target is not cooperating, the ISAR system, unfortunately, does not know the trajectory performed by the target; therefore, in order to perform high resolution radar image of the moving target, the spectral distortions introduced by the relative motion between the sensor and the target has to be compensated [6]. Hence, the system must necessarily estimate the target motion parameters. In literature, several algorithms have been developed to estimate these motion parameters; f.i. by implementing exhaustive search algorithms which try to maximize or minimize mathematical cost function based on the contrast or the entropy of the radar image. These

approaches allow to obtain well focused radar images, but, the computational load performances are not sufficient to ensure the use of these techniques in real time applications even if these techniques are performed by exploiting convex optimization tools.

In this thesis, it has been proposed a novel and computational efficient technique for estimating target motion parameters based on Doppler signal parameters, namely: the Doppler centroid and the Doppler rate which are directly related to the target radial velocity and acceleration [7]. This new technique, called Doppler Parameters Estimation Algorithm (DPEA), has been developed and tuned by testing it with ISAR simulated data. Subsequently, the DPEA technique has been applied for refocusing moving targets in SAR images. Classical SAR processing is based on the assumption that the illuminated area is static, or better targets are all moving with the same velocity, during the synthetic aperture formation [8]. The assumption that the targets in the illuminated area do not move during the data acquisition must hold to provide accurately focused SAR images. Nevertheless, in some scenarios, moving targets may be present in the illuminated scene. For such targets the mismatch between the target doppler history and the doppler history pertinent to the whole scene used in the reference function induces first of all an azimuth shift, thus providing an incorrect location of the target in the SAR image, and secondly it generates a defocusing of the target. This is the case of ground vehicles, ships and any other moving targets that may be of interest in some applications. Therefore, it has been proposed an ISAR add on algorithm based on Doppler parameter estimation technique which estimates the residual target motion parameters due to the relative motion between the target and the sensor. The proposed algorithm has been tested with a dataset of maritime targets acquired by the spaceborne COSMO-SkyMed constellation. Then, a novel approach for focusing moving target acquired by a static ISAR sensor has been proposed. The proposed ISAR autofocus algorithm exploits a new iterated version of the Doppler parameters estimation tool described before. In fact, the new version of the algorithm try to minimize the residual component of the Doppler centroid and the Doppler rate by iterating the estimation procedure until the residual error is less than a preset threshold. The novel algorithm has been tested with a real dataset acquired by a static sensor, and, the results have been compared with those obtained with the well known Image Contrast Based

Technique which has been used as benchmark.

The second issue regards the development of a novel technique for the integration of Global Positioning System (GPS) measurements of atmospheric phase delay within the multipass interferometric SAR processing chain [9]. SAR imaging allows representing the observed scene into the *azimuth-range* plane. Obviously, this is not sufficient to unambiguously locate the targets, i.e. to estimate their height with respect to a reference plane. In fact, similarly to a common optical image, a (single) SAR image is a two-dimensional projection of the scene and it is not sufficient to determine the 3-D location of the objects. Using the technique known as SAR Interferometry (InSAR), by comparing two images acquired from slightly different positions (spatial baseline) it is possible to obtain 3-D images of the Earth's surface, measuring the topography. When images are acquired in different times (temporal baseline), using the Differential SAR Interferometry (DInSAR) technique, it is possible to measure the changes of the Earth's surface [10]. DInSAR data are affected by many factors that cause the presence of spurious phase signals which act as error sources, thus, impacting, if not properly accounted for, the quality of the final deformation results. One of the main error source for DInSAR is the variation between the two acquisition of the atmospheric phase delay. Variations of the atmospheric propagation delay (APD) introduce spatially correlated error sources, which cannot be easily identified and separated by the useful deformation signal on single interferograms: APD impacts the accuracy of the final product derived from few acquisitions. Modern interferometric SAR techniques are based on the joint use, or better, on the stacking of multipass SAR data and mitigate the effects of APD variation by filtering in accordance with its spatio-temporal statistical characterization of the noise source. In fact, by assuming APD contributions to be spatially correlated and temporally uncorrelated, the signal component can be discriminated from the deformation signal component [11]. Typically, erroneous APD estimations may in principle impact the evaluation of weak linear deformation components such as, for instance, those typically observable in the interseismic phase over faults. Even more important is to note that the presence of APD corrupts the use of the multitemporal DInSAR techniques in emergency situations: in these cases, typically only few acquisitions are available and therefore APD temporal filtering becomes critical. These motivations have recently stimulated again the research

in the use and integration of SAR data with information acquired by other instruments. In this thesis, it has been investigated the possibility to integrate the measurements of the atmospheric phase delay obtained by a dense GPS network onto the DInSAR processing chain by implementing a robust assimilation via a least square approach. It has been derived a linear model of the variation of the atmospheric phase delay with the height corresponding to a stratified atmosphere, and, then, the coefficients of this linear model are evaluated by minimizing the mean square error between the model and the GPS measurements [12]. The algorithm has been tested with data acquired during the L'Aquila earthquake emergency, adopted by ASI as a priority acquisition program of COSMO-SkyMed constellation on the area hit by the Mw 6.3 earthquake, which struck L'Aquila on April 6, 2009, to support the Italian Department of Civil Protection (DCP) for the emergency phase.

The thesis is organized as follows:

- In Chapter 1, the concept of the radar imaging system based on synthesizing aperture induced by the relative motion between the target and the sensor has been introduced; then, the ISAR system model and the ISAR Point Spread Function with the relative system resolutions are derived in order to evaluate the performance of the ISAR system.
- In Chapter 2, firstly, the ISAR image formation process has been considered for focusing cooperative targets, subsequently, it has been addressed the problem of focusing non cooperative target. In this case, the most important ISAR autofocus algorithms have been introduced with particular emphasis with the well known Image Contrast Based Autofocus which is considered as the autofocus reference technique.
- In Chapter 3, a novel and efficient ISAR autofocus technique based on Doppler parameters signal is described. In particular, the estimation techniques of Doppler centroid and Doppler rate from the ISAR signal model has been derived. The Doppler parameters estimation technique has been firstly adopted for refocusing moving target in SAR image, and, then, is tested also for focusing moving targets acquired by a static ISAR sensor. The results obtained by the proposed ISAR autofocus technique for two different case studies have been compared with those obtained by the image contrast

based technique.

- In Chapter 4, the SAR system principles and the SAR impulse response function have been described; subsequently, the SAR Interferometry concept and the Differential SAR interferometry technique for monitoring the Earth surface is illustrated with emphasis on the impact of the limitation of these techniques caused by the atmospheric phase delay.
- In Chapter 5, it has been discussed a procedure for the mitigation of atmospheric propagation delay in multipass Differential SAR Interferometry based on the integration of data of GPS systems, which carry out measurements with large observation angles diversity practically in continuous time. The proposed algorithm allows a robust assimilation of the GPS atmospheric delay measurements in the multipass DInSAR processing and founds on a linear approximation with the height of the atmospheric delay corresponding to a stratified atmosphere. In this Chapter are also present the results obtained by testing the proposed algorithm on post-seismic deformation occurring in the area of L'Aquila, hit by a critical seismic sequence in 2009.

Finally conclusions and possible future developments are discussed.

# References

- [1] M. Skolnik, *Radar Handbook*. McGraw Hill Press, 2008.
- [2] F. Ulaby, R. K. Moore, and A. K. Fung, “Microwave remote sensing: Active and passive, vol. iii, volume scattering and emission theory, advanced systems and applications,” *Inc., Dedham, Massachusetts*, pp. 1797–1848, 1986.
- [3] M. A. Richards, J. Scheer, W. A. Holm *et al.*, *Principles of modern radar: basic principles*. SciTech Pub., 2010.
- [4] C. Oliver and S. Quegan, *Understanding synthetic aperture radar images*. SciTech Publishing, 2004.
- [5] J. L. Walker, “Range-doppler imaging of rotating objects,” *Aerospace and Electronic Systems, IEEE Transactions on*, no. 1, pp. 23–52, 1980.
- [6] V. C. Chen and M. Martorella, *Inverse Synthetic Aperture Radar Imaging Principles, Algorithms and Applications*. Shitech Publishing, 2014, vol. 1.
- [7] C. Noviello, G. Fornaro, and M. Martorella, “Focused sar image formation of moving targets based on doppler parameter estimation,” *Geoscience and Remote Sensing, IEEE Transactions on*, vol. 53, no. 6, pp. 3460–3470, 2015.
- [8] R. Lanari and G. Fornaro, “A short discussion on the exact compensation of the sar range-dependent range cell migration effect,” *IEEE Transactions on Geoscience and Remote Sensing*, vol. 35, 1997.
- [9] N. D’Agostino, G. Fornaro, R. Giuliani, C. Noviello, D. Reale, and S. Verde, “Gps aided atmospheric phase delay mitigation in differential sar interferometry: Experiences from the 2009 l’aquila earthquake.” in *IGARSS*, 2013, pp. 1853–1856.
- [10] R. F. Hanssen, *Radar interferometry: data interpretation and error analysis*. Kluwer Academic Publisher, 2001, vol. 1.

- [11] P. Berardino, G. Fornaro, R. Lanari, and E. Sansosti, "A New Algorithm for Surface Deformation Monitoring Based on Small Baseline Differential SAR Interferograms," *IEEE Trans. Geosci. Remote Sens.*, vol. 40, no. 11, pp. 2375–2383, Nov. 2002.
- [12] G. Fornaro, N. D'Agostino, R. Giuliani, C. Noviello, D. Reale, and S. Verde, "Assimilation of gps-derived atmospheric propagation delay in dinsar data processing," *Selected Topics in Applied Earth Observations and Remote Sensing, IEEE Journal of*, vol. 8, no. 2, pp. 784–799, Feb 2015.

# Chapter 1

## Inverse Synthetic Aperture Radar Imaging

*Inverse Synthetic Aperture Radar is a powerful technique for imaging moving targets in the range-Doppler (or range-cross-range) domain. Range is defined as the axis parallel to the direction of propagation from radar toward the target, cross-range is defined as the axis perpendicular to the range direction. An ISAR image has the ability to successfully display the dominant scattering centers on the target. ISAR processing is normally used for the identification and classification of targets. The classical two-dimensional (2-D) ISAR image is constructed by collecting the scattered field for different look angles and Doppler histories. Although ISAR processing is similar to SAR processing, ISAR imaging procedure has some conceptual differences when compared to the SAR imagery.*

### 1.1 SAR and ISAR Concepts

Synthetic Aperture Radar processing coherently combines signals obtained from sequences of small apertures acquired at different viewing angles to synthesize a very large aperture [1,2]; the sensor is usually mounted on a moving platform, generally an aircraft or satellite, although other carries, such as helicopters and ground based rails [3].

The most common modes operated in SAR are the strip-map mode and the spotlight mode. In the strip-map mode, the antenna beams bears on a fixed direction relative to the moving direction of a platform as illustrated in Figure 1.1(a). When the platform moves, an area strip is swept over. If the antenna direction is off the perpendicular of the flight path, this mode is referred to as squinted strip-map SAR. The strip-map mode can generate long strip of illumination of the terrain. In the spotlight mode, differently from the strip-

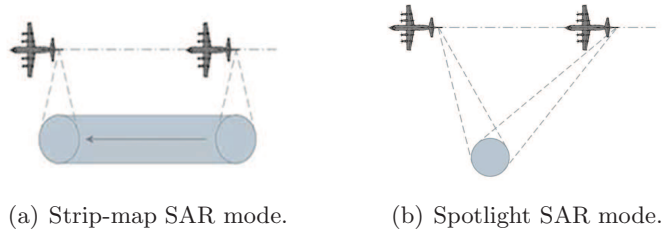


**Figure 1.1:** Commonly SAR modes

map mode, the antenna has a narrower beam and points to the same patch area when the physical aperture moves through the length of the synthetic aperture, as shown in Figure 1.1(b). This mode typically generates images of smaller scenes at a finer resolutions. The azimuth resolution is determined by the angular variation spanned during the formation of the synthetic aperture, and the size of the imaged area is determined by the antenna beamwidth.

To reconstruct the radar image of a target from a sequence of returned echoes, it is required that each returned signal must be obtained with a different view of the target, thus, a relative rotation between the radar and the target is necessary for creating different aspect angles of the target, such that each radar transmitted signal will capture a different view of the target. Now, it should be paid attention to the relative motion between the radar platform and the target. It means that the motion is not necessarily produced by a moving platform; in fact, if the radar is stationary and the target moves with respect to it, an improvement in cross-range resolution can be also obtained [4,5]. To emphasize the concept of relative motion, one could argue that whether the configuration called *stationary target and moving platform* or *stationary platform and moving target* really depends on where the reference coordinate system is placed: the former occurs by placing the reference system on the target and the latter by placing the reference system on the radar. According to this view, the differences between SAR and ISAR would depend only on where the reference system is placed. Such a concept is depicted in Figure 1.2(a), where a spotlight SAR configuration is transformed into an ISAR configuration by moving the reference system from the target to the radar.

Conversely, the same concept may be argued by starting with a controlled ISAR configuration, such as the turntable experiment. In the turntable configuration, the radar antenna is fixed on the ground (typically mounted on a turret) and the target is placed on a rotating turning table, as depicted in Figure 1.3(a). By moving the reference system from the radar to target, a circular SAR geometry can be enabled, as depicted in Figure 1.3(b), where the reference system is placed determines the type of configuration (i.e. SAR or ISAR configuration), but in practice a subtle yet significant detail exists that

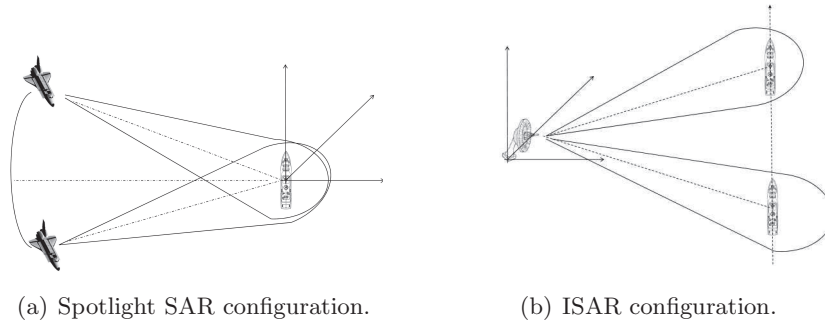


**Figure 1.2:** From SAR Spotlight configuration to ISAR configuration

substantially defines the difference between SAR and ISAR. This difference

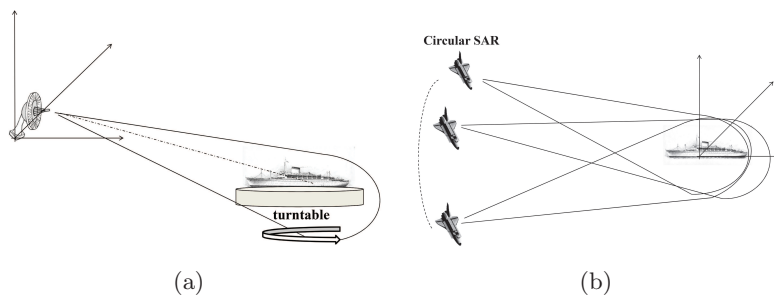


**Figure 1.3:** From an ISAR configuration to a circular SAR configuration

depends not on the placement of the reference system (this may be arbitrary to avoid affecting the system physically) but it depends on the target's cooperation. To better explain this concept, one may place the reference system on the target and if such a target moves with respect to the radar with unknown motion parameters; it is usually considered a non cooperative target, and so, the synthetic aperture formed during the coherent processing interval differs from that produced by an expected controlled motion of the platform, such as a turntable experiment; thus, the SAR image formation that follows would be based on an erroneously predicted synthetic aperture and lead to the formation of a defocussed image. A pictorial example of a synthetic aperture formed by a non cooperative motion of the target's motion is shown in Figure 1.4(a), where the unknown and non cooperative motion of the target generates an unpredictable synthetic aperture as shown in Figure 1.4(b). At this moment, it is very important to say that the detail of whether the target is

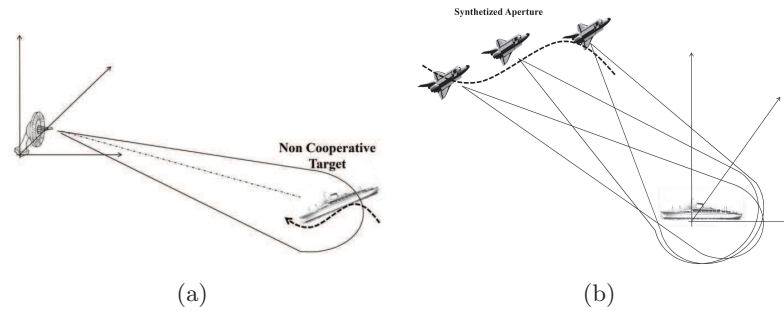


**Figure 1.4:** Synthetic aperture formed by non cooperative target motion

cooperative, it presents a number of issues, which are strictly related to the reason that for ISAR is important to determine the relative motion between the radar and the target and, thus, to form radar images of non cooperative targets. In fact, the synthetic aperture formed by an arbitrary target's motion with respect to the sensor is also unknown. This means that the position of the synthesized aperture sensors elements are not known a priori. Since SAR image processing is based on such a knowledge, it should say that any SAR image formation algorithm may not be successfully applied to form a focused image of non cooperative target. Furthermore, in cases where both radar and target are moving, if the target's motion is unknown by the radar, the SAR image processing would fail again. Generally, in cases where the radar platform is stationary and the target's motion is non cooperative, novel and different ISAR image algorithms should be applied instead of using classical SAR processing.

## 1.2 Fundamental of radar imaging

In this section I will focus on some imaging fundamentals concepts before introducing the ISAR system in its details. Some of the concepts such as coherency, Doppler effect and round trip delay, are common to the radar experts but they are introduced to establish the notation that I am going to use in this work.

### 1.2.1 Doppler Effect

Radar transmits a signal to a target and receives an echo from it. Based on the time delay of the received signal, radar can measure the range of the target. If the target is moving, the frequency of the received signal will be shifted from the frequency of the transmitted signal, this physical effect is known as the

*Doppler effect.* The Doppler frequency shift is determined by the radial velocity of the moving target, that is the component of the target velocity along the Line-of-Sight (LOS) direction. The Doppler frequency shift is usually measured by evaluating the Fourier spectrum of the signal and measuring the peak component which indicates the Doppler frequency induced by the radial velocity of the target. To accurately track the phase information in the radar received signals, the radar transmitter must be driven by a highly stable frequency source to fully maintain phase coherency. In typically radar application, the velocity of a target,  $v$ , is much slower than the speed of wave propagation  $c$  (i.e.  $v \ll c$ ). Generally for monostatic radar systems, the Doppler frequency generated by a moving target is expressed as follow:

$$f_D(t) = -f_0 \left[ \frac{2v_r(t)}{c} \right], \quad (1.1)$$

where  $f_0$  is the transmitted carrier frequency,  $v_r$  is the radial velocity of the target, and  $t$  is the time variable. When the target is moving away from the radar, its velocity component is defined as positive, as a consequence, the Doppler shift becomes negative. Assuming a model for the radar received signal as follows:

$$S_R = A \cos[2\pi(f + f_D)t] = A \cos[2\pi ft + \phi(t)], \quad (1.2)$$

where  $A$  is the amplitude of the received signal,  $\phi(t) = 2\pi f_D t$  is the phase shift on the received signal due to the target motion. In the following, I will consider a coherent demodulator with in-phase (I) and quadrature (Q) channels, which allows the full phase information to be retrieved from the signal. By mixing with the transmitted signal

$$S_T = \cos(2\pi ft), \quad (1.3)$$

the output of the I-channel mixer is

$$S_R(t)S_T(t) = \frac{A}{2} \cos[4\pi ft + \phi(t)] + \frac{A}{2} \cos \phi(t). \quad (1.4)$$

After low-pass filtering, the I-channel output becomes

$$I(t) = \frac{A}{2} \cos \phi(t). \quad (1.5)$$

By mixing with the  $90^\circ$  phase shifted transmitted signal

$$S_T^{90^\circ}(t) = \sin(2\pi ft), \quad (1.6)$$

the output of the Q-channel mixer is

$$S_R(t)S_T^{90^\circ}(t) = \frac{A}{2} \sin[4\pi ft + \phi(t)] - \frac{A}{2} \sin \phi(t). \quad (1.7)$$

After low-pass filtering, the Q-channel output becomes

$$Q(t) = \frac{A}{2} \sin \phi(t). \quad (1.8)$$

By combining the I and Q outputs, a complex signal can be formed as follows:

$$S_D(t) = I(t) + jQ(t) = \frac{A}{2} \exp[-j\phi(t)] = \frac{A}{2} \exp(-j2\pi f_D t) \quad (1.9)$$

Thus the Doppler frequency shift  $f_D$  can be estimated from the complex signal,  $S_D(t)$ , by using a frequency measurements tool. Because frequency is determined by time derivative of the phase function, the phase difference,  $\phi(t)$ , between the received and the transmitted signal is used to estimate the Doppler frequency shift,  $f_D$ , of the received signal:

$$f_D(t) = \frac{1}{2\pi} d\phi(t)/dt. \quad (1.10)$$

From the estimated Doppler frequency, the radial velocity of the target is determined by

$$v_r = \frac{\lambda}{2} f_D = \frac{c}{2f} f_D, \quad (1.11)$$

where  $\lambda = c/f$  is the wavelength of the transmitted frequency. Here, the dependence on the time variable,  $t$ , has been omitted for the sake of simplicity.

### 1.2.2 Radar backscattering from a point-like target

The radar backscattering from a point-like target can be easily simulated. Assuming to exactly know the initial location and the target's motion parameters in each time instant; based on the system geometry, the received signal can be easily formulated. Suppose the radar transmits a sequence of narrow rectangular pulses at the carrier frequency  $f_0$ , and with a pulse width,  $\Delta T$ , and a Pulse Repetition Interval (PRI),  $T_{PRI}$ , the radar baseband signal reflected from a point target can be expressed as:

$$S_B(t) = \sum_{n=1}^N \sigma^{1/2} \text{rect} \left[ \frac{t - nT_{PRI} - 2R(t)}{c\Delta T} \right] \exp \left[ \frac{-j4\pi f_0 R(t)}{c} \right], \quad (1.12)$$

where  $\sigma$  is the Radar Cross Section (RCS) of the target,  $N$  is the number of the received pulses,  $R(t)$  is the distance from the radar to the point target at time  $t$  (the time dependence of this term will be clarified later), and the rectangular function  $\text{rect}$  is defined as

$$\text{rect}(t) = \begin{cases} 1 & |t| \leq \Delta T/2 \\ 0 & |t| > \Delta T/2. \end{cases} \quad (1.13)$$

For high-resolution and unambiguous range and Doppler measurements, ISAR signals must have wide bandwidth and satisfy certain requirement for the selection of its Pulse Repetition Frequency (PRF). To have wide bandwidth, a multifrequency or a modulated continuous wave signal should be used, such as stepped-frequency signal, the linear frequency modulation signal, and a train of modulated pulses. To have high Doppler frequency measurement, the PRF must be sufficient high to avoid Doppler ambiguities. Similarly, to measure a target to a long distance, the PRF must be lower enough to avoid range ambiguities. In general, multiple PRFs can be used to resolve the range and Doppler ambiguities. When a radar transmits a signal  $s_T(t)$ , the received signal  $S_R(t)$  returned from the target, is proportional to the transmitted signal with a round-trip delay  $s_T(t - \tau)$  and scaled by the reflectivity function  $\rho$  of the target,

$$S_R(t) \propto \rho s_T(t - \tau) = \rho \exp\{j2\pi f(t - \tau)\} \quad (0 \leq t \leq T), \quad (1.14)$$

where  $T$  is the total signal time duration,  $\rho$  the target reflectivity function and  $f$  the transmitted frequency of the signal. The round-trip delay  $\tau$ , is determined by the distance of the target  $R$ , and the speed of light  $c$ :

$$\tau = \frac{2R}{c}. \quad (1.15)$$

When the target is moving with a radial velocity  $v_r$ , the radar signal must travel along a shorter or a longer distance, depending on the projection of the target velocity along the LOS to reach the target. The signal backscattered from the target to the radar at the time instant  $t - \tau(t)/2$ , and the round-trip delay is time-varying. The radar must have a waveform suitable to the required function of the radar. FMCW signal is a typical modulation scheme; other commonly schemes include the stepped-frequency waveform, pulse Doppler waveform and coherent pulse (amplitude, phase and frequency), modulation waveform. The simplest signal waveform is the continuous wave with a carrier frequency  $f_0$ ;

$$S_T(t) = A \cdot \exp\{j2\pi f_0 t\}. \quad (1.16)$$

The relative received signal:

$$S_R(t) = A_R \cdot \exp\{j2\pi f_0(t - \tau)\}, \quad (1.17)$$

If the target is moving, the received signal becomes:

$$S_R(t) = A_R \cdot \exp\{j2\pi(f_0 + f_D)(t - \tau)\}, \quad (1.18)$$

where  $f_D$  is the Doppler frequency shift.

### 1.3 Imaging Radar System

The relative motion between the radar and a target makes it possible to view the target at different aspect angles. The image generated by the the relative rotation is called the motion-induced image and it is usually represented in the Range Doppler (RD) domain. The concept of RD imaging was proposed in [6–8] when dealing with radar imaging of a rotating target. The global or space-fixed system  $(\Sigma, Y)$  and the local or body-fixed system  $(\varsigma, v)$ , which is rigidly fixed in the body, are the two coordinate systems commonly used to describe a target with motion as shown in Figure 1.5. For simplicity, I gave a 2-D representation of the geometry reference system. I will assume that the radar is in the origin of a global reference system and the target’s origin point is located in its geometric centre and I assume that the target rotates around the vertical axis  $z$  of the local reference system, with an angular rotation rate equal to  $\Omega(t) = \Omega + \gamma t$ , where  $\Omega$  is the angular velocity and  $\gamma$  is the angular acceleration. It’s worth pointing out that the assumption of

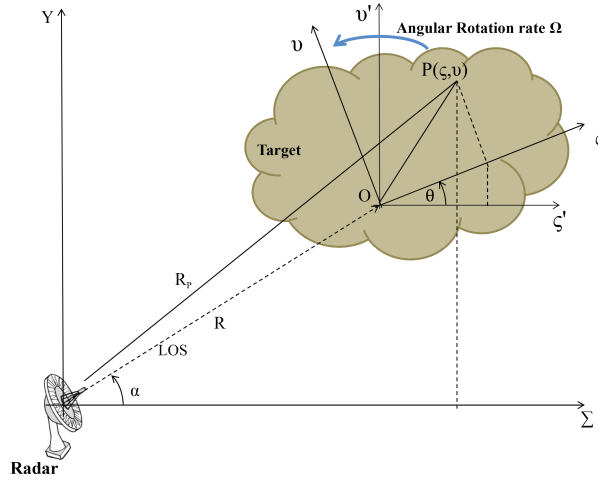


Figure 1.5: Geometry of a radar and a rotating target

constant acceleration is a reasonable approximation that holds in the case of short observation intervals. To describe the rotation of the target, another reference system  $(\varsigma', v')$  is introduced, which is parallel to the global  $(\Sigma, Y)$  reference system fixed on the sensor, with the same origin of the local body-fixed reference system  $(\varsigma, v)$ . Given the range distance  $R$ , by simple geometric consideration, the distance between the sensor and a generic point on the target,  $P(\varsigma, v)$ , becomes approximately

$$R_P(t) \cong R(t) + \varsigma \cos[\theta(t) - \alpha] - v \sin[\theta(t) - \alpha]. \tag{1.19}$$

The radar signal baseband version, backscattered from the generic point  $P$ , is a function of  $R_P$  as follows:

$$S_P(t) = \rho(\varsigma_P, \nu_P) \exp\{-j2\pi f[2R_P(t)/c]\}, \quad (1.20)$$

where  $\rho(\varsigma_P, \nu_P)$  is the reflectivity density function of the point scatterer  $P$ , and  $R_P(t)$  is time dependent. Based on the returned signal from a single point scatterer, the returned signal from the target can be represented as the integration of the returned signals from all scatterers that belong to the target:

$$S_R(t) = \iint \rho(\varsigma, \nu) \exp\left[-j\frac{4\pi f}{c}R_P(t)\right] d\varsigma d\nu. \quad (1.21)$$

For a target that has both translational and rotational motion and assuming that the azimuth angle  $\alpha$  is equal to zero, the range of a point scatterer at  $(\varsigma, \nu)$  becomes

$$S_R(t) = e^{-j4\pi f \frac{R(t)}{c}} \iint \rho(\varsigma, \nu) \exp\{-j2\pi[\varsigma f_\varsigma(t) - \nu f_\nu(t)]\} d\varsigma d\nu, \quad (1.22)$$

where  $f_\varsigma(t)$  and  $f_\nu(t)$  can be seen as two components of the frequency,  $f$ , and defined by

$$f_\varsigma(t) = \frac{2f}{c} \cos \theta(t) \quad (1.23)$$

and

$$f_\nu(t) = \frac{2f}{c} \sin \theta(t). \quad (1.24)$$

The backscattered signal (1.22) can also be expressed in terms of wavenumber  $k = 2\pi f/c$ :

$$S_R(t) = e^{-j4\pi f \frac{R(t)}{c}} \iint \rho(\varsigma, \nu) \exp\{-j2[\varsigma k_\varsigma(t) - \nu k_\nu(t)]\} d\varsigma d\nu, \quad (1.25)$$

where the two wavenumber components are determined by

$$k_\varsigma(t) = \frac{2\pi f}{c} \cos \theta(t) = k \cos \theta(t) \quad (1.26)$$

and

$$k_\nu(t) = \frac{2\pi f}{c} \sin \theta(t) = k \sin \theta(t). \quad (1.27)$$

During the Coherent Processing Interval (CPI), if the range function  $R(t)$ , is exactly known, the phase term due to the target's motion  $\exp[-j4\pi f R(t)/c]$  can be perfectly removed by multiplying the demodulated backscattered signal by the complex conjugate of this term. Such an operation is typically known as *radial motion compensation*, and the signal obtained after such operation is usually named *motion compensated signal*. When the radar transmits a sequence of

$N$  signals and the received signal of each transmitted signal has  $M$  samples, the collected raw data can be rearranged as a two dimensional  $M \times N$  matrix which is typically known as the delay time or fast-time ( $t_m$ , with  $m = 1, 2, \dots, M$ ) and pulses or slow-time ( $t_n$ , with  $n = 1, 2, \dots, N$ ) matrix. Because the fast time is related to the range, the raw data are also said to be in the range and pulses domain. Figure 1.6 describes how the 2-D radar raw data are arranged in the range (fast-time or time delay) and pulses (slow-time) domains. Figure

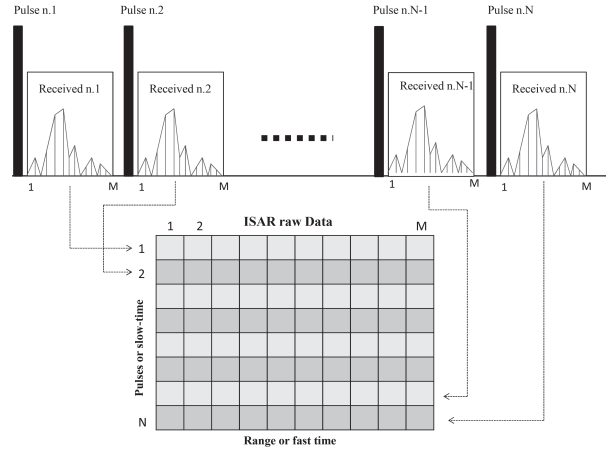


Figure 1.6: ISAR raw data matrix formation.

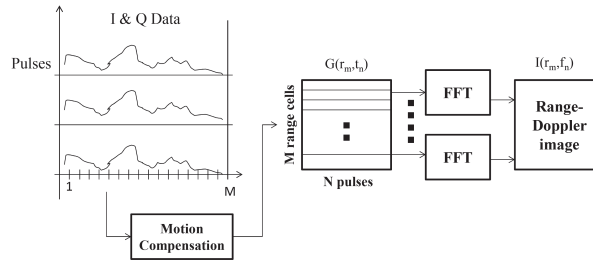


Figure 1.7: The concept of ISAR system.

1.7 illustrates the concept of an ISAR imaging system. The radar transmits a sequence of  $N$  pulses. For each transmitted pulse, the total number of range cells,  $M$ , is determined by the maximum range covered and the size of range cell or bin. Conversely, the total number of pulses,  $N$ , during a given CPI determines the Doppler resolution. After pulse compression I-Q downconversion in the radar receiver, the baseband complex I and Q data are organized into an  $M \times N$  two-dimensional complex matrix, which consists of  $N$  range profiles,

where each range profile has  $M$  range cells. Range profile represents the energy distribution of the received signal as a function of range. Magnitude peaks of the range profile indicate range locations of dominant scatterers. In a range profile, if one or more magnitude peaks are detected at certain range cells, it indicates that one or more dominant scatterers have been detected at the corresponding locations. Then, by applying the motion compensation procedure, the aligned-range profiles,  $G(r_m, t_n)$ , can be obtained, where  $m = 1, 2, \dots, M$ , and  $n = 1, 2, \dots, N$  as shown in Figure 1.7. The Fourier based image formation takes the Fourier transform at each range cell along  $N$  pulses and generates an  $N$ -point Doppler spectrum called the Doppler profile. Finally, by adjoining the Doppler spectra for each of the  $M$  range cells, the  $M \times N$  range-Doppler image is formed:

$$I(r_m, f_{Dn}) = FFT_n \{G(r_m, t_n)\}, \quad (1.28)$$

where  $FFT_n$ , denotes the fast Fourier operation with respect to  $n$ . The radar range-Doppler image,  $I(r_m, f_{Dn})$ , represents the target's reflectivity,  $\rho(\zeta, \nu)$ , mapped onto the range-Doppler plane.

## 1.4 Point Spread Function of ISAR system

In any Radar imaging system, the antenna emits ElectroMagnetic (EM) waves with the desired beam pattern, and the backscattered signals are exploited to form the image of the object of interest. The most important parameter of any imaging system is its spatial resolution, which is defined as the minimum distance at which two different objects are detected by the system as two different images of objects. Generally, the spatial resolution of a radar imaging system is determined by the length of the transmitted pulse and the antenna beamwidth. The pulse length determines the range resolution in the direction of the LOS. The antenna pattern determines the cross-range (or azimuth) resolution in the direction perpendicular to the radar LOS. Thus, the generated images are composed of rectangular resolution cells, whose sides are given by a range cell and a cross-range or Doppler cell. To achieve high range resolution, the transmitted signal should have a very short duration and high power peak. The backscattered signal is processed through the pulse compression technique by convolving the signal with the matched filter to compress the pulse length [9].

The mathematical model of a radar imaging system is composed of different system properties. The main important property is the reflectivity function  $\rho(u, v)$  of an object observed by the radar system. The expected output of the radar imaging system is the image  $I(\zeta, \nu)$ , which can be obtained by convolving the impulse response function and the reflectivity function as

$$I(\zeta, \nu) = \iint \rho(u, v) \cdot h(\zeta - u, \nu - v) du dv. \quad (1.29)$$

If the system impulse response becomes at 2-D delta Dirac function,  $h(\zeta, \nu) = \delta(\zeta, \nu)$ , then the image becomes equal to the object reflectivity function, conversely, if the reflectivity function becomes at 2-D delta Dirac function, then the image  $I(\zeta, \nu)$  becomes the Point Spread Function (PSF). However, the impulse response function introduces blurring effects that degrade the appearance of the output image, for this reason, it has to be processed to retrieve the object reflectivity.

To clarify the relation between the Range-Doppler measurements and ISAR imaging system, let refer to the same signal model introduced in the section 1.3. In particular, the model of the received signal after demodulation and radial motion compensation can be expressed as follows:

$$S_R(t, f) = \iint \rho(\tau, f_D) \exp \{-j4\pi f/c [\zeta \cos \theta(t) - \nu \sin \theta(t)]\} d\zeta d\nu, \quad (1.30)$$

where  $\rho(\zeta, \nu)$  is replaced by  $\rho(\tau, f_D)$ , it will be described later.

On the left side of formula (1.30), a frequency variable,  $f$ , represents the dependence of the received signal on the transmitted frequency. Assuming that the aspect angle is  $\theta(t) = \Omega t$  and its total variation is sufficiently close to zero, that is,  $|\Omega t| \ll 1$ , then (1.30) can be approximated as follows:

$$S_R(t, f) \cong \iint \rho(\tau, f_D) \exp \{-j4\pi f/c [\zeta - \nu \Omega t]\} d\zeta d\nu, \quad (1.31)$$

where  $\cos \theta(t) \cong 1$ , and  $\sin \theta(t) \cong \Omega t$ . To represent the time delay,  $\tau$ , and the Doppler shift,  $f_D$ , coordinates, (1.31) can be rewritten as follows:

$$S_R(t, f) = \iint \rho(\tau, f_D) \exp \{-j2\pi [f\tau - t f_D]\} d\tau d f_D, \quad (1.32)$$

where

$$\tau = 2\zeta/c \quad (1.33)$$

represents the round trip delay expressed as function of the range coordinate  $\zeta$ , and

$$f_D = 2f\Omega\nu/c \quad (1.34)$$

represents the Doppler frequency shift expressed as function of the cross-range,  $y$ . It should be pointed out that  $\rho(\tau, f_D)$ , in (1.32) represent the reflectivity function projected onto the Range-Doppler image plane.

Then the Range-Doppler image can be obtained by simply taking the Inverse Fourier Transform (IFT) of (1.32) with respect to  $t$  and  $f$  as follows:

$$\rho(\tau, f_D) = IFT \{S_R(t, f)\}, \quad (1.35)$$

where  $\rho(\tau, f_D)$  is the target's reflectivity function mapped onto the Range-Doppler plane, which is represented by the radar image  $I(r_m, f_{Dn})$  in (1.28).

In ISAR systems, the 2-D image is represented in the range and cross-range domain. The cross-range is the direction perpendicular to the range direction and contains the relative motion between the radar and the target. When the PSF is analyzed, the range and cross-range dimensions are coupled and this fact must be taken into account [4, 5]. Starting from the formula (1.35), it should be remarked that such results is only ideal; in fact, the reflectivity function  $\rho(\tau, f_D)$  would be estimated perfectly if its Fourier transform is known for all values of the slow time  $t$  and the frequency  $f$ . Unfortunately, such a function is known only in a limited region of such bidimensional domain  $(t, f)$ . Assuming that the Fourier transform of the reflectivity function is known in a limited domain defined by a new function,  $W(f, t)$ , it should be modified (1.29) as

$$\hat{\rho}(\tau, f_D) = IFT[S_R(t, f) \cdot W(t, f)]. \quad (1.36)$$

It should be clarified that the scope of the function  $W(t, f)$  is to take into account the limitation of the backscattered signal  $S_R(t, f)$  which is both band and time limited. According to the former consideration, the function  $W(f, t)$  can be approximated to a double *rect* functions in the time-frequency domains, as follow:

$$W(f, t) = \text{rect}\left(\frac{t}{T_{obs}}\right) \text{rect}\left(\frac{f}{B_W}\right). \quad (1.37)$$

If it has been considered  $\hat{\rho}(\tau, f_D)$  in (1.36) as the delay-time and Doppler ISAR image, so by exploiting the Fourier transform property, the ISAR image expression can be write as follow:

$$I(\tau, f_D) = \iint \rho(u, v) \cdot w(\tau - u, f_D - v) dudv, \quad (1.38)$$

where  $w(\tau, f_D) = IFT[W(t, f)]$  represents the ISAR imaging system PSF expressed in the delay time-Doppler domain, and can be made explicit as

$$w(\tau, f_D) = \text{sinc}(\tau B_W) \text{sinc}(f_D T_{obs}). \quad (1.39)$$

To be able to rewrite (1.38) into the spatial coordinates  $(\varsigma, v)$ , I will assume that a relationship exists between the time-delay  $\tau$ , and the range coordinate,  $\varsigma$ , and between the Doppler frequency,  $f_D$ , and the cross-range coordinate,  $v$ , as

$$\varsigma = f(\tau), \quad v = g(f_D). \quad (1.40)$$

the formula (1.38) can be rewritten as:

$$I(\varsigma, v) = \iint \rho(u, v) \cdot w(\varsigma - u, v - v) dudv, \quad (1.41)$$

where  $w(\varsigma, v)$  can be defined as the PSF in the spatial coordinates:

$$w(\varsigma, v) = \text{sinc}\left(\frac{\varsigma}{2B_W}\right) \text{sinc}\left(\frac{v}{2T_{obs}\Omega}\right). \quad (1.42)$$

## 1.5 ISAR image Resolution

ISAR image resolution is the ability to resolve separated scatterers in the ISAR image, and they determine the quality of the resulting image. To derive the resolution, let refer to the Range-Doppler interpretation in the section 1.4 as it provide a simple means to do it. More specifically, I will separately consider the two dimensions, range and Doppler, to easily calculate the two resolutions. This will allow to conclude that 2-D resolution is the Cartesian product of the two single resolutions.

### 1.5.1 Range Resolution

Typically, in modern coherent radar systems a concept of range compression is used to achieve high range resolution without transmitting very short pulses [8–10]. The idea behind the concept is that if a signal with wide bandwidth is transmitted, it can be compressed at the receiver by using a suitable signal processing method called the *matched filter*. The result of the compression is that the resolution in the time delay,  $\tau$ , is inversely proportional to the bandwidth of the transmitted signal, that is  $\Delta\tau \simeq 1/B_W$ , where  $B_W$  is the bandwidth of the transmitted signal. Thus the range resolution is obtained by inverting (1.33) and renaming  $\varsigma$  with  $\Delta r$  in

$$\Delta r = \frac{c}{2B_W}. \quad (1.43)$$

### 1.5.2 Cross-Range and Doppler Resolution

Doppler resolution refers to ability to distinguish two sinusoidal components in the Doppler frequency domain. If two sinusoidal signals are observed during a limited time interval,  $T_{obs}$ , they can be resolved only when the difference of two oscillating frequencies is greater than  $1/T_{obs}$ . By applying the concept to the Doppler resolution,

$$\Delta f_D = \frac{1}{T_{obs}}. \quad (1.44)$$

As a consequence, the cross-range resolution can also be obtained by combining (1.34) and (1.44) and renaming  $v$  with  $\Delta r_{cr}$  as

$$\Delta f_D = 2f\Omega \frac{\Delta r_{cr}}{c} = \frac{1}{T_{obs}}. \quad (1.45)$$

By inverting (1.45), the cross-range resolution can be obtained as:

$$\Delta r_{cr} = \frac{c}{2fT_{obs}\Omega}. \quad (1.46)$$

Based on (1.46), if  $f = 10$  GHz and  $T_{obs} = 1$  sec, to achieve 0.3 m cross-range resolution the target angular rotation rate must be  $2.86^\circ/s$ . A longer integration time may provide higher cross-range resolution but causes phase-tracking errors and makes Doppler smearing. Because Doppler resolution,  $\Delta f_D$ , is inversely proportional to the image integration time,  $T_{obs}$ , the cross-range resolution is proportional to the Doppler resolution with a scaling factor:  $2fT_{obs}\Omega/c$  which called the scaling factor.

It should also pointed out that the cross-range resolution depends on the target's motion through the parameter  $\Omega$ ; therefore, it is not known a priori. This is a typical problem as ISAR resolution performances are not predictable and depend on the radar-target dynamics, which are not controlled by the radar system.



# References

- [1] Franceschetti, G. and Lanari, R., *Synthetic Aperture Radar Processing*. Boca Raton, FL; CRC Press, 1999.
- [2] J. C. Curlander and R. N. McDonough, *Synthetic aperture radar*. John Wiley & Sons, 1991.
- [3] W. G. Carrara, R. S. Goodman, R. M. Majewski *et al.*, *Spotlight synthetic aperture radar: signal processing algorithms*. Artech House Boston, 1995.
- [4] C.-C. Chen and H. C. Andrews, “Target-motion-induced radar imaging,” *Aerospace and Electronic Systems, IEEE Transactions on*, no. 1, pp. 2–14, 1980.
- [5] —, “Multifrequency imaging of radar turntable data,” *Aerospace and Electronic Systems, IEEE Transactions on*, no. 1, pp. 15–22, 1980.
- [6] D. A. Ausherman, A. Kozma, J. L. Walker, H. M. Jones, and E. C. Poggio, “Developments in radar imaging,” *Aerospace and Electronic Systems, IEEE Transactions on*, no. 4, pp. 363–400, 1984.
- [7] J. L. Walker, “Range-doppler imaging of rotating objects,” *Aerospace and Electronic Systems, IEEE Transactions on*, no. 1, pp. 23–52, 1980.
- [8] D. R. Wehner, “High resolution radar,” *Norwood, MA, Artech House, Inc., 1987, 484 p.*, vol. 1, 1987.
- [9] M. Skolnik, *Radar Handbook*. McGraw Hill Press, 2008.
- [10] M. A. Richards, J. Scheer, W. A. Holm *et al.*, *Principles of modern radar: basic principles*. SciTech Pub., 2010.



## Chapter 2

# Inverse Synthetic Aperture Radar Image Processing

*As it has been discussed in the Chapter 1, ISAR can generate high resolution range-Doppler images of moving target. High range resolution is obtained by compressing wideband signal waveform as FMCW or stepped-frequency waveform. High range resolution allow to resolve different scatterer centers into different range cells. On the other hand for increasing radar image resolution in cross-range a larger antenna aperture is required. Antenna aperture can be synthesized through the relative motion between a target to be imaged and the radar sensor. From the point of view of the synthesizing aperture, for a stationary radar and a rotating target ISAR image of the target is equivalent to a spotlight SAR image of a stationary target (see Figure 2.1). In this chapter, I will introduce the most commonly used ISAR image formation processing and briefly compare it with the SAR processing chain.*

### 2.1 ISAR processing background

Theoretical formulation of ISAR imaging is described by Walker's model [1–3], now, I will focus on analyzing factors that make an ISAR image defocused and on ISAR processing techniques that compensate the effect of target motion and rotation for refocusing radar moving target image. Let refer to the formula (1.25), the received signal can be modelled as:

$$S_R(t) = \exp \left[ -j4\pi f \frac{R(t)}{c} \right] \iint \rho(\varsigma, \nu) \exp \{ -j2[\varsigma k_\varsigma(t) - \nu k_\nu(t)] \} d\varsigma d\nu, \quad (2.1)$$

where the two wavenumber components are determined by

$$k_\varsigma(t) = \frac{2\pi f}{c} \cos \theta(t) = k \cos \theta(t) \quad (2.2)$$

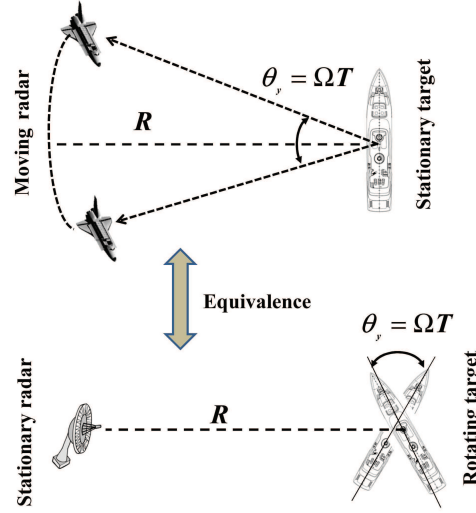


**Figure 2.1:** Equivalence between the SAR spotlight imaging system and an ISAR imaging rotating target.

and

$$k_v(t) = \frac{2\pi f}{c} \sin \theta(t) = k \sin \theta(t). \quad (2.3)$$

the instantaneous range and angle can be written in terms of the target motion characteristics:

$$\begin{cases} R(t) = R_0 + v_r t + \frac{1}{2} a_r t^2 + \dots, \\ \theta(t) = \theta_0 + \Omega t + \frac{1}{2} \gamma t^2 + \dots \end{cases} \quad (2.4)$$

where the translational motion are the initial range  $R_0$ , the velocity  $v_r$  and the acceleration  $a_r$ ; and, the angular rotation parameters are: the initial angle  $\theta_0$ , angular velocity  $\Omega$  and the angular acceleration  $\gamma$ . If these motion parameters can be accurately estimated, the phase term:  $\exp[-j4\pi f R(t)/c]$  can be completely removed. Thus, the target's reflectivity function  $\rho(\zeta, v)$  can be reconstructed exactly by taking the 2-D IFT. Thus for ISAR Range-Doppler image formation includes the following three main steps:

1. *Preprocessing*: The preprocessing step consists of processing received raw ISAR data to remove the amplitude and phase errors introduced during the data collection, to filter out unwanted modulations and interference effects and to crop the target of interest.
2. *Range processing*: Range processing consists of estimating the target's translational motion parameters and, then, compensating them. Subse-

quently, removing extra phase term, such that the target's range is no longer varying with the time. Typically, the range processing includes first a coarse range compensation and a subsequently fine range compensation.

3. *Cross-range processing*: Range processing is able to compensate only the translational motion respect to the rotation center of the target. If the target has rotation around the focal point, it may led to time-varying Doppler drifts  $f_D(t)$ , that introduce additional defocusing. Furthermore, if the effective rotation vector is time-varying, it can also induces cross-range defocusing. Therefore, the main goal of the cross-range processing is to estimate these two time-varying factors and, then, compensate the image defocusing before applying the 2-D IFT. Another issue relative to the cross-range processing is the cross-range scaling procedure, which consists of converting the image Doppler domain in the cross-range effective scale.

## 2.2 SAR and ISAR Range-Doppler processing

SAR is used to generate radar image of stationary targets, such as buildings and bridges. To achieve high cross-range resolution, SAR synthesizes a large-sized antenna aperture through a radar platform's motion in the along-track direction. The process of SAR imaging of a point target is depicted in Figure 2.2, SAR collects data from the target space, then, it converts data in the data space, and finally forms a SAR image in the image space. On the other

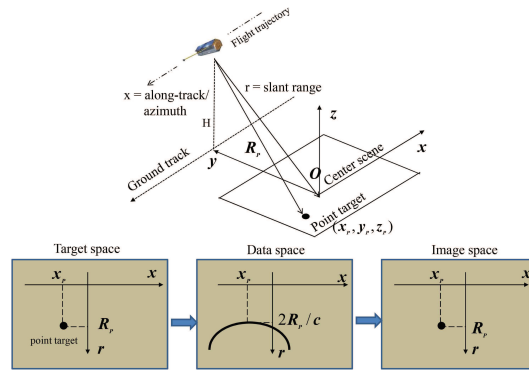


**Figure 2.2:** The process of SAR imaging of a stationary point target.

hand, ISAR synthesizes a larger antenna aperture through the relative rotation between radar and target. In a ground-based ISAR, a radar image of a moving target is generated through the relative rotation with respect to the radar. In an

airborne ISAR, a radar image of moving target is generated through the relative rotation contributed by both the target and the radar motions. Figure 2.3 illustrates the difference between SAR imaging of a stationary target and ISAR imaging of a moving target. The collected SAR raw data are similar to that of

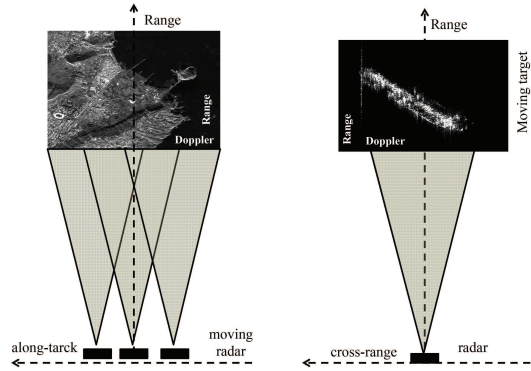


**Figure 2.3:** SAR imaging in range-azimuth domain and ISAR imaging in range-cross-range domain.

ISAR. Typically, the pulse number in ISAR data is replaced by the azimuth-cell domains (see Figure 2.4), similar to the ISAR raw data arrangement in Figure 1.6. The difference in terms of platform movement in ISAR is that the time-varying azimuth change due to the radar platform movement corresponds to the time-varying view angle change due to target movement. A block diagram

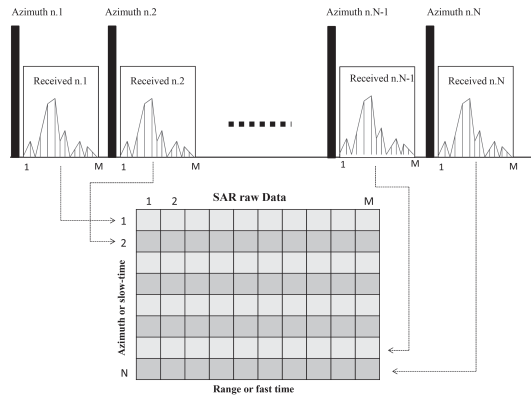


**Figure 2.4:** SAR raw data matrix formation.

of the SAR Range Doppler Algorithm (RDA) is shown in Figure 2.5. The SAR data are in the range-cell (fast-time) and azimuth-cell (slow-time) domains. A matched filter is used in the range domain for range compression. Because the

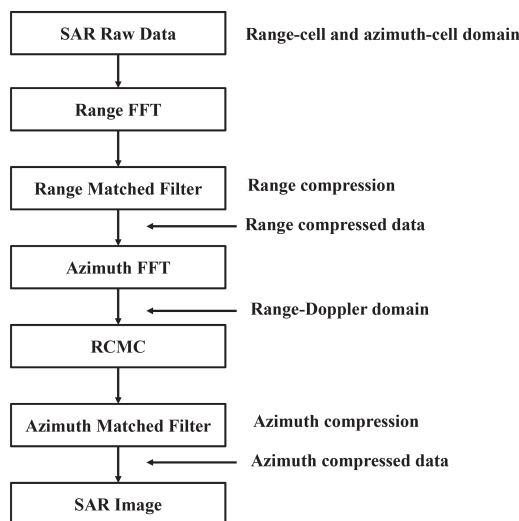


Figure 2.5: Block diagram of SAR range-Doppler algorithm.

RD algorithm works in the range and azimuth-frequency (Doppler) domains, the Fourier Transform in the azimuth domain must be taken to convert to the Doppler domain. Then, the Range Cell Migration Correction (RCMC) is performed in the range and Doppler domains to compensate for Range Cell Migration (RCM). After the RCMC, an azimuth-matched filter is applied. Finally, by taking the Inverse Fast Fourier Transform (IFFT) in the azimuth domain, the SAR image is formed. Similarly, a block diagram of the ISAR RDA is shown in Figure 2.6, where the raw ISAR data are arranged in the range-cells (fast-time) and number pulses (slow-time) domains. To reconstruct an ISAR range-Doppler image, firstly the range compression has been performed to obtain ISAR range profiles, after which the Translational Motion Compensation (TMC) is applied to remove target's translational motion. The common process of TMC includes two stages: range alignment and phase adjustment. If the target has more significant rotational motion during the CPI time, the former ISAR range-Doppler image can still be unfocused and smeared due to the rotational induced time-varying Doppler spectrum. In these cases, additional image-focusing algorithms for rotational motion errors must be applied. After removing translational and rotational motion, ISAR range-Doppler image is finally generated by taking the Fourier Transform (FT) in the pulses domain. To display ISAR image in the range and cross-range domain, cross-range scaling is also needed to convert Doppler shift to cross-range domain by applying the cross-range scaling procedure.

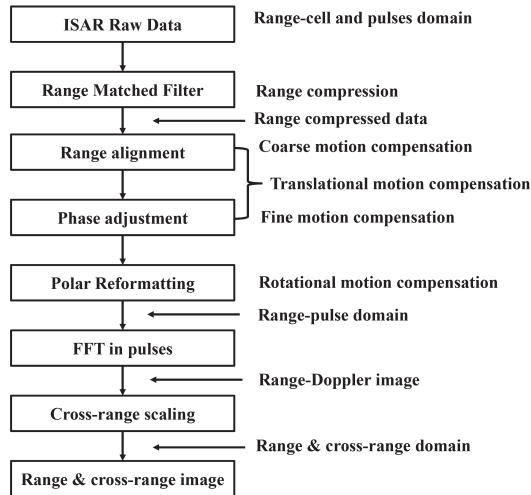
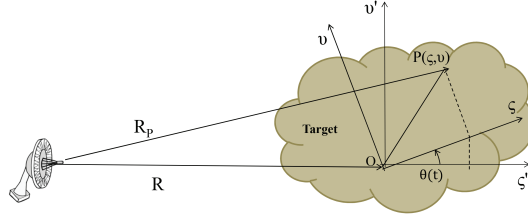


Figure 2.6: Block diagram of ISAR range-Doppler algorithm.

### 2.3 ISAR Motion Compensation

The motion of the target naturally affects the pulse-to-pulse coherence over the synthetic aperture. In order to use the synthetic aperture concept for generating fine azimuth resolution in radar imagery, both SAR and ISAR systems must account for the distance from the target to radar at the transmission time of each radar pulse. For the airborne SAR, an inertial measurement unit (IMU) and possibly a GPS receiver are onboard the SAR platform, and so knowledge of the position by various means is the solution without the need for explicit measurements. For the ISAR technique must be distinguished two cases: a case in which the moving target is cooperating with the radar and another where the target is not cooperating. If the target is cooperating, then, the sensor will know the movements of the target with a certain degree of precision and can realize a compensation procedure similar to the SAR technique. In the second case, the target is not cooperating, and so, the motion must be estimated in order to implement the motion compensation procedure. Motion effects in synthetic aperture radar involve three types of relative motion between radar sensor and the target [7]:

- Line Of Sight (LOS) translational motion which changes the distance between the target and the sensor without affecting the angular orientation between them;
- Rotational motion which changes the angular orientation between the target and the sensor without affecting the distance between them;



**Figure 2.7:** Geometry of a moving target with respect to radar.

- Motion of individual targets in SAR applications or non-rigid-body motion (vibration and bending) of ISAR target.

LOS translational motion introduces primarily space-invariant phase effects in the signal history. These effects are amenable to quadratic and higher order focus techniques in the image formation process. The rotational motion is important for two reasons. First, the appropriate component of rotational motion provides the basis for azimuth resolution in SAR and ISAR systems. Second, the image formation algorithm must also compensate the component of rotational motion which causes non-planar motion to the radar LOS vector. In the case of ISAR system, target rotational motion are particularly important because they greatly impact relative motion between the target and the radar. On the other hand, for the non-rigid-body motion of the target in ISAR applications causes space-variant image degradation, which the processor cannot ordinarily remove. The main difficulty is that the ISAR processing is a blind process. Hence, nobody knows any about the parameters of the motion of the target. That is why, motion compensation algorithms only suggest some good solutions, but they could not always be successful.

Let refer to the formula (2.4), the phase of the backscattered signal from the generic point  $P$  (see Figure 2.7) can be written as:

$$\phi(t) = -2\pi \frac{2f}{c} R_P(t). \quad (2.5)$$

Therefore, the Doppler frequency shift due to the motion can be calculated by taking the derivative of the previous phase as:

$$f_D = \frac{1}{2\pi} \frac{\partial}{\partial t} \phi(t) = -\frac{2f}{c} \frac{\partial}{\partial t} R_P(t) = \approx f_{D_{transl}} + f_{D_{rot}}, \quad (2.6)$$

where:

$$f_{D_{transl}} = \frac{2f}{c} (v_r + a_r t), \quad (2.7)$$

and

$$f_{D_{rot}} = -\frac{2f}{c} \Omega [\xi \sin \theta(t) + v \cos \theta(t)] - \frac{2f}{c} \gamma [\xi \sin \theta(t) + v \cos \theta(t)] t. \quad (2.8)$$

Assuming that the CPI is very short, about  $[1 - 2]$  seconds, the terms  $a_r t$  can be neglected, so, the translational Doppler frequency shift shown by Equation (2.7) can be considered constant for all of the scatterers on the target and produce a uniform (not differential) Doppler shift. Hence, this motion does not contribute to the cross-range resolution and of course to the ISAR imaging [4], but, unfortunately, this kind of translational motion causes the range walk. Range walk is referred as range misalignment in many of the sources. Hence, assuming the target's translational motion parameters and removing the related phase component from the received signals phase is called the translational motion compensation.

The rotational Doppler frequency shift, which is shown by the Equation (2.8), is a function of time. Therefore, it would need to be compensated depending to the strength of the angular rotation rate,  $\Omega$ , even if the translational motion compensation is already done. This process is called rotational motion compensation.

### 2.3.1 ISAR Translational Motion Compensation

In order to obtain clear and sharp images, the following conditions must be satisfied during the coherent image processing time:

1. The scatterers on the target must remain in their range cells.
2. Scatterer's Doppler frequency shifts must be constant.

If the scatterers drift out their range or their Doppler frequency cells; shifts are time varying, the Doppler spectrum obtained from the Fourier transform becomes smeared, and the radar image becomes blurred. The first step for the TMC is the Range Tracking. Range Tracking step includes re-alignment of the range profiles, in order to compensate the effect of range-walk. If a compensation algorithm only includes the Range Tracking step, it is called coarse motion compensation. The coarse range alignment allows a point-scatterer to be sorted into the same range-cell across all the pulses. However, in many cases, range tracking does not give satisfactory results because of the time-varying characteristic of the Doppler shifts in one range-cell, thus, fine motion compensation, called Doppler Tracking, should be applied to make phase compensation and, hence, Doppler frequency shifts, constant. Doppler Tracking step includes correction and compensation of the phases along the range-cells [5]. A possible solution for the implementation of both coarse and fine motion compensation is to adopt the De-ramping technique [6]. This kind of calibration procedure used to correct the translational motion component provides essentially the product of the received signal for the following phase factor, also known as de-ramping factor [7]:

$$e^{j2\pi \frac{2f}{c} R(t)} \quad (2.9)$$

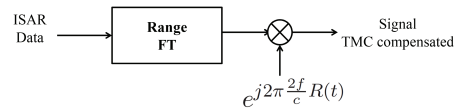


**Figure 2.8:** De-ramping procedure

where  $R(t)$  is the distance between the sensor and a reference point at the center of the target (focal point). The compensation of the range migration has been implemented converting the raw signal in the Fourier domain and multiplying it by the phase factor, according to the Figure 2.8. The De-ramping procedure allows obtaining the complete focusing of the single reference point, instead, the motion compensation procedure is not able to realize the full image focusing, in fact, if the observation interval is too long, the points which are shifted respect to the reference point, will be blurred. In the Figure 2.9(a) it has been shown



(a) Amplitude and phase of a point close to the reference point. (b) Amplitude and phase of a point displaced with respect to the reference point.

**Figure 2.9:** De-ramping effects.

an example relative to the amplitude and phase of the focal point after the de-ramping correction, as can be see the range migration has been completely compensated. On the contrary, in Figure 2.9(b) is shown the amplitude and phase response of the target shifted in range after the motion compensation by the De-ramping technique; the residual migration can be clearly appreciated, not so much on the amplitude of signal, but in the phase of the signal where it is evident the quadratic distortion. This phenomenon is what is defined as Residual Motion Through Resolution Cell; due to such residual migration the image associated with this target will be defocused.

### 2.3.2 ISAR Rotational Motion Compensation

As described in the first Chapter, in ISAR images the Doppler shift are induced by the target's rotation, if a target rotates too fast or the CPI is too long, after the translational motion compensation the Doppler frequency shifts can be time varying. In this cases, the final reconstructed ISAR range-Doppler image can still be smeared. Therefore, the rotational motion correction is needed to compensate the angular time-varying frequency components defined in formula (2.8).

After the translational motion compensation, the target has only rotation

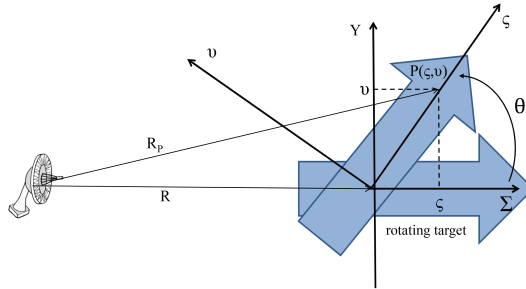


Figure 2.10: Radar and a rotating target.

about the center at a constant range, as depicted in Figure 2.10. The backscattered signal can be expressed as follow:

$$S'_R(t) = \iint \rho(\varsigma, v) \exp \{-j2\pi[\varsigma f_\varsigma(t) - v f_v(t)]\} d\varsigma dv, \quad (2.10)$$

where the spatial frequency are:

$$f_\varsigma(t) = \frac{2\pi f}{c} \cos \theta(t), \quad (2.11)$$

and

$$f_v(t) = \frac{2\pi f}{c} \sin \theta(t) = k \sin \theta(t). \quad (2.12)$$

The two Cartesian coordinates  $f_\varsigma$  and  $f_v$  and the two polar coordinates  $f$  and  $\theta$  are related by the transform

$$\begin{cases} f = \sqrt{f_\varsigma^2 + f_v^2} \\ \theta = \tan^{-1} \left( \frac{f_v}{f_\varsigma} \right) \end{cases} \quad (2.13)$$

Then, the target reflectivity function,  $\rho(\varsigma, v)$ , can be reconstructed by taking the IFT:

$$\rho(\varsigma, v) = \iint S'_R(f_\varsigma, f_v) \exp \{j2\pi[\varsigma f_\varsigma(t) - v f_v(t)]\} df_\varsigma df_v. \quad (2.14)$$

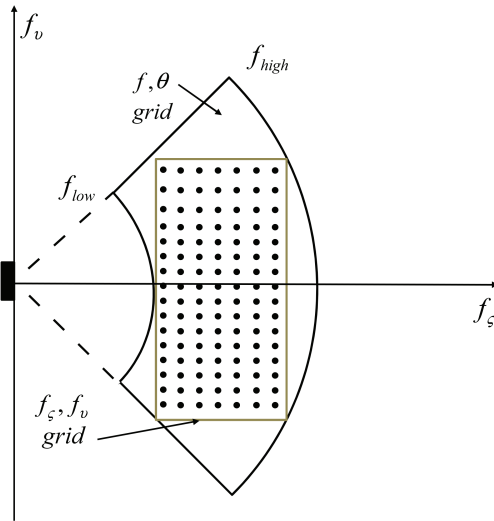


**Figure 2.11:** Polar reformatting mapping from polar to rectangular domain.

Therefore, one possible way to mitigate the de-focusing introduced by the rotational motion and to estimate to the reflectivity of the target is to map the backscattered signal  $S'_R$  from a domain defined by the polar coordinates  $(f, \theta)$  to a rectangular domain defined by Cartesian coordinates  $(f_\zeta, f_v)$ , as illustrated in Figure 2.11, this process is known as *polar reformatting*.

### 2.3.3 ISAR Polar Formatting

The motion compensation allows only achieving the reference point full focusing, while the other points, affected by time varying rotational motions, will be blurred. In fact, the variation of the distance due to the relative motion between radar and target, during the process of the electromagnetic echoes collection, determines a migration of the bright points. This phenomenon known as Residual Motion Through Resolution Cells (RMTRC), must be adequately compensated in order to realize the image focusing. One of the well-known techniques to alleviate losses image focusing caused by the space variant characteristics of the RMTRC is the Polar Formatting [8]. In general, the motion compensation procedure, similarly to the de-chirp technique, transforms the raw data from the azimuth-time domain to the azimuth-frequency domain. In general the phase history data collected for the target represents a polar raster in the Fourier domain, so polar format processing is about reformatting the data to a Cartesian grid array for efficient digital processing and image formation of both SAR and ISAR data.

The PFA is based on the radar tomography developed in medical imaging,

which has been used to reconstruct a spatial domain object. According to the projection slice theorem [9], a projection of the function (to be estimated) in one domain represents a slice in the Fourier domain, so that: varying the direction of the projection it is possible to obtain coverage of the spectral region of the object function. In principles, the ISAR PFA is similar to the spotlight SAR PFA [10]. However, in ISAR the target's aspect angle is changed by the target's motion and is typically unknown and uncontrollable. Because the aspect angle change defines the data surface, the target's rotation must be estimated before applying the PFA in ISAR. To implement the PFA in ISAR the motion parameters should be measured from the received radar data for modeling the data surface, projecting the data surface onto a planar surface, interpolating the data into equally spaced samples, and performing the Fourier transform. A possible solution to apply the ISAR PFA is by splitting the 2-D interpolation into two one-dimensional interpolations along range and cross-range directions. The decomposition from two-dimensional to one-dimensional interpolation problem allows also reducing the computational load and making the processing more efficient. In details the procedure provides primarily an interpolation along the range coordinate going from a polar domain to an intermediate trapezoidal domain. Then, the polar formatting algorithm is finished performing the interpolation along the azimuth coordinate from the trapezoidal to the rectangular domain (see Figure 2.12). The main effects associated with the use

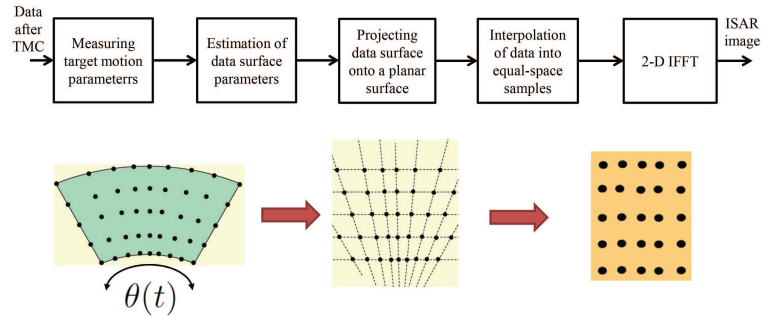
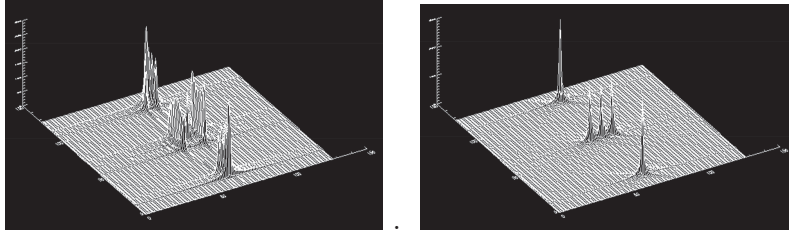


**Figure 2.12:** ISAR PFA block diagram

of the PFA are: the compensation of the residual quadratic phase migration, and, in this way, obtaining the image focusing. Moreover the PFA, thanks to the final rectangular grid samples disposition, enables the Fast Fourier Transform (FFT) codes, which are used for the final image formation process, to work in optimal conditions. On the other hand, however, the two consecutive interpolation steps may cause loss of the accuracy and efficiency; this cannot be neglected especially when the processor works with a large of a real data-set. In Figure 2.13 is shown an example of the effect of the PFA, as can be seen, the use of PFA allows performing the full focusing of this five scatterers, instead,

without the use of the PFA, the five simulated scatterers shifted (respect the reference compensation) are blurred and only the central point is full focused.



(a) Amplitude of 5 simulated scatterers before the application of PFA. (b) Amplitude of 5 simulated scatterers after the application of PFA.

**Figure 2.13:** PFA effect for rotational motion compensation.

## 2.4 ISAR Image Autofocusing Techniques

Autofocus allows generating images with a better quality by automatically adjusting the image focusing parameters. For radar imaging, autofocus means to automatically correct phase errors based on collected radar returns from targets. As discussed in the section 2.3, ISAR translational motion compensation includes range alignment and phase adjustment. The phase adjustment process is for removing the residual translational errors on the phase terms. The phase errors are the cause of image defocusing. Phase adjustment algorithms based on radar data itself are called image autofocus algorithms [8, 11]. ISAR autofocus methods can be distinguished in two main groups:

- *Parametric*: make use of a signal model;
- *Non Parametric*: do not use any specific signal model.

The most popular non parametric autofocus techniques are: the Prominent Point Processing (PPP) and the Phase Gradient Autofocus (PGA). The PPP algorithm utilizes information from prominent points to correct the phase errors and to convert non uniform rotation in uniform rotation; in particular, it tracks multiple selected prominent scatterers in a target to extract motion parameters [8] and remove both space-invariant and space-variant errors. In multiple PPP, the first prominent point is selected for removing translational motion and adjusting the phase of the received signal so as to form a new image center; then, a second prominent point is selected for correcting phase errors induced by non uniform rotations, and finally, if it is necessary, a third point is selected for the correction of rotation rate and complete the final focusing [8].

The other non parametric technique is the PGA, which was been proposed

in [12], and, it has also been used in SAR autofocus. The PGA attempts to focus the radar image by minimizing the residual translational errors which are present in the defocused image; it makes a robust estimation of the gradient of the phase error by measuring the pulse-to-pulse phase difference at each range cell and averaging for each range cells, then, the procedure is iterated until the root mean square phase error becomes small enough.

On the other hand, the most important parametric autofocusing techniques are: the Image Contrast Based Autofocus (ICBA) and the Entropy Minimization Based Autofocus (EMBA). Both the techniques use a mathematical model based on the target motion parameters which the techniques try to estimate for correcting the smearing effects and hence correctly focusing the ISAR image. The ICBA aims to realize well focused ISAR image by maximizing the contrast of the image, vice versa, the EMBA try to minimize the entropy of the image to perform the image autofocusing. As matter of fact both the contrast and the entropy, are two indicators of the radar image quality. Thus, both the techniques adopt two mathematical cost functions, based on this two image quality indicators, for estimating the target focusing parameters by performing exhaustive search algorithm which maximize or minimize the respectively cost functions.

### 2.4.1 Image Contrast Based Autofocus

The Image Contrast Based Autofocus Technique is one of the most important parametric technique for the ISAR autofocusing algorithm present in literature [13]. ICBA aims to form well focused ISAR images by maximizing the image contrast cost function. The innovative features of this algorithm can be described by the following two main characteristics:

1. Parametric nature of the ICBA: the radial motion of the target's point is described by a parametric function (typical a Taylor polynomial)
2. Radial motion compensation is implemented in one step, avoiding the range alignment step.

When the relative radar-target motion is regular, the distance from the radar to the reference focusing point focusing on the target to the radar  $R(t)$  can be approximated around the central time instant  $t = 0$  by means of a Taylor's polynomial as follows:

$$R(t) \cong \tilde{R}(t) = \sum_{n=0}^N \frac{\alpha_n t^n}{n!}, \quad (2.15)$$

where  $\alpha_n = d^n R(t)/dt^n$ . Since the term  $R(t)$  must be estimated and compensated for. The ISAR image autofocus problem reduces to the estimation of the  $\alpha_n$  coefficients. Typically, a second or a third order polynomial is sufficient to

describe target's radial motions for a short integration time intervals, which are usually good enough to form high-resolution ISAR images at C-band or higher frequencies. It should be pointed out that: the zero-order term,  $\alpha_0$ , is constant with respect to the slow-time variable  $t$ , being equal to  $\exp(-j4\pi f\alpha_0/c)$ . It is easy to demonstrate that such phase term does not produce any image defocus effect as it is a constant phase term. This fact, allows neglecting this zero-order component, and so, reducing the autofocus problem to the estimation of only remaining coefficients: the second and the third order coefficients. The ICBA technique is typically implemented in two steps: (1) preliminary estimation of the defocusing parameters, which is accomplished with an initialization technique that use the Radon Transform (RT); and (2) a fine estimation which obtained via an exhaustive search by solving an optimization problem where the cost function to be maximized is the image contrast.

*Estimation of  $\alpha_1$ .* Let  $S_R(\tau, kT_{PRI})$  be the range-compressed radar data collecting during the  $k$ -th radar pulse, with  $\tau$  representing the round trip delay and time  $T_{PRI}$  the pulse repetition interval. An example of the real data range profile time history,  $S_R(\tau, kT_{PRI})$ , is plotted in Figure 2.14. It may be easily noted that the stripes, due to the main scatterer range migration, are almost linear; each stripe represents the trace of the time history of a generic scatterer. To estimate the value of  $\alpha_1$  it has been assumed that:

1. the distance  $R_{S_i}(kT_{PRI})$  relative to the  $i$ -th scatterer varies linearly with a slope equal to  $\alpha_1$ , that is,  $R_{S_i}(kT_{PRI}) \approx R_{S_i}(0) + \alpha_1 kT_{PRI}$
2. the focusing point distance has roughly the same linear behaviour of each scatterer. In general the focusing point does not need to be coincident with any real scatterer.

So, if the previous assumption are satisfied, the preliminary estimation of  $\alpha_1$  can be obtained by calculating the mean slope of the scatterer distance traces. In fact, let  $\alpha_1 = \tan(\phi)$ , where the angle  $\phi$  regarding the angle between the abscissa axis and the scatterer trace, and can be calculated by the RT as follow:

$$\hat{\phi} = \arg \{ \max_{\phi} RT[S_R(r, \phi)] \} - \frac{\pi}{2}, \quad (2.16)$$

where  $RT[S_R(r, \phi)]$  is the Radon Transform of  $S_R(\tau, kT_{PRI})$ , hence the estimation of  $\hat{\alpha}_1$  is obtained by equating  $\hat{\alpha}_1 = \tan(\hat{\phi})$ .

*Estimation of  $\alpha_2$ .* Let  $I(\tau, \nu, \tilde{\alpha}_1, \tilde{\alpha}_2)$  be the absolute value of the complex image obtained by compensating the received signal with two initial values of  $(\tilde{\alpha}_1, \tilde{\alpha}_2)$ . The Image Contrast (IC) is defined as [13, 14]:

$$IC(\tilde{\alpha}_1, \tilde{\alpha}_2) = \frac{\sqrt{A \{ [I(\tau, \nu, \tilde{\alpha}_1, \tilde{\alpha}_2) - A \{ I(\tau, \nu, \tilde{\alpha}_1, \tilde{\alpha}_2) \}]^2 \}}}{A \{ I(\tau, \nu, \tilde{\alpha}_1, \tilde{\alpha}_2) \}}. \quad (2.17)$$

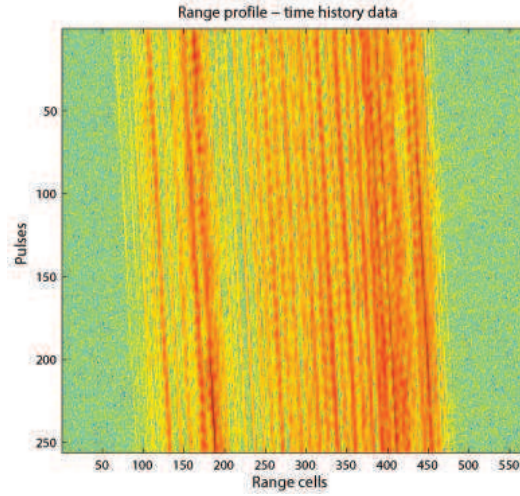


Figure 2.14: Range Profiles of the received signal after range-compression.

where  $A\{\cdot\}$  represents the image spatial mean over the coordinates  $(\tau, \nu)$ . The function  $IC(\tilde{\alpha}_1, \tilde{\alpha}_2)$  represents the normalized effective power of the image intensity  $I(\tau, \nu, \tilde{\alpha}_1, \tilde{\alpha}_2)$  and gives a measure of the image focusing. In fact, when the image is correctly focused, it is composed of several pronounced peaks that enhance the contrast. When the image is defocused, the image intensity levels are concentrated around the mean value and the contrast is low. The final estimation of focusing parameters  $\alpha_1$  and  $\alpha_2$  is obtained through an exhaustive search by maximizing the IC resolving the following optimization problem:

$$(\tilde{\alpha}_1, \tilde{\alpha}_2) = \arg(\max_{\tilde{\alpha}_1, \tilde{\alpha}_2} [IC(\tilde{\alpha}_1, \tilde{\alpha}_2)]). \quad (2.18)$$

# References

- [1] D. A. Ausherman, A. Kozma, J. L. Walker, H. M. Jones, and E. C. Poggio, "Developments in radar imaging," *Aerospace and Electronic Systems, IEEE Transactions on*, no. 4, pp. 363–400, 1984.
- [2] J. L. Walker, "Range-doppler imaging of rotating objects," *Aerospace and Electronic Systems, IEEE Transactions on*, no. 1, pp. 23–52, 1980.
- [3] W. M. Brown, "Walker model for radar sensing of rigid target fields," *Aerospace and Electronic Systems, IEEE Transactions on*, no. 1, pp. 104–107, 1980.
- [4] M. Prickett and C. Chen, "Principles of inverse synthetic aperture radar/isar/imaging," in *EASCON'80; Electronics and Aerospace Systems Conference*, vol. 1, 1980, pp. 340–345.
- [5] V. C. Chen, *Time-frequency Transforms for Radar Imaging and Signal Analysis*. Artech House, 2006.
- [6] C. Noviello and G. Fornaro, "Inverse and direct synthetic aperture radar data processing," in *Gold Conference, 2012. Proceedings of*. IEEE, 2012, pp. 134–136.
- [7] Franceschetti, G. and Lanari, R., *Synthetic Aperture Radar Processing*. Boca Raton, FL; CRC Press, 1999.
- [8] W. G. Carrara, R. S. Goodman, R. M. Majewski *et al.*, *Spotlight synthetic aperture radar: signal processing algorithms*. Artech House Boston, 1995.
- [9] A. C. Kak and M. Slaney, *Principles of Computerized Tomographic Imaging*. SIAM, 2001, vol. 33.
- [10] D. R. Wehner, "High resolution radar," *Norwood, MA, Artech House, Inc., 1987, 484 p.*, vol. 1, 1987.
- [11] C. V. Jakowatz, D. E. Wahl, P. H. Eichel, D. C. Ghiglia, and P. A. Thompson, *Spotlight-mode synthetic aperture radar: a signal processing approach*. Kluwer Academic Publishers Boston, 1996, vol. 101.

- [12] D. Wahl, P. Eichel, D. Ghiglia, and C. Jakowatz Jr, "Phase gradient autofocus—a robust tool for high resolution sar phase correction," *Aerospace and Electronic Systems, IEEE Transactions on*, vol. 30, no. 3, pp. 827–835, 1994.
- [13] M. Martorella, F. Berizzi, and B. Haywood, "Contrast maximization based technique for 2-d isar autofocusing," *IEE Proc. Radar Sonar Navig.*, vol. 152, no. 4, pp. 253–262, 2005.
- [14] F. Berizzi and G. Corsini, "Autofocusing of inverse synthetic aperture radar images using contrast optimization," *Aerospace and Electronic Systems, IEEE Transactions on*, vol. 32, no. 3, pp. 1185–1197, 1996.

## Chapter 3

# Inverse Synthetic Aperture Radar Doppler Parameters Autofocus Technique

*As it has been discussed in the Chapter 2, autofocus allows generating high-resolution ISAR images by automatically correcting the defocusing caused by the radar-target relative motion. If the phase adjustment algorithm is based on estimation carried out by collected radar data, the algorithm is called autofocus. ISAR autofocus methods are usually distinguished in parametric and non parametric. Here, I discuss about a novel ISAR parametric autofocus technique by exploiting the estimation of the target Doppler parameters: namely the Doppler centroid and the Doppler rate, which are related to the target motion parameters. The proposed Doppler parameter autofocus algorithm is based on the re-use of efficient autofocus approaches that are classically used in direct SAR imaging. The effectiveness of the proposed method has been tested on COSMO-SkyMed Spotlight SAR data of maritime moving targets. Further experiments have been carried out also on data acquired by a static ISAR system. Furthermore, the proposed Doppler Parameter Estimation Algorithm (DPEA) has been compared with the well known autofocus ISAR technique, namely the Image Contrast Based Technique (ICBT), which has been introduced in previous Chapter and it has been used as benchmark for validating the proposed technique which, by avoiding the use of exhaustive search, shows better computational performances.*

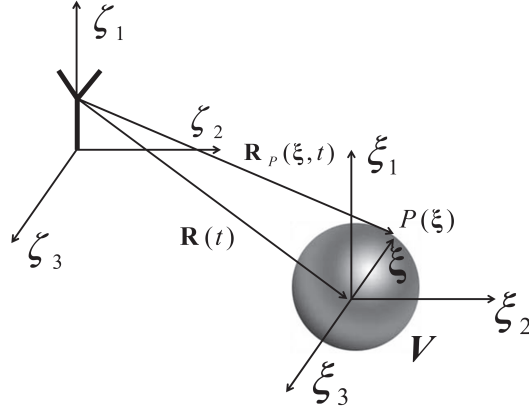


**Figure 3.1:** Reference geometry of the ISAR system with the sensor centred reference system and the reference system moving solidly with the target.

### 3.1 ISAR Doppler Parameters Model

The proposed Doppler Parameters Autofocus Technique aims to focus the ISAR images by estimating the Doppler radar signal parameters, which are directly related to the target motion parameters. In order to derive the relationship between the Doppler parameters and the target motion parameters, let consider the geometry depicted in Figure 3.1 where the sensor is located at  $(0, 0, h)$  in the system of coordinates  $(\zeta_1, \zeta_2, \zeta_3)$ , and let consider the reference system  $(\xi_1, \xi_2, \xi_3)$  on the target, which is assumed to move along an arbitrary trajectory. The signal backscattered from the target to the sensor, in the representation of frequency  $f$  and slow-time  $t$  (sampled at  $kT_{PRI}$ ) is given by:

$$S_R(f, t) = W(f, t)e^{-j4\pi \frac{t}{c}R(t)} \int_V \rho(\boldsymbol{\xi})e^{-j4\pi \frac{t}{c}\boldsymbol{\xi}^T \cdot \mathbf{i}_{LOS}(t)} d\boldsymbol{\xi}, \quad (3.1)$$

such that:

$$W(f, t) = \text{rect}\left(\frac{t}{T_{obs}}\right) \text{rect}\left(\frac{f - f_0}{B_W}\right), \quad (3.2)$$

where  $\rho(\boldsymbol{\xi})$  is the reflectivity function, which represents the backscattering properties of the target,  $V$  is the domain where the reflectivity function is defined,  $c$  is the speed of light,  $\boldsymbol{\xi}$  is the vector that locates a generic scatterer on the target reference system,  $f_0$  is the carrier frequency,  $T_{obs}$  is the observation interval, and  $B_W$  is the transmitted signal bandwidth. The formula (3.1) refers to a typical ISAR scenarios, where the target size can be assumed to be significantly smaller than the radar-target distance, and, therefore, the iso-range approximation can be applied:  $R_P(\boldsymbol{\xi}, kT_R) \simeq R(t) + \boldsymbol{\xi}^T \cdot \mathbf{i}_{LOS}(t)$  [1]. Where  $\mathbf{i}_{LOS}(t)$  is the line of sight unit vector at time  $t$ , and  $R(t)$  is the modulus of the

vector  $\mathbf{R}(t)$  which locates the position of the focusing point on the target. The composition of both translation and angular motions can be interpreted as an equivalent rotation vector  $\mathbf{\Omega}_{tot}$ . The projection of  $\mathbf{\Omega}_{tot}$ , on the plane which is orthogonal to the line of sight is defined as the effective rotation vector  $\mathbf{\Omega}_{eff}$  by means [2]:

$$\mathbf{\Omega}_{eff} \triangleq \mathbf{i}_{LOS} \times (\mathbf{\Omega}_{tot} \times \mathbf{i}_{LOS}). \quad (3.3)$$

This component is in fact the only one projection that provides a contribution to the formation of the Doppler band. Therefore, the plane orthogonal to the  $\mathbf{\Omega}_{eff}$  can be defined as the image plane. To simplify the notation, the orientation of the target reference system can be chosen by letting  $\xi_3$  orthogonal to the image plane. Accordingly the image plane is defined by  $(\xi_1, \xi_2)$ , and so, the following scalar product can be written as:  $\mathbf{\xi}^T \cdot \mathbf{i}_{LOS}(t) = \xi_1 \sin \theta(t) + \xi_2 \cos \theta(t)$ . Where  $\theta(t)$  is the radar-target aspect angle. According to this assumption the received signal can be written as:

$$S_R(f, t) = W(f, t) e^{-j(4\pi f/c)R(t)} \iint \rho(\xi_1, \xi_2) e^{-j4\pi \frac{f}{c}(\xi_1 \sin \theta(t) + \xi_2 \cos \theta(t))} d\xi_1 d\xi_2, \quad (3.4)$$

where  $\int \rho(\xi_1, \xi_2, \xi_3) d\xi_3 = \rho(\xi_1, \xi_2)$  is the projection of the reflectivity function on the image plane. Then, by defining the following transformation:

$$\Psi : \begin{cases} \Xi_1 = \frac{2f}{c} \sin \theta(t) \\ \Xi_2 = \frac{2f}{c} \cos \theta(t) \end{cases} \quad (3.5)$$

the signal in (3.4) can be expressed as:

$$S_R(f, t) = W(f, t) e^{-j4\pi \frac{f}{c}R(t)} \iint \xi(\xi_1, \xi_2) e^{-j2\pi(\Xi_1 \xi_1 + \Xi_2 \xi_2)} d\xi_1 d\xi_2 \quad (3.6)$$

In order to reconstruct the image of the target, motion compensation should be carried out by removing phase term  $\exp\{-j(4\pi f/c)R(t)\}$ , which is due to the radial motion parameter of the focusing point. In the ISAR context, The Range-Doppler technique is the conventional method used for reconstructing ISAR images. This approach can be applied when the target's rotation can be considered very smooth, and so the effective rotation vector  $\mathbf{\Omega}_{eff}$  is constant within the observation time  $T_{obs}$ . Therefore, when the aspect angle changes of few degree it can be approximated as:  $\theta(t) = \Omega_{eff} t$ . So the received signal in (3.4) can be rewritten as follows:

$$S'_R(f, t) \approx W(f, t) \iint \rho(\xi_1, \xi_2) e^{-j2\pi \frac{2f_0}{c} \frac{\Omega_{eff}}{T_{obs}} \xi_1 t} e^{-j2\pi \frac{2f}{c} \xi_2} d\xi_1 d\xi_2. \quad (3.7)$$

As described in the second Chapter, the motion compensation is the most crucial step in the ISAR image formation process. Assuming that the dwell time is about 1 – 2 seconds, then the distance term  $R(t)$  can be approximated (around the central time at  $t = 0$ ) by second order Taylor polynomial:

$$R(t) \approx R_0 + v_r t + a_r t^2 \quad (3.8)$$

where  $v_r = \dot{R}(0)$  and  $a_r = \ddot{R}(0)/2$ . The estimation of first term  $R_0$  can be avoided, as it only causes a constant shift along the range coordinate without defocusing the image [1]. The terms  $v_r$  and  $a_r$  physically represent the target's radial velocity and acceleration. In this context, both the terms are considered as constant over the slow-time domain. The coefficients  $v_r$  and  $a_r$  are also related to the Frequency Doppler Parameters. Indeed, by differentiating the expression of the phase of the motion compensation term with respect to the slow-time  $t$ , the instantaneous Doppler frequency can be obtained as:

$$f_D(t) = f_{DC} + f_{DR}t \quad (3.9)$$

where  $f_{DC}$  is the Doppler Centroid and  $f_{DR}$  the Doppler Rate, whose binding to the coefficients  $v_r$  and  $a_r$  are:

$$\begin{cases} f_{DC} = \frac{2f_0}{c}v_r \\ f_{DR} = \frac{4f_0}{c}a_r \end{cases} \quad (3.10)$$

therefore, the both motion coefficients  $v_r$  and  $a_r$ , can be calculated by estimating the Doppler parameters (i.e.  $f_{DC}$  and  $f_{DR}$ ).

## 3.2 Doppler Centroid Estimation

In the previous section, I showed the important relationship between the motion parameters and the signal Doppler parameters. In this section, I will discuss how to estimate the Doppler centroid by using an algorithm implemented by Madsen [3] which is typically used in standard SAR image focusing. In particular I will describe how this algorithm is modified to adapt to an ISAR configuration. The Doppler centroid plays an important role in the cross-range processing. In fact, this parameter is directly related to the target's radial velocity and also represents the average Doppler shift, which affects the backscattered signal. With reference to (3.6), let define the following function:

$$S(f, t) \triangleq W(f, t)e^{-j2\pi\frac{2f}{c}a_r t^2} \iint \xi(\xi_1, \xi_2)e^{-j2\pi(\Xi_1\xi_1 + \Xi_2\xi_2)}d\xi_1d\xi_2 \quad (3.11)$$

To simplify the notation I will consider only the dependence on  $t$  and will temporarily neglect the dependence on  $f$ . Therefore, the received signal can be written as:

$$S'_R(t) = S(t)e^{-j2\pi\frac{2f_0}{c}v_r t} \quad (3.12)$$

where  $\frac{2f_0}{c}v_r$  is the Doppler centroid  $f_{DC}$ . Let now consider the function  $P(f_d)$  defined as the power Doppler spectrum associated with the signal  $S(t)$ . Therefore the power Doppler spectrum of  $S'_R(t)$ , can be written as:

$$P_s(f_d) = P(f_d - f_{DC}) \quad (3.13)$$

The autocorrelation function  $R_s(\eta)$  can then be calculated as the IFT of  $P_s(f_d)$ , as follow:

$$R_s(\eta) = FT^{-1}[P_s(f_d)] = R(\eta)e^{j2\pi\eta f_{DC}} \quad (3.14)$$

with

$$R(\eta) = FT^{-1}[P(f_d)] \quad (3.15)$$

As the signal  $S(t)$  is sampled in the time domain,  $\eta = kT_{PRI}$   $k = 0, 1, \dots, N-1$  must be substituted in (3.14), as follows:

$$R_s(k) = R(k)e^{j2\pi k T_{PRI} f_{DC}} \quad (3.16)$$

So, in the time domain, measuring the phase of the correlation coefficient it is possible to estimate the Doppler centroid, as:

$$\hat{f}_{DC} = \frac{1}{2\pi k T_{PRI}} \arg\{R_s(k)\} \quad (3.17)$$

Because the sampling step  $T_{PRI}$  may be not small enough, the Doppler estimation may be affected by an aliasing error. For this reason, the centroid can be considered as composed of two parts: an integer number, namely the Doppler Ambiguity, and the fractional part, which can be interpreted as the wrapped Doppler centroid. In formula, this can be expressed as follow:

$$f'_{DC} = \hat{f}_{DC} + M \cdot PRF \quad (3.18)$$

Where  $f'_{DC}$  is the unwrapped Doppler centroid,  $\hat{f}_{DC}$  is the estimated wrapped Doppler centroid. The estimator presented in (3.17) is able to provide the wrapped Doppler centroid. In order to correctly estimate the Doppler centroid, also the ambiguity number  $M$  must be estimated. In this work, such a number is estimated by using the Multi-Look Beat Frequency (MLBF) algorithm, which was developed by Cumming for the SAR system [4].

With reference to the formula (3.6) let define the two range compressed looks of a single point target that are shifted by a frequency  $\Delta f$ :

$$\mathfrak{L}_1(f, t) = \text{rect}\left(\frac{t}{T_{obs}}\right) \text{rect}\left(\frac{f - f_0 - \frac{\Delta f}{2}}{B_W}\right) e^{-j4\pi\left(\frac{f_0 - \frac{\Delta f}{2}}{c}\right)R(t)} \quad (3.19)$$

$$\mathfrak{L}_2(f, t) = \text{rect}\left(\frac{t}{T_{obs}}\right) \text{rect}\left(\frac{f - f_0 + \frac{\Delta f}{2}}{B_W}\right) e^{-j4\pi\left(\frac{f_0 + \frac{\Delta f}{2}}{c}\right)R(t)} \quad (3.20)$$

The MLBF algorithm calculates the beating product between two range looks with the result as follows and the details can be found in Appendix 5.6:

$$f_b(t) = \frac{\Delta f}{f_0} \left( f'_{DC} + f_{DR}t \right) \quad (3.21)$$

Assuming that the slow-time signal envelope is symmetric with respect to the Doppler centroid and that the Doppler bandwidth is confined in a narrow range, a relation between the beat frequency  $f_b$  and the unwrapped Doppler centroid can be obtained by averaging the envelope in the slow-time domain, as follows

$$f_b = f'_{DC} \frac{\Delta f}{f_0} \quad (3.22)$$

The frequency of the beat signal is calculated by transforming the beating signal in the Doppler domain and by evaluating the position of the maximum value of its mean power (average along the range coordinate). The averaging operation makes this estimation robust with respect to the presence of clutter in the real data. By estimating the beating frequency and by inverting the formula (3.22) the unwrapped centroid can be obtained. However, rather than calculate the centroid with the MLBF algorithm (due to the presence of noise and the contribution of extended targets that could cause some estimation errors), in this work, the MLBF is performed only to calculate the Doppler Ambiguity. The Doppler centroid fractional part is instead estimated by using Madsen's algorithm. The unwrapped Doppler centroid is then obtained by using (3.18).

### 3.3 Doppler Rate Estimation

The algorithm for estimating the Doppler rate originates from an algorithm developed for SAR image auto-focus by Li et al. [5]. The algorithm is able to correct the inaccuracies on the knowledge of motion parameters, which, in the SAR case, are typically known a priori. In fact, the SAR Doppler rate can be easily calculated by knowing the sensor parameters  $f_{DR}^{(SAR)} = 2v_r^2/\lambda r_0$  where  $v_r$  is the radial velocity of the sensor,  $\lambda$  is the radar wavelength and  $r_0$  is the reference distance between the radar and the scene centre. Often, however, the measured parameters are affected by errors that lead to an inaccurate estimation of the Doppler rate. For this reason, algorithms have been developed in the literature to correct the parameter estimates, and achieve a better motion compensation solution. The proposed algorithm uses a sub-aperture correlation

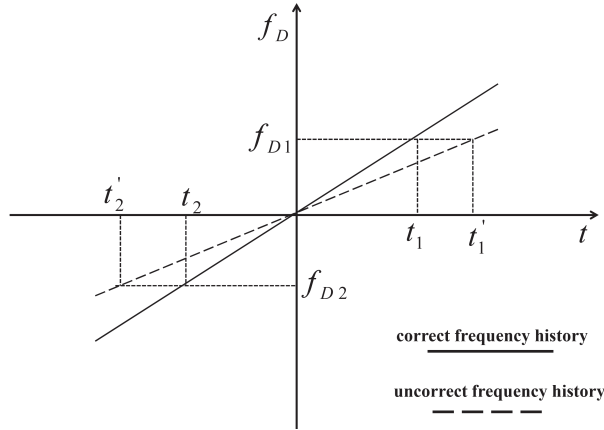


**Figure 3.2:** Slow-Time and Doppler Frequency relation.

method [6]. This method relies on the well known relationship between slow-time coordinates and the Doppler frequency:

$$f_D = f_{DR}t. \quad (3.23)$$

In particular, such an algorithm considers two sub-apertures that are generated by filtering the received signal in the Doppler domain. Specifically, two Doppler sub-bands centered around two frequencies, namely  $f_{D1}$  and  $f_{D2}$ , are defined where the signal is filtered. Once the two sub-apertures are obtained after filtering the original signal, the two SAR images are formed, one per sub-aperture. If the nominal value of the Doppler rate ( $f'_{DR}$ ) is used to compensate the platform motion, a SAR image will be produced that shows a time shift with respect to its correct position. Such time shift can be calculated as follows:

$$\epsilon_k = t'_k - t_k = \frac{f_{Dk}}{f'_{DR}} - \frac{f_{Dk}}{f_{DR}}, \quad k = 1, 2 \quad (3.24)$$

where  $f_{DR}$  is the correct value of the Doppler rate. A de-focusing effect would also be noticed if  $t'_k - t_k \neq 0$  and it would be more pronounced if  $t'_k - t_k$  increases. The two SAR images would show a time shift difference:

$$\Delta t = \epsilon_1 - \epsilon_2 \quad (3.25)$$

when the incorrect Doppler rate is used to compensate the platform motion. Whereas, if  $f'_{DR} = f_{DR}$ , no time shift difference would be present. In fact, a relationship between the time shift difference  $\Delta t$  and the Doppler rate  $f_{DR}$  can be written as follow:

$$\Delta t = (f_{D2} - f_{D1}) \left( \frac{1}{f'_{DR}} - \frac{1}{f_{DR}} \right) \quad (3.26)$$

An estimation of  $f_{DR}$  can be obtained by inverting (3.26). It should be pointed out that  $f_{DR}$  can be estimated by iterating this process, as consecutive iterations improve the estimation of  $\Delta t$ , which is typically attained by cross-correlating the two sub-aperture SAR images and by finding its peak. In the ISAR context, though, the two sub-aperture images are defined in the Range-Doppler domain, which changes some of the aspects of this method. In order to modify this method to apply to the ISAR case, I have recalculated the sub-apertures ISAR image mathematical expressions. Details of such calculation are given in Appendix 5.6. The direct result of the cross-correlation is given in (3.27):

$$\begin{aligned} R_{\Gamma_{l1}, \Gamma_{l2}}(\nu) &= |\Gamma_{l1}(f_d)|^2 \otimes |\Gamma_{l2}(-f_d)|^2(\nu) = \\ &= FT^{-1} \left\{ \Lambda \left( \frac{t}{T_{obs}/2} \right) e^{-j2\pi\delta\frac{T_{obs}}{4}} \Lambda^* \left( \frac{t}{T_{obs}/2} \right) e^{-j2\pi\delta\frac{T_{obs}}{4}} \right\} = \\ &= FT^{-1} \left\{ \left| \Lambda \left( \frac{t}{T_{obs}/2} \right) \right|^2 e^{-j2\pi\delta\frac{T_{obs}}{2}} \right\} = A \left( \frac{\nu - \delta T_{obs}/2}{2/T_{obs}} \right) \end{aligned} \quad (3.27)$$

where  $\nu$  is the Doppler lag and  $\delta$  is the Doppler rate error, defined as follow:

$$\delta = f_{DR} - f'_{DR} \quad (3.28)$$

$\Gamma$  is the sub-aperture Doppler profile defined in Appendix 5.6,  $\Lambda$  is the triangular function defined as follows:

$$\Lambda \left( \frac{t}{T_{obs}/2} \right) = rect \left( \frac{t}{T_{obs}/2} \right) (1 - |t|) \quad (3.29)$$

and  $A$  is the Inverse Fourier Transform of the triangular function square modulus. It is worth noting that the function  $A$  can also be obtained by convolving two *sinc* functions. In the case of a very bright scatterer, its PSF can be considered equivalent to a *sinc* function and therefore, as result, the cross-correlation would produce a concentrated peak at the position  $\delta T_{obs}/2$ . In this case, the result of the search of the cross-correlation peak would return such a position:

$$\hat{\nu}_{max} = \arg \max_{\nu} \{ R_{\Gamma_{l1}, \Gamma_{l2}}(\nu) \} = \delta \frac{T_{obs}}{2} \quad (3.30)$$

Which would lead to an estimation of the Doppler rate error, as follows:

$$\hat{\delta} = \frac{2}{T_{obs}} \hat{\nu}_{max} \quad (3.31)$$

The subsequent estimation of the Doppler rate would be obtained as follows:

$$\hat{f}_{DR} = f'_{DR} + \hat{\delta} \quad (3.32)$$

As already mentioned, this procedure can be iterated by updating  $f'_{DR}$  with  $\widehat{f}_{DR}$ . The iteration may stop when the difference between two consecutive iterations is smaller than a pre-set threshold.

In the ISAR case, it is also important to obtain an initial guess for  $f'_{DR}$ . In this work, such initial guess is estimated by exploiting the relationship between the Doppler bandwidth and the observation time:

$$B_D = f'_{DR} T_{obs} \quad (3.33)$$

The Doppler Bandwidth is here considered as the support of the cross-range power spectral density. This can be measured by using one of the conventional definitions (e.g.  $-3dB$  Doppler bandwidth or 99% of the energy).

### **3.4 Doppler Parameters Estimation Algorithm for SAR Re-Focusing**

In sections 3.2 and 3.3 it has been introduced the methods for estimating the Doppler centroid and Doppler rate, respectively. However, I will detail in this section how these methods are joined together into an algorithm that will be able to refocus non-cooperative targets in Single Look Complex SAR images. In fact, when the SAR image is focused, the SAR processor considers only the relative motion between the platform that carries the sensor and one single point of the illuminated area, which is taken as a reference point of a static observation scene. Therefore, targets that are in motion during CPI, appear de-focused in the SAR image. This phenomenon becomes more evident when the CPI increases. The goal of the proposed algorithm is to estimate the target's Doppler Parameters (centroid and Doppler rate) using a defocused Single Look Complex (SLC) SAR image of it as input data [7]. The refocus algorithm is designed to be applied to both StripMap and Spotlight SAR modes. A block diagram of the proposed algorithm is shown in Figure 3.3. The proposed algorithm takes a crop of the de-focused target from the SLC SAR image as input and then estimates the Doppler centroid by using the algorithm described in section 3.2. The Doppler centroid estimation is performed in two steps. The first step makes use of the algorithm developed by Madsen, which exploits the Fourier Transform relationship between the power spectrum of the signal along the slow-time and its autocorrelation function. The Doppler centroid is estimated as indicated in (3.17). A common practice (see [8]) is for the lag value to be set to  $k = 1$ . This allows the autocorrelation function to be evaluated near the peak, therefore ensuring sufficiently high Signal to Noise Ratio (SNR). If the slow-time sampling rate is below Nyquist, the Doppler centroid estimation may produce an estimate that is a wrapped version of the actual value. For this reason, a second step is performed. The second step evaluates the Doppler ambiguity by applying the MLBF algorithm: a check is carried out

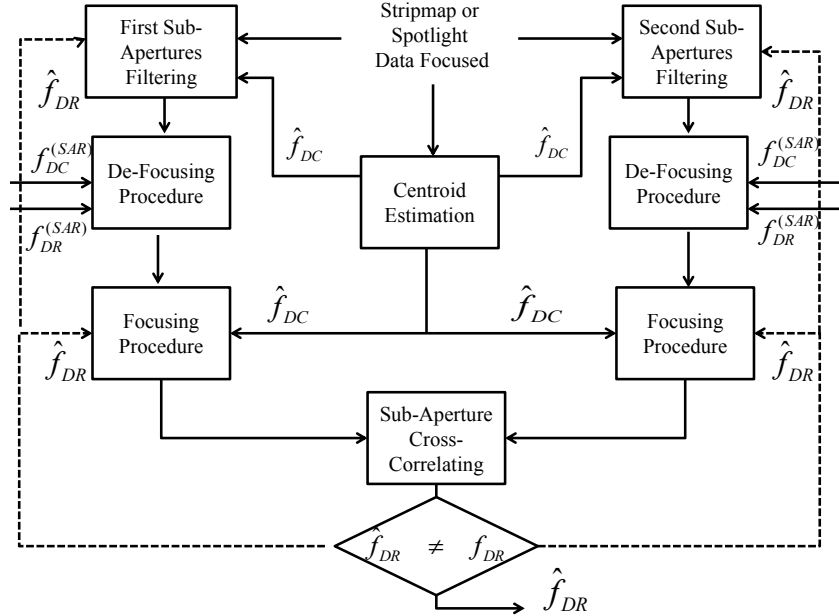


**Figure 3.3:** Block diagram of Doppler Parameters Estimation for SAR re-focusing non-cooperative targets. The dashed line connections indicate that the estimated Doppler rate is updated at each iteration.

that aims at determining if the estimated Doppler centroid is the correct one or if it is wrapped. In the latter case, the Doppler ambiguity factor ( $M$ ) is determined firstly and the Doppler centroid is re-estimated by using (3.18). After estimating the Doppler centroid, the refocus algorithm proceeds with the Doppler rate estimation. As previously explained, the Doppler rate estimation is performed by using an iterative algorithm that seeks to minimize the estimation error, starting from the initial knowledge of a nominal Doppler rate. Such nominal rate is a parameter that is set a priori and, in this case, is the Doppler rate that was used by the SAR processor to carry out the motion compensation procedure to form the original SLC SAR image  $f_{DR}^{(SAR)}$ . At first, the algorithm filters the two sub-apertures that have to be cross-correlated. After doing that, both SAR images obtained with the two sub-apertures are de-focussed by the following de-ramping factor:

$$d(f, t') = e^{+j2\pi \frac{2f}{c} \tilde{R}(t')} \quad (3.34)$$

where the distance term is:

$$\tilde{R}(t') = f_{DC}^{(SAR)} t' + f_{DR}^{(SAR)} t'^2, \quad (3.35)$$

and where  $t'$  is a scaled version of the slow-time. This de-focusing procedure is performed in order to reconstruct the signal back-scattered from a classical ISAR point of view and then the data is processed according to the proposed estimation process.

Subsequently, the two sub-apertures are refocused with the distance term:

$$\widehat{R}(t') = \widehat{f}_{DC}t' + \widehat{f}_{DR}t'^2. \quad (3.36)$$

It should be pointed out that the term  $\widehat{R}(t')$  does not remain constant because the Doppler rate  $\widehat{f}_{DR}$  is updated at each iteration. Finally, the two sub-apertures are cross-correlated to measure the mis-registration parameter  $\Delta t$  defined in (3.23), which allows determining if the estimated Doppler rate, namely  $\widehat{f}_{DR}$  is equal or not to the actual Doppler rate. Consequently, the Doppler rate is updated again. The same steps are repeated as long as the two sub-apertures are mis-registered ( $\Delta t \neq 0$ ).

The scheme described above is the most general scheme for re-focusing of the non-cooperative targets in the focused SAR images. The algorithm can be further improved especially with respect to the computational load and time complexity point of view. In particular, in the Stripmap case, the de-focusing procedure can be performed before the two sub-aperture filtering steps and performed only once. On the other hand, in the Spotlight case, the sub-aperture filtering cannot be performed after the de-focusing due to the well known spectral aliasing [9]. Moreover, if a good pre-estimate of the Doppler rate is available, further improvement in terms of computational load can be achieved because the filtering process can be performed only at the first iteration. More specifically as far as the sub-aperture filtering blocks in Figure 3.3 are concerned, it can be operated by substitution of  $\widehat{f}_{DR}$  with  $f_{DR}^{(SAR)}$ . This substitution leads to a scheme in which the dash line in Figure 3.3 corresponding to the iteration can be limited to the focusing procedure block, without reaching the sub-aperture filtering block diagram.

### 3.4.1 Numerical Results of refocusing SAR moving target

The Doppler Parameter Estimation Algorithm (DPEA) described in the previous section has been tested with SAR data provided by Italian Space Agency (ASI) under a COSMO-SkyMed (CSK) AO Project ID-2143 [10]. Specifically, SLC SAR images of moving maritime targets have been used. In order to validate the proposed technique on Spotlight SAR images, I have proposed two case studies. Some specifications of the Spotlight SAR data are summarized in Table 3.1. The scenario selected is such that the observation time is short enough to guarantee that the target's effective rotation vector is constant [11]. The results obtained by using the proposed estimation algorithm are compared to the results obtained by using the ICBT [1]. The latter has been chosen as a

<i>Parameters</i>	<i>SAR Spotlight Image 1</i>	<i>SAR Spotlight Image 2</i>
PRF, kHz	9.809	9.712
B, MHz	277.510	198.410
$T_{obs,S}$	2.080	2.588
Polarisation	HH	HH
Look	right	right
Direction	descending	ascending

**Table 3.1:** SAR Image Specification

point of reference as it is a well consolidated and effective algorithm for refocusing moving targets in SAR images [12] and [12]. The comparison analysis between the two different algorithms has been carried out by considering:

- image visual quality;
- image contrast;
- entropy of the image intensity;
- peak value of the image intensity;
- computational load.

### First Case Study: Image 1

I have considered the problem of refocusing a SLC SAR image of a moving ship. The image was collected by Cosmo-SkyMed (CSK) in spotlight mode.

As evident from Figure 3.4 the image has been affected by considerable de-focusing. This phenomenon may be due to the fact that the SAR Spotlight mode requires a longer integration time and therefore the effect of the target's motions become more evident in the formation of the synthetic aperture. It should not be dismissed though that the target may have had faster and more complicated motions. The images obtained using the two refocusing techniques are shown in figures 3.5 and 3.6 respectively. From a visual inspection, both images seem to have achieved an optimal result in terms of image refocus. In fact, the scattering centers representative of strong scattering mechanisms are well mapped into single points in the refocussed image. Also, the contours of the ship are much more delineated than in the original image. The results in terms of image contrast, entropy and peak reflect the visual inspection results, as shown in table 3.2. The DPEA achieves, albeit slightly, a lower entropy and the same value of contrast. Furthermore, the DPEA obtains a higher image peak. This is reflected by the higher localization and lower side-lobe-level (SSL) of some scatterers, which can be noticed by comparing Figures 3.5 and 3.6.

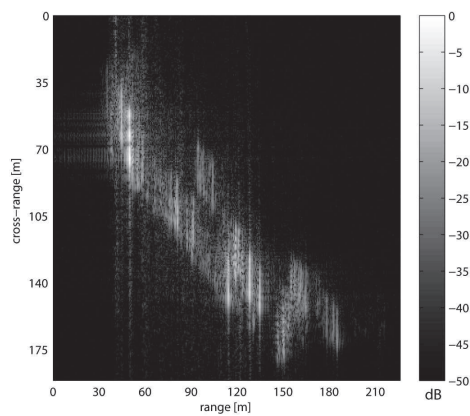


Figure 3.4: First unfocused ship cropped from the SLC image of CSK in Spotlight mode.

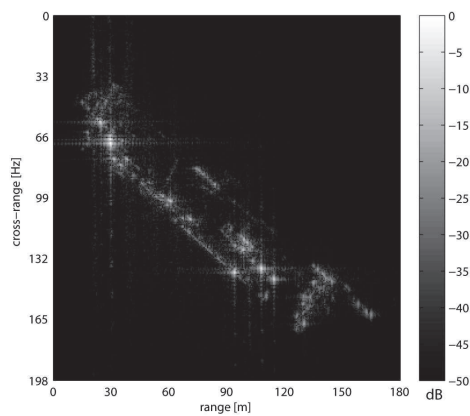


Figure 3.5: First focused ship with Doppler Parameters Estimation Algorithm.

### Second Case Study: Image 2

As a second case study, it can be considered the problem of re-focusing a moving ship in a SLC SAR image, which appears de-focused in both range and azimuth directions (see Figure 3.7). If compared to the first case, the second image shows a greater de-focusing effect. It should not be dismissed though that the target may have had faster and more complicated motions than in the first case study as the result of a higher sea state or because it was undergoing some maneuvers during the observation time. From a visual point of view (see

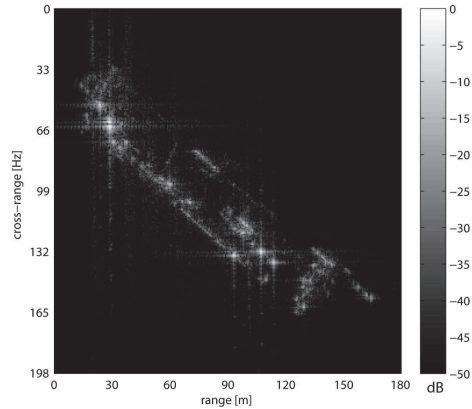


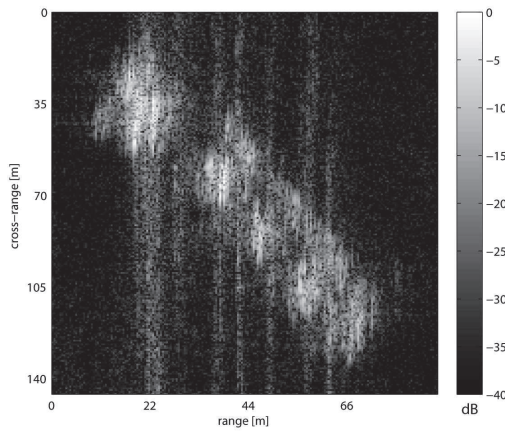
Figure 3.6: First focused ship with Image Contrast Based Technique.

<i>Parameters</i>	<i>SAR processing</i>	<i>DPEA</i>	<i>ICBT</i>
Centroid, Hz	$7.462 \cdot 10^6$	$1.320 \times 10^4$	$7.462 \times 10^6$
Doppler Rate, Hz/s	$3.098 \times 10^3$	$3.105 \times 10^3$	$3.593 \times 10^4$
Constrast	3.641	4.329	4.329
Entropy	7.774	6.350	6.359
Peak	$3.757 \times 10^3$	$1.015 \times 10^4$	$8.866 \times 10^3$
Computational load, s		1.934	2.980

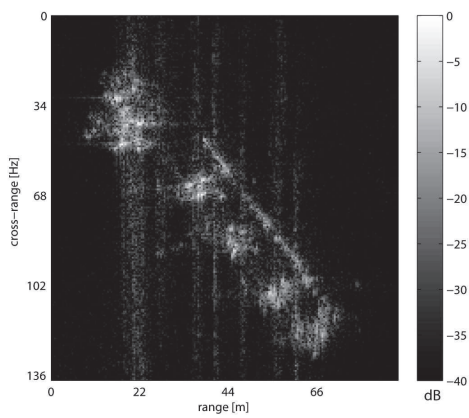
Table 3.2: Comparison Parameters for Image 1

Figure 3.8), the image obtained by using the DPEA seems very well focused, as highlighted by the vessel contours. In addition, the DPEA also reduces the spread along the azimuth coordinate, as shown in the original SLC SAR image. Indeed, the vessel appears with a thinner outline. Furthermore, the image focus achieved by the DPEA has enhanced the Signal to Clutter Ratio (SCR).

On the other hand, the ICBT (see Figure 3.9) obtains very analogous results to those obtained with the DPEA. Results in Figure 3.8 and Figure 3.9 are very similar. The slight differences are only due to the different parameter estimation obtained by the two algorithms, namely the ICBT and the proposed one. When looking at the results shown in table 3.3, the ICBT shows, although few decimal values, a lower value of the image contrast, indeed, the contrast is the parameter that the ICBT aims to a maximize. As far as the entropy is concerned [13], again, the DPEA seems to obtain, although for a few of decimal digits, a lower entropy. In terms of image peak, the DPEA produces the highest value, indicating its ability to focus well with respect one point of the target.



**Figure 3.7:** Second unfocused ship cropped from the SLC image of CSK in spotlight mode.



**Figure 3.8:** Second focused ship with Doppler Parameters Estimation Algorithm.

Considering such a point as a reference point on the target, this indicates the DPEA's effectiveness to track the Doppler centroid and Doppler rate (radial velocity and acceleration) of the target. These results prove the effectiveness of the DPEA.

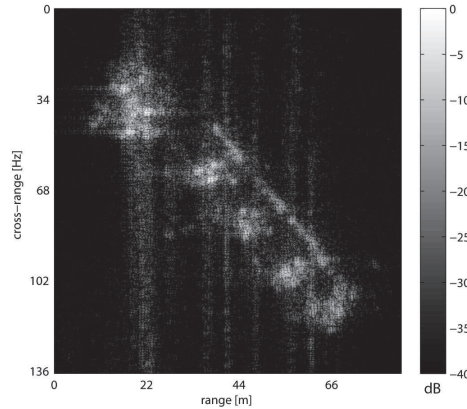


Figure 3.9: Second focused ship with Image Contrast Based Technique.

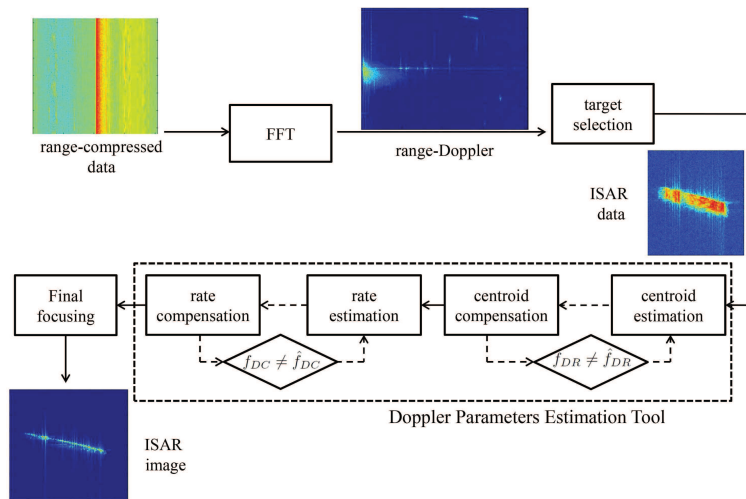
<i>Parameters</i>	<i>SAR processing</i>	<i>DPEA</i>	<i>ICBT</i>
Centroid, Hz	806.970	464.305	806.915
Doppler Rate, Hz/s	$3.895 \times 10^3$	$3.892 \times 10^3$	$3.884 \times 10^3$
Constrast	1.871	2.014	2.020
Entropy	8.667	8.070	8.063
Peak	$1.281 \times 10^3$	$2.646 \times 10^3$	$2.492 \times 10^3$
Computational load, s		1.213	1.92

Table 3.3: Comparison Parameters for Image 2

### 3.5 Doppler Parameters Estimation Algorithm for ISAR Static Sensor

In this section I will describe how to apply the Doppler parameters estimation technique to a classical ISAR system where the sensor is stationary and the only motion which induces the Doppler variation signal is the motion of the target. In particular, I propose a novel algorithm which is able to generate high resolution ISAR images in the Range-Doppler domain for maritime target observed by FMCW radar. In fact, in the last few years, in order to be more appealing with different scenarios, radar imaging sensors are required to be low-cost, low-powered and compact. Coherent pulsed radars, which require high peak transmission power, do not account for these requirements as much as the FMCW systems which operate with constant low transmission power. As demonstrated in the past [14], the combination of FMCW sensors with SAR technique led to lightweight cost-effective imaging sensors of high

resolutions. The low-cost and the ability to form high-resolution images from remote sensors in all day/all weather conditions has boosted the use of FMCW system as radar imaging in several applications, spanning from risk monitoring associated to human-induced and natural hazards to homeland security applications. So, it has been described a novel algorithm for generating high resolution ISAR images by readapting the previous Doppler parameters estimation technique. A block scheme of the proposed algorithm is shown in Figure 3.10. As can be seen, the range compressed radar data, in the range-slow-time



**Figure 3.10:** Block diagram of Doppler Parameters Estimation and compensation for focusing non-cooperative targets for static ISAR system.

domain, are transformed by the FFT algorithm in the range-Doppler domain; this preliminary operation is necessary for the selection of the moving target to be imaged. In fact, the FMCW radar system is typically characterized by a couple of antennas (one for transmitting and one for receiving) with a wide fixed beamwidth of about  $40^\circ$  along the azimuth and the elevation directions; therefore, for distinguish the moving targets of interest from the static clutter, the only possible solution is to transform the radar data in Doppler domain and exploit the Doppler effect (described in the first Chapter), which induces a relative Doppler frequency component due to the relative motion between the radar and the moving target. An example is given in Figure 3.11; as evident, the moving target which is characterized by a mean Doppler frequency of  $-270$  [Hz] is clearly distinguishable from the static clutter whose spectrum is centered around the zero-Doppler interval. After the FFT, the target is selected and cropped from the radar observed scene and it can be elaborated by the the Doppler Parameters Estimation Tool. As illustrated in Figure 3.10,

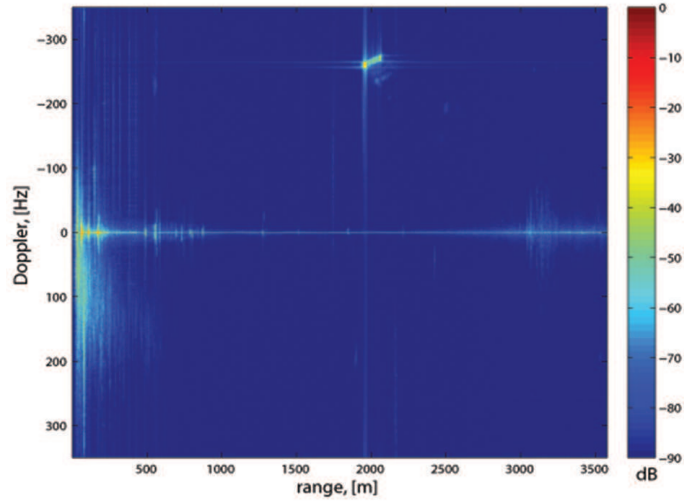


Figure 3.11: Range-Doppler FMCW radar data.

the Doppler Parameters Estimation Tool, first of all, calculates the Doppler centroid by exploiting the procedure described in the section 3.2, and, then compensates the estimated centroid in the target phase history; subsequently, in order to take into account the residual centroid component, the estimating process is iterated until the difference between two consecutive iterations is smaller than a pre-set threshold. After, the Doppler parameters Estimation Tool performs the Doppler rate estimation by exploiting the Doppler rate estimating procedure, described in the section 3.3, and then, similarly to the centroid compensation, the rate procedure is iterated for compensating also the residual rate components. Finally, the algorithm ends with the “Final focusing” blocks for generating the ISAR target image.

### 3.5.1 Numerical Results of focusing ISAR moving targets

The Doppler Parameter Estimation Algorithm for static sensor, described in the previous section 3.5, has been tested with a maritime X-band radar system data-set owned by Centre for Maritime Research & Experimentation (CMRE) in the Gulf of La Spezia (Italy) (see Figure 3.12).

The sensor has two small flat panel antennas with  $40^\circ$  beamwidth in the horizontal plane, with a fixed field of view. Both antennas work in the two polarizations, linear horizontal and linear vertical, being the first one used for transmit and the second one for receive, allowing the acquisition of full polarimetric measures. The main radar parameters are illustrated in Table 3.4. The results obtained by using the proposed estimation algorithm are again com-

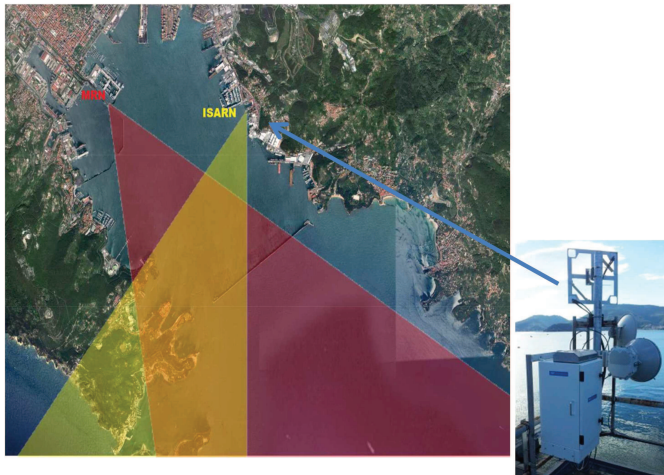


Figure 3.12: View of the test site area in the Gulf of La Spezia (Italy).

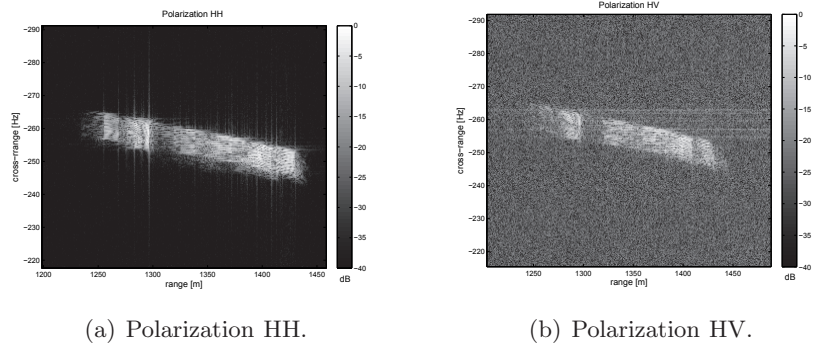
Parameters	Specification
Carrier Frequency	9.6 GHz
Bandwidth	Adjustable up to 300 MHz
Resolution	Adjustable up to 0.50 m
Antenna type	Fixed Flat Panel
Angular Aperture Azimuth	40°
Angular Aperture Elevation	40°
Polarization	Linear Vertical and Horizontal
Antenna Gain	12 dBi
Transmitted Power	Adjustable 50 mW - 5 W
PRF	Adjustable 350 Hz - 10 kHz

Table 3.4: Sensor Specifications.

pared with the ICBT by analyzing the same quality parameters defined in the section 3.4.1 as: visual inspection, contrast, entropy, peak and computational load.

### First Case Study

I have considered the problem of focusing moving ships by a static FMCW radar system in full polarization mode. As evident from Figure 3.13 the image is affected by considerable de-focusing, in fact, the range-Doppler target image



**Figure 3.13:** First unfocused ship cropped from the radar data in Polarization HH and HV

shows a significant blurring and thus it is not possible to measure the vessel sizes; as matter of fact, the different points scatterers, which represent the ship, are mixed together and they are also affected by a very large migration so that any kind of classification is not feasible. The images obtained using the two autofocusing technique are shown in Figures 3.14 and 3.15 respectively.

From the visual point of view, both the images, relevant to the polarizations

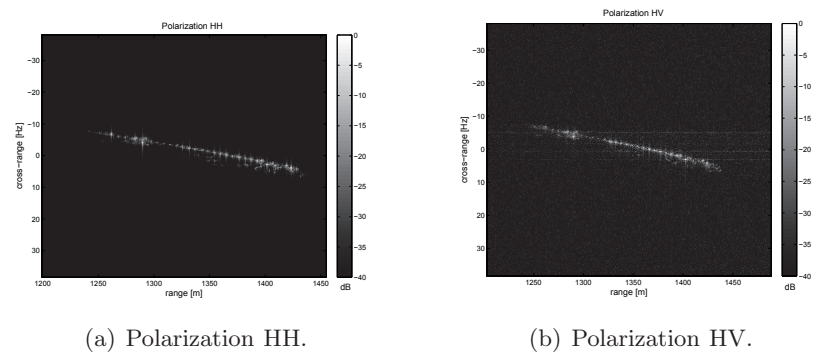
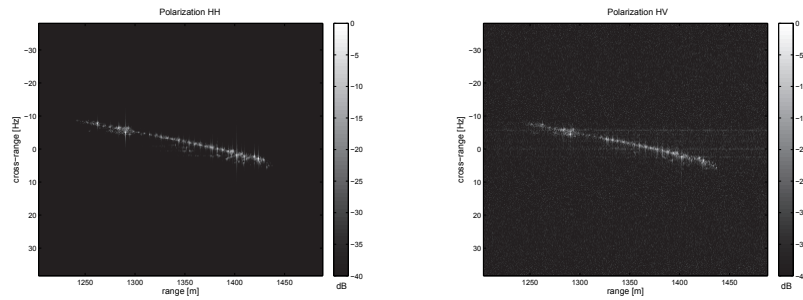


**Figure 3.14:** First focused ship with DPEA in Polarization HH and HV

$HH$  and  $HV$  respectively, seem to have achieved a very good result in terms of image focusing. In fact, the single points representative of strong scattering mechanisms are well recognizable in the focussed images. Also, the shape of the ship is much more delineated than in the original image. The results in terms of image contrast, entropy and peak reflect the visual inspection results, are shown in tables 3.5 and 3.6.

The DPEA achieves, albeit slightly, a lower contrast and the same value



(a) Polarization HH.

(b) Polarization HV.

**Figure 3.15:** First focused ship with ICBT in Polarization HH and HV

<i>Parameters</i>	<i>Raw Data</i>	<i>DPEA</i>	<i>ICBT</i>
Contrast	2.773	4.737	4.778
Entropy	8.738	5.814	5.814
Peak	$7.289 \times 10^6$	$4.980 \times 10^7$	$4.328 \times 10^7$
Computational load, s		0.757	8.722

**Table 3.5:** Comparison Parameters for I case study Polarization HH

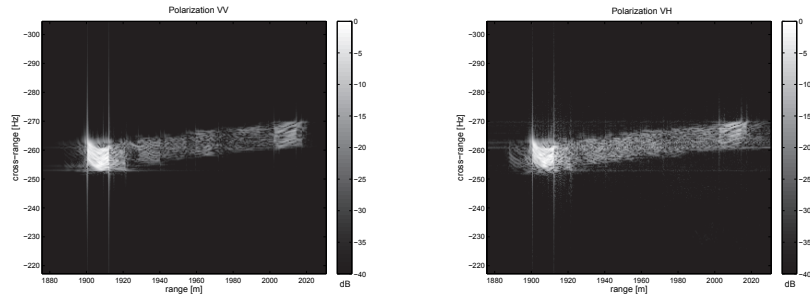
<i>Parameters</i>	<i>Raw Data</i>	<i>DPEA</i>	<i>ICBT</i>
Contrast	0.800	0.945	0.945
Entropy	10.826	9.843	9.841
Peak	$7.796 \times 10^5$	$4.387 \times 10^6$	$4.249 \times 10^6$
Computational load, s		0.720	10.943

**Table 3.6:** Comparison Parameters for I case study Polarization HV

of entropy. Furthermore, the DPEA obtains a higher image peak. The main difference between the two processing techniques is relative to the computational load; in fact, the DPEA achieves the focusing of the target in a very low processing time compared to ICBT technique. This fact is essentially due to exhaustive searching of focusing parameters for the ICBT algorithm.

### Second Case Study

As a second case study, it has been considered the problem of focusing a moving ship with different polarizations respect to the previous case (see Figure 3.16). If compared to the first case, the second image shows a greater range-walk effect which causes a very high range migration. From the visual

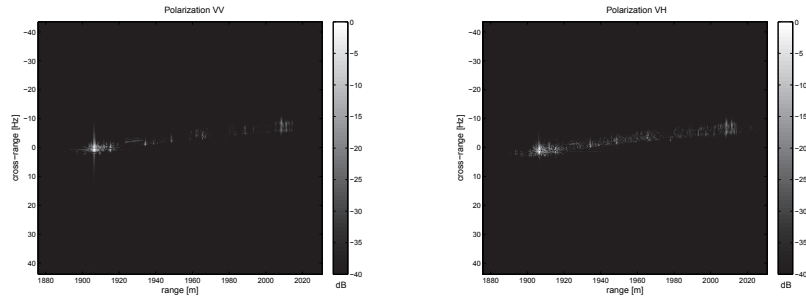


(a) Polarization VV.

(b) Polarization VH.

**Figure 3.16:** First unfocused ship cropped from the radar data in Polarization VV and VH

inspection (see Figure 3.17), the image obtained by using the DPEA seems very well focused, as highlighted by the thinner outline. Indeed, the image focus achieved by the DPEA has enhanced the SCR.



(a) Polarization VV.

(b) Polarization VH.

**Figure 3.17:** First focused ship with DPEA in Polarization HH and HV

On the other hand, comparing the Figures 3.17 and 3.18 both the techniques obtain very similar results, but, if I consider the quality parameters described in tables 3.7 and 3.8 some differences can be noted.

In fact, the ICBT shows, an higher value of contrast, a lower entropy and an higher peak (as shown in Table 3.7), and for this reason the results obtained by the ICBT are slightly better than DPEA results. The improvements, in terms of focusing quality parameters, is paid in terms of computational load; in fact, by comparing the processing time of the two autofocus techniques, I may notice that the DPEA algorithm reaches similar results with a time efficiency of about the 90%. These results prove the effectiveness of the proposed DPEA

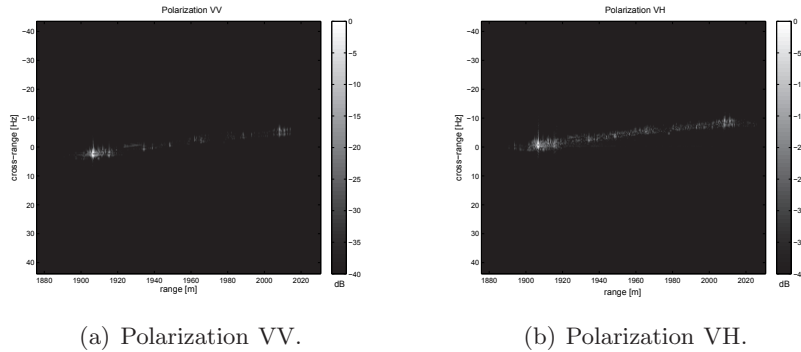


**Figure 3.18:** First focused ship with ICBT in Polarization VV and VH

<i>Parameters</i>	<i>Raw Data</i>	<i>DPEA</i>	<i>ICBT</i>
Contrast	4.806	8.578	9.469
Entropy	6.996	4.235	4.012
Peak	$2.965 \times 10^8$	$1.705 \times 10^9$	$1.819 \times 10^9$
Computational load, s		0.671	9.615

**Table 3.7:** Comparison Parameters for II case study Polarization VV

<i>Parameters</i>	<i>Raw Data</i>	<i>DPEA</i>	<i>ICBT</i>
Contrast	3.196	4.514	4.776
Entropy	7.569	5.186	5.090
Peak	$2.000 \times 10^7$	$1.298 \times 10^8$	$1.217 \times 10^8$
Computational load, s		0.661	9.795

**Table 3.8:** Comparison Parameters for II case study Polarization VH

and demonstrate also the ability of this new technique to process the ISAR data in real time, presenting itself as very efficient ISAR autofocusing technique.

## 3.6 Acknowledgment

The author would like to thank the Italian Space Agency ASI for providing under the CSK AO Project ID-2143 the SAR data on which estimation techniques have been tested. In addition, the authors also thank the project PON “HArBour traffic OpTimizAtion SysTem” (HABITAT) financed by the Italian Ministry of Transport and Infrastructure. Furthermore, the author would like also to thank the Centre for Maritime Research & Experimentation of the

North Atlantic Treaty Organization (CMRE-NATO) for providing the ISAR data relative to La Spezia harbor by which the proposed Autofocus technique has been tested.

# References

- [1] M. Martorella, F. Berizzi, and B. Haywood, "Contrast maximization based technique for 2-d isar autofocusing," *IEE Proc. Radar Sonar Navig.*, vol. 152, no. 4, pp. 253–262, 2005.
- [2] C. Noviello, G. Fornaro, M. Martorella, and D. Reale, "A novel approach for motion compensation in isar system," *EUSAR 2014*, 2014.
- [3] S. N. Madsen, "Estimating the doppler centroid of sar data," *Aerospace and Electronic Systems, IEEE Transactions on*, vol. 25, no. 2, pp. 134–140, 1989.
- [4] F. Wong and I. G. Cumming, "A combined sar doppler centroid estimation scheme based upon signal phase," *Geoscience and Remote Sensing, IEEE Transactions on*, vol. 34, no. 3, pp. 696–707, 1996.
- [5] F.-K. Li, D. N. Held, J. C. Curlander, and C. Wu, "Doppler parameter estimation for spaceborne synthetic-aperture radars," *Geoscience and Remote Sensing, IEEE Transactions on*, no. 1, pp. 47–56, 1985.
- [6] J. R. Bennett, I. G. Cumming, P. R. McConnell, and L. Gutteridge, "Features of a generalized digital synthetic aperture radar processor," in *International Symposium on Remote Sensing of Environment, 15 th, Ann Arbor, MI*, 1981, pp. 271–290.
- [7] C. Noviello, G. Fornaro, and M. Martorella, "Focused sar image formation of moving targets based on doppler parameter estimation," *Geoscience and Remote Sensing, IEEE Transactions on*, vol. 53, no. 6, pp. 3460–3470, 2015.
- [8] R. Bamler, "Doppler frequency estimation and the cramer-rao bound," *Geoscience and Remote Sensing, IEEE Transactions on*, vol. 29, no. 3, pp. 385–390, 1991.
- [9] R. Lanari, M. Tesauro, E. Sansosti, and G. Fornaro, "Spotlight sar data focusing based on a two-step processing approach," *Geoscience and Remote Sensing, IEEE Transactions on*, vol. 39, no. 9, pp. 1993–2004, 2001.

- 
- [10] F. Covello, F. Battazza, A. Coletta, G. Manoni, and G. Valentini, “Cosmoskymed mission status: Three out of four satellites in orbit,” in *Geoscience and Remote Sensing Symposium, 2009 IEEE International, IGARSS 2009*, vol. 2. IEEE, 2009, pp. II-773.
  - [11] C. Noviello, G. Fornaro, M. Martorella, and D. Reale, “Isar add-on for focusing moving targets in very high resolution spaceborne sar data,” in *Geoscience and Remote Sensing Symposium (IGARSS), 2014 IEEE International*. IEEE, 2014, pp. 926–929.
  - [12] M. Martorella, E. Giusti, F. Berizzi, A. Bacci, and E. Dalle Mese, “Isar based technique for refocusing non-cooperative targets in sar images,” *IET Radar, Sonar & Navigation*, vol. 6, no. 5, pp. 332–340, 2012.
  - [13] L. Xi, L. Guosui, and J. Ni, “Autofocusing of isar images based on entropy minimization,” *Aerospace and Electronic Systems, IEEE Transactions on*, vol. 35, no. 4, pp. 1240–1252, 1999.
  - [14] A. Meta, P. Hoogeboom, and L. P. Ligthart, “Signal processing for fmcw sar,” *Geoscience and Remote Sensing, IEEE Transactions on*, vol. 45, no. 11, pp. 3519–3532, 2007.

## Chapter 4

# Synthetic Aperture Radar Principles and Interferometry

*The use of microwaves radiation allows imaging independently of weather conditions and during night and day. The radar principle is rather simple: the system merely transmits a signal and measures the electric field backscattered by the illuminated area; the delay is directly related to the distance between the target and the sensor, while the amplitude of the received signal is somehow an indicator of the backscattering characteristics, i.e. of the physical and electromagnetic properties of the observed scene.*

*The Synthetic Aperture Radar (SAR) consists of moving the radar along a straight trajectory thus allowing creating a 2-D map of the scene. This apparently simple extension requires however a considerable amount of signal processing and results in an unconventional imaging geometry. An interesting application of SAR imagery is the Interferometry and particularly Differential Interferometry that, by processing two or more images acquired from slightly different position at different times, allows reconstructing the height distribution and monitoring possible movements of the surface.*

### 4.1 Synthetic Aperture Radar principle

A SAR system consists of a side-looking radar on a moving platform, such as an airplane or a satellite. The three-dimensional (3-D) reference system of a SAR sensor is cylindrical and it is defined as (see Figure 4.1):

- $x$ : *azimuth*, the flight direction of the sensor, also called the *along-track* direction;

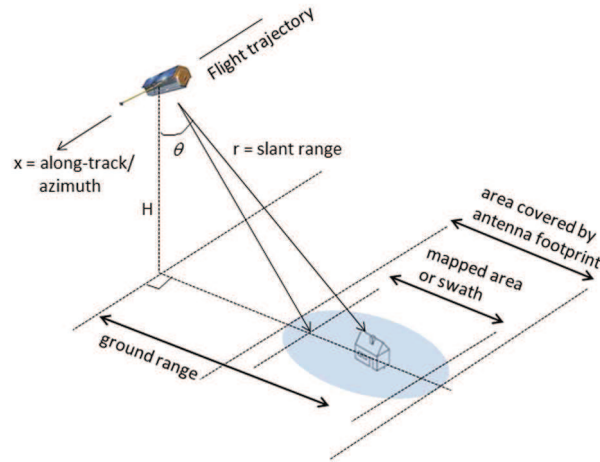


Figure 4.1: Radar side-looking imaging geometry

- $r$ : range, LOS direction of the antenna, also referred to as slant range;
- $\theta$ : looking angle, i.e. perpendicular to the azimuth-range plane.

The SAR sensor is assumed moving with constant velocity along a straight trajectory along the *azimuth* direction ( $x$ -axis); it is imaging along the range direction ( $r$ -axis) tilted of an angle  $\theta$  respect to the nadir (side-looking mode).

SAR is able to obtain images of the observed scene, which are available in the two conventional radar coordinates *azimuth* and *range*. The sensor performs a mapping of the observed scene with different principles along each direction:

- *Azimuth*: Synthetic aperture principle enabled by the movement of the sensor;
- *Range*: Radar ranging principle, i.e. the transmitter emits pulses, e.g. *chirps*. These pulses are reflected from objects on the ground and part of the energy reaches again the receiver. Different objects can be resolved if they have a different distance with respect to the sensor, i.e. their echoes show a different two-way travel time.

It is worth pointing out that along the *slant height* direction, also called *elevation* direction, which is the defined as the direction orthogonal to the radar LOS, SAR is not able to distinguish targets sharing the same azimuth-range ( $x, r$ ) coordinates but with different elevation positions: their radar returns will interfere within the SAR pixel image. This gives rise to geometric distortion effects (see Section 4.1.2).

The pixels in a SAR image can be identified by an azimuth and a range coordinate; they contain complex-valued information relative to the backscattering

response of the scene.

On the two directions SAR has different spatial resolution, which is defined as the minimum distance that two scatters must have in order to be resolved.

Concerning the range resolution  $\Delta r$ , since the echo backscattered from a point target has the same duration in time  $\Delta T$  (in units of time) of the transmitted signal, two different targets can be distinguished only if their echoes are not superimposed in time, hence the range resolution is [1,2]:

$$\Delta r = \frac{c\Delta T}{2} = \frac{c}{2B_W} \quad (4.1)$$

being  $B_W$  the frequency bandwidth of the transmitted radar pulse and  $c$  the speed of light. The range resolution is independent from the distance between the sensor and the target. From (4.1), range resolutions of the order of some meters can be obtained by transmitting pulses with duration of the order of  $\Delta T \approx 10^{-9}$ s. From practical considerations such a pulse cannot be easily produced due to the need of high peak power and also for the very large bandwidth. A way to circumvent this limitation consists of transmitting a linear frequency modulated signal, i.e. the *chirp* (see Figure 4.2):

$$p(t) = e^{-j\frac{\alpha t^2}{2}}, \quad (4.2)$$

where  $\alpha$  is the *chirp rate*. The chirp bandwidth is given by:

$$\Delta f = \frac{\alpha\Delta T}{2\pi} \quad (4.3)$$

The chirp bandwidth is directly proportional to chirp duration: the more the pulse is extended in the time domain, the greater is its bandwidth. The chirp allows having high range resolutions thanks to its wide bandwidth and also, at the same time, to maintain low peak power, thanks to the high duration of the signal.

It is evident that the energy of the chirp signal is spread over a large duration. Then, in order to compress the signal there is the necessity to use a post-processing step in the receiver, usually referred to as *range or pulse compression*, which is based on a matching filter.

The given definition of range corresponds to the slant range direction. In *ground range*, i.e.  $r_g$ , which is the projection of the slant range direction on the ground, the resolution is given by  $\Delta r_g = \Delta r / \sin(\theta)$ , i.e. the ground range resolution is coarser than the slant range resolution.

For example, the satellites of the COSMO-SkyMed constellation transmit a chirp with a duration of  $\Delta T = 40\mu s$  with bandwidth  $B_W = 120MHz$  resulting in a range resolution of  $\Delta r = 1,25m$  and a ground range resolution of  $\Delta r \approx 2,92m$ .

Concerning the azimuth resolution, SAR is different from conventional radar

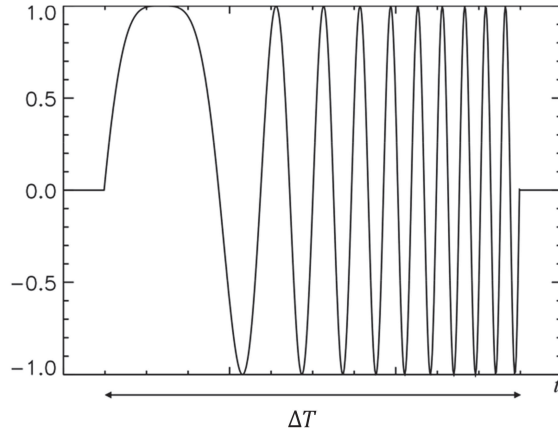


Figure 4.2: Chirp signal

systems. In conventional radar systems two targets at a given range position  $r_0$  from the radar cannot be detected if they are both located in the azimuth antenna beam, or rather the azimuth resolution  $\Delta x$  is just given by the amplitude of the antenna footprint  $X$  [1, 2]:

$$\Delta x = X = \frac{\lambda}{L} r_0, \tag{4.4}$$

where  $\lambda$  is the signal wavelength (which is typically several centimetres) and  $L$  is the physical antenna length along the azimuth direction. This means that in order to increase the azimuth resolution, it is necessary to use larger antennas and working at a small distance from the scatterers. These requirements are not practically realizable.

SAR systems take advantage from the fact that a generic scatterer point remains in the antenna beam for a significant period of time, i.e. the time the sensor takes to shift a distance equal to the antenna footprint. So a scatterer point is observed by the SAR from different positions during the movement of the antenna along its orbit. Hence by exploiting the movement of the platform along the azimuth direction an antenna array can be synthesized: instead of using a very long antenna in azimuth, the same small antenna can implement during the flight different elements of an antenna array in the different time instants.

In Figure 4.3 the synthesis concept is explained from the practical point of view: given the antenna footprint  $X$ , the target is imaged from the azimuth beam during a flight path of the platform of extension  $X$ . Better, the target is imaged from the sensor during a time interval defined as *integration time*, which is the time required to translate the along-track beam of a distance equal to  $X$ . Hence during this time interval, the target is seen from the radar at differ-

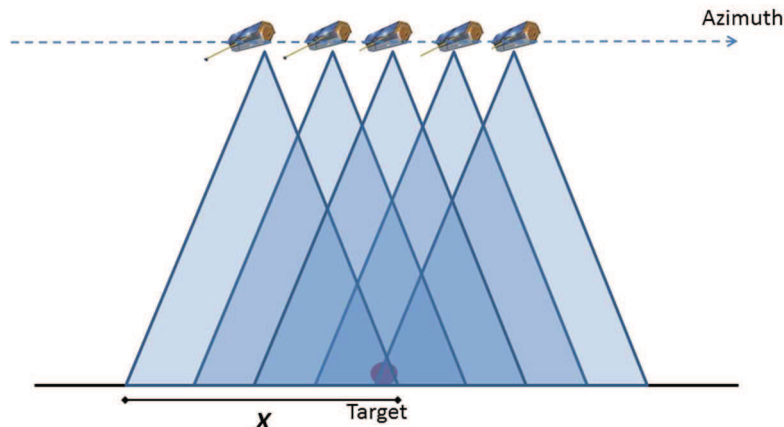


Figure 4.3: Synthetic aperture principle

ent positions: the synthesis is carried out by coherently combining, offline, all the backscattered echoes. In this way a larger antenna of dimension  $L_{sa} = X$  (subscript *sa* stands for *synthetic aperture*) is synthesized. This leads to a SAR azimuth resolution given by:

$$\Delta x = \frac{\lambda}{2L_{sa}} r_0 = \frac{L}{2}. \quad (4.5)$$

Hence the azimuth resolution results to be of the same order of the physical antenna length along the azimuth direction  $L$  and, more importantly, it does not depend on the range distance  $r_0$  between the sensor and the target. For example the azimuth resolution of the COSMO-SkyMed satellites, is about  $\Delta x \approx 2,8m$ , being the azimuth antenna size  $L \approx 5,6m$ .

It would appear that a finer resolution can be obtained by simply making the real antenna length  $L$  very small. This is true, but some ambiguity conditions place certain limits on this (in particular related to the *PRF* and the ground coverage capability of the SAR system). A compromise between these and other involved parameters is necessary [3].

#### 4.1.1 SAR processing

A brief explanation of SAR processing is provided. A comprehensive description of the overall SAR image processing step (usually referred to as *focusing procedure*) is outside the scope of this work; the reader can refer back to [1, 2] for a more detailed one.

Let consider a radar system working with a single antenna in a synchronized transmit/receive mode and, for sake of simplicity, suppose it transmits and

receives the same pulse at the same position (*stop and go approximation*). First of all, to investigate the radar signal characteristics, referring to the recorded echo (*raw data*) corresponding to a generic target of SAR coordinates  $(x, r)$  at a distance  $R_n$  from the sensor. Accordingly, let assume that the SAR system is transmitting at a generic time instant  $t_n - \Delta T/2$  the following pulse with complex representation:

$$f_{tx}(t) = \exp(j2\pi f_0 t) p(t - t_n) \text{rect}\left(\frac{t - t_n}{\Delta T}\right), \quad (4.6)$$

where  $p(t - t_n)$  describes the signal modulation,  $\Delta T$  is the duration of the transmitted pulse and  $f_0$  is the carrier frequency.

As explained in the Section 4 a chirp pulse (see equation (4.2)) is used. Hence by substituting (4.2), the expression of the transmitted signal becomes:

$$f_{tx}(t) = \exp(j2\pi f_0 t) \exp\left[\frac{-j\alpha(t - t_n)^2}{2}\right] \text{rect}\left(\frac{t - t_n}{\Delta T}\right). \quad (4.7)$$

The backscattered signal, which is received onboard when the sensor lies in the azimuth position  $x' = vt_n$ , takes into account the transmitted/received signal time delay  $t_D = 2R_T/c$ . By neglecting the fast-varying ( $\exp(j2\pi f_0 t)$ ) term (because it is cancelled out at the receiver through a heterodyne process) it can be expressed as:

$$\begin{aligned} f_{rx}(x' - x, t - t_n, r) = \rho(x, r) \exp(-j2\pi f_0 t_D) \exp\left[\frac{-j\alpha(t - t_n - t_D)^2}{2}\right] \cdot \\ \cdot \text{rect}\left(\frac{t - t_n - t_D}{\Delta T}\right) \text{rect}\left(\frac{x' - x}{X}\right), \end{aligned} \quad (4.8)$$

where  $\rho$  is the reflectivity function of the target, which indicates the amount of energy backscattered by the target toward the sensor, and  $X$  is the antenna footprint.

In order to manage with spatial coordinates only, the coordinate transformation  $t' = t - t_n = 2r'/c$  is necessary, thus obtaining:

$$\begin{aligned} f_{rx}(x' - x, r' - r, r) = \rho(x, r) \exp\left(-j4\pi \frac{R_T}{\lambda}\right) \exp\left[-\frac{j2\alpha}{c^2}(r' - R_T)^2\right] \cdot \\ \cdot \text{rect}\left(\frac{r' - R_T}{c\Delta T/2}\right) \text{rect}\left(\frac{x' - x}{X}\right), \end{aligned} \quad (4.9)$$

where  $\lambda = c/f_0$  is the carrier wavelength.

It can be observed that the signal in (4.9), commonly referred to as *raw data*, represents an estimate of the measured reflectivity pattern  $\rho$  relevant to the point target. Furthermore it can be noted in (4.9) the presence of two rect functions: the first one has an extension equal to  $c\Delta T/2$  and is centered in  $R_T$

(which depends on the azimuth coordinate, as it will be shown later), while the other one has an extension equal to  $X$  and is centered in the target azimuth coordinate  $x$ . They identify the range and azimuth resolution of the *raw data*, respectively (see equations (4.1) and (4.4)).

In a SAR signal processor specific operations are required to convert the *raw data* (i.e. the acquired data) into an interpretable image; they are referred to as *SAR focusing* operations. In fact a SAR raw data is not an image yet, since point targets are spread out in range and in azimuth. The spreading in range is due to the use of the chirp signal. The spreading in azimuth is due the fact that the echo of a point target is contained in many received radar pulses (see Figure 4.3). The core of SAR processor is to correctly and coherently combine all these echo referred to the same target point received during the integration time. The focusing is needed both in azimuth and in range dimension, in order to achieve the SAR image with improved resolution with respect to the raw data.

It is worth noting in (4.9) the *chirp* signal is:

$$c_p(r') = \exp \left[ -\frac{j2\alpha}{c^2}(r' - R_T)^2 \right] \text{rect} \left( \frac{r' - R_T}{c\Delta T/2} \right), \quad (4.10)$$

with a *chirp rate*:

$$\alpha' = \frac{4\alpha}{c^2} \quad (4.11)$$

with a time duration equal to  $\Delta T' = c\Delta T/2$ .

The range compression, or *range focusing*, is achieved through a matched filter, i.e. with the convolution of the received signal with:

$$l_f(r') = \exp \left[ \frac{j2\alpha}{c^2}r'^2 \right] \text{rect} \left( \frac{r'}{c\Delta T/2} \right). \quad (4.12)$$

It can be demonstrated that the matched filtering of a generic chirp signal with *chirp rate*  $\alpha$  and duration  $\Delta T$  results in:

$$i_f(t) * c_p(t) = \text{sinc} \left( \frac{\pi}{\Delta}t \right), \quad (4.13)$$

where the generic term  $\Delta$  is given by:

$$\Delta = \frac{2\pi}{\alpha\Delta T}. \quad (4.14)$$

It represents the time interval in which the signal power is reduced, at most, at one half of its maximum. It also demonstrates the “*compression*” effect, which leads to a signal of duration  $\Delta \ll \Delta T$ .

Hence, after some calculation [1], the range compressed signal will be:

$$\begin{aligned} h(x', r') = f_{rx}(\cdot) * l_f(\cdot) = \rho(x, r) \exp \left( \frac{-j4\pi R_T}{\lambda} \right) \cdot \\ \cdot \text{sinc} \left[ \frac{\pi}{\Delta r}(r' - R_T) \right] \text{rect} \left( \frac{x' - x}{X} \right), \end{aligned} \quad (4.15)$$

with  $\text{sinc}(x) = \sin(x)/x$ . By recalling (4.14) in which the range chirp rate in (4.11) has been substituted, as follow:

$$\Delta r = \frac{2\pi}{\left(\frac{4\alpha}{c^2}\right)\left(\frac{c\Delta T}{2}\right)} = \frac{\pi c}{\alpha\Delta T} = \frac{c}{2\Delta f}, \quad (4.16)$$

where  $\Delta f$  is given by (4.3).

The appearance of the sinc function in the range compressed signal in (4.15) clearly explains the use of the term *compression*: for each point target, the raw data in (4.9) has a temporal extension of  $\Delta T$ ; after the convolution with the reference function in (4.12), the duration reduces to  $1/\Delta f$ , thus leading to an improved range resolution  $\Delta r$  in (4.16), which is approximately equal to half of the extension of the main lobe of the sinc function.

It is worth noting that the signal in (4.15) is characterized by an effect known as RCM. It is due to the fact that the sinc is not centered in correspondence of the target range coordinate  $r$ , but in correspondence of  $R_T$ , which measures the distance between the sensor (having coordinate  $(x', 0)$ ) and the target (having coordinate  $(x, r)$ ) and hence depends on the range coordinate, as well as on the difference between the azimuth coordinate  $x$  of the sensor and of the target i.e.  $x' - x$ . In fact the movement of the platform introduces a range variation given by:

$$R_T = R_T(x' - x, r) = \sqrt{(x' - x)^2 + r^2} \cong r + \frac{(x' - x)^2}{2r}. \quad (4.17)$$

This means that for different positions of the sensor, the same target will be compressed along a parabolic path in azimuth. The parabolic distortion effect is referred to as RCM. In absence of any compensation of the RCM, the simple independent focusing explained before leads to a defocusing in azimuth. The RCM compensation [4] is compulsory to reduce/eliminate the defocusing: practically the curvature is corrected to a straight line before azimuth compression. Hence the range focused signal in (4.15) becomes:

$$h(x', r') = \rho(x, r) \exp\left(\frac{-j4\pi R_T}{\lambda}\right) \cdot \text{sinc}\left[\frac{\pi}{\Delta r}(r' - r)\right] \text{rect}\left(\frac{x' - x}{X}\right). \quad (4.18)$$

By substituting in (4.18) the relation in (4.17), as follow:

$$h(x', r') = \rho(x, r) \exp\left(\frac{-j4\pi r}{\lambda}\right) \text{sinc}\left[\frac{\pi}{\Delta r}(r' - r)\right] \cdot \exp\left[\frac{-j4\pi}{\lambda} \frac{(x' - x)^2}{2r}\right] \text{rect}\left(\frac{x' - x}{X}\right), \quad (4.19)$$

the previous relation highlights the presence of an equivalent *chirp* signal along the azimuth direction, given by :

$$c_{p2}(x') = \exp\left[\frac{-j4\pi}{\lambda} \frac{(x' - x)^2}{2r}\right] \text{rect}\left(\frac{x' - x}{X}\right), \quad (4.20)$$

whose *chirp rate* is:

$$\alpha'' = \frac{4\pi}{\lambda r}, \quad (4.21)$$

in  $\frac{\text{rad}}{\text{m}^2}$  or equivalently:

$$\alpha'' = \frac{2v_s^2}{\lambda r}, \quad (4.22)$$

in  $\text{Hz}^2$ , whose duration is,

$$\Delta T'' = X. \quad (4.23)$$

The *chirp* signal in (4.20) is generated by the translation movement of the sensor along its trajectory. As seen for the range compression, the azimuth focusing can be achieved through the convolution with the reference function in azimuth given by:

$$a_f(x') = \exp\left(\frac{j4\pi}{\lambda r} \frac{x'^2}{2}\right) \text{rect}\left(\frac{x'}{X}\right), \quad (4.24)$$

resulting in the final focused SAR image:

$$S_f(x', r') = \rho(x, r) \exp\left(\frac{-j4\pi r}{\lambda}\right) \text{sinc}\left[\frac{\pi}{\Delta r}(r' - r)\right] \text{sinc}\left[\frac{\pi}{\Delta x}(x' - x)\right]. \quad (4.25)$$

By recalling (4.14), the sinc extension in the  $x'$  variable defines the azimuth resolution after the *azimuth focusing* operation which is given by:

$$\Delta x = \frac{2\pi}{\left(\frac{4\pi}{\lambda r}\right) X} = \frac{L}{2}. \quad (4.26)$$

The signal  $S_f(x', r')$  represents the focused signal for a point target. The set of processing operations that lead to the focused signal are referred to as *SAR focusing* operation. They are schematically described in Figure 4.4:

1. *Range Focusing*: the *raw signal* is range focused through a matched filter whose impulse response  $l_f(r')$  is given by (4.12);
2. *RCM compensation*: in the range focused signal the RCM effect has to be compensated;
3. *Azimuth Focusing*: the range focused and RCM compensated signal is azimuth focused through a matched filter with impulse response  $a_f(x')$  given by (4.24).

In case of a continuous distribution of scatterers, the general expression of the SAR image within each resolution cell is given by the superposition of all the elementary backscattering contributions of the scene:

$$S_f(x, r) = \int \int \rho(\bar{x}, \bar{r}) \exp\left(\frac{-j4\pi \bar{r}}{\lambda}\right) \text{sinc}\left[\frac{\pi}{\Delta r}(r - \bar{r})\right] \text{sinc}\left[\frac{\pi}{\Delta x}(x - \bar{x})\right]. \quad (4.27)$$

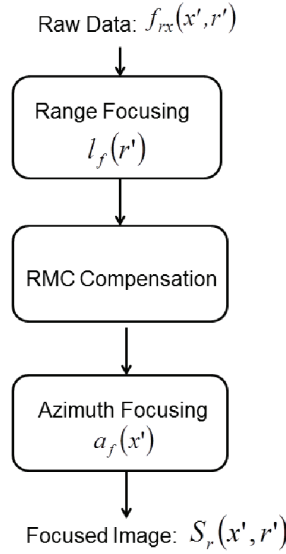


Figure 4.4: Block diagram of SAR focusing operations

### 4.1.2 SAR Image

Differently from optical images, SAR images are not very easy to be interpreted. A focused SAR image can be expressed via the equation (4.27) and managed as a complex-valued matrix. Each resolution cell, given by  $\Delta x \times \Delta r$ , corresponds to a pixel in the SAR image.

However, as suggested by the Nyquist condition, the pixel dimensions will be, generally, numerical lower than the theoretical resolutions and they will account for the range sampling frequency  $f_{samp}$  and the PRF, respectively, that is:

$$\Delta r = \frac{c}{2\Delta f} \geq \frac{c}{2f_{samp}} = \Delta r_{PIXEL}$$

$$\Delta x = \frac{L}{2} = \frac{v_s}{B_x} \geq \frac{v_s}{PRF} = \Delta x_{PIXEL}$$

where  $B_x = 2v_s/L$  is the azimuth bandwidth (often interpreted as Doppler bandwidth), being  $v_s$  the sensor velocity. Finally it should be remarked that each single SAR image can be also effectively analyzed via the inspection of the relevant amplitude and phase component, respectively. The amplitude is related to the backscattering coefficient of the ground, while the phase contains information about the travel distance of the transmitted signal.

Due to the coherent data processing, SAR images show amplitude values characterized by a *salt and pepper* effect and a randomly distributed phase. Inside a

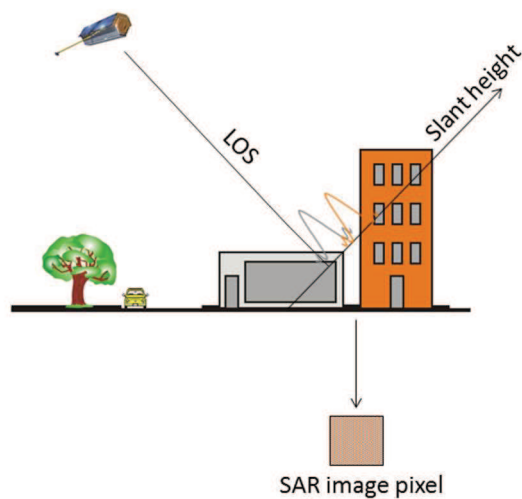


Figure 4.5: Layover effect

resolution cell, many different scatterers are located, providing a backscattered signal which is the coherent sum of all contributes characterized by a random distribution. This coherent interference is the basis of the so-called *speckle* effect, which is present even over homogeneous areas. This speckle effect prevents the use of a single image to measure distance of objects.

Another interesting aspect of SAR images is due to the fact that since in SAR systems time delays are measured, points having the same distance to the antenna are located in the same position in the image. This can become a problem, or a source of misunderstanding of SAR images when areas with strong topography are investigated, as f.i. urban areas. In such cases, different geometrical distortion effects induced by the terrain slope can arise in SAR images. Three main geometrical distortion can be distinguished: foreshortening, shadowing and layover.

The *foreshortening* effect occurs when the radar beam reaches the base of a tall feature tilted towards the radar (e.g. a mountain) before it reaches the top. Because the radar measures distance in slant-range, the slope will appear compressed in the SAR image, providing a tilting of the top of the mountain towards the sensor.

The *shadowing* effect happens when the radar signal is shadowed by the topography. In this case backscattered information is lost and no signal is collected. This causes a dark area in the SAR image that contains no signal, but only systems noise. This effect increases with greater incident angle  $\theta$ .

The *layover* phenomenon typically arises in very steep height areas, as urban

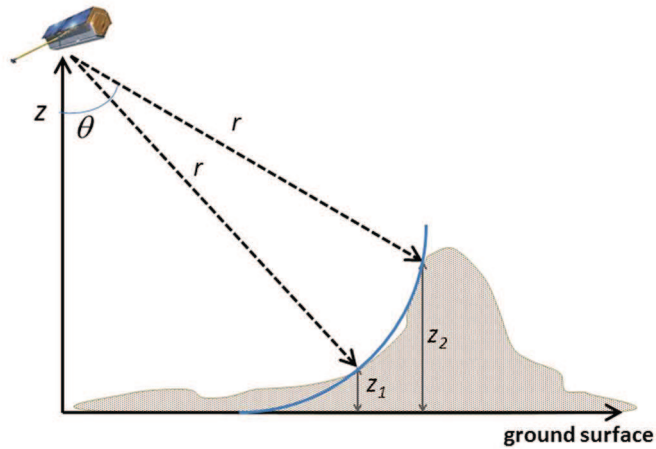


**Figure 4.6:** SAR geometry in the plane orthogonal to the flight direction with a single sensor: schematic picture of the layover

areas. Due to the SAR geometry, different targets positioned along the same slant height edge, i.e. at the same distance from the radar but at different heights, will interfere within the same resolution cell and hence will be mapped within the same SAR image pixel.

In presence of a vertical structure, such as a building, layover is particularly critical. The geometry of a building subject to layover is shown in Figure 4.5: the backscattering return coming from a near ground building (the grey coloured one) interfere within the same resolution cell with the one coming from the vertical wall of the tallest building (the orange coloured one).

## 4.2 SAR Interferometry

As explained in the previous section, SAR imaging allows representing with a certain resolution the observed scene into the *azimuth-range* plane. Obviously, this is not sufficient to unambiguously locate the targets, i.e. to estimate their height with respect to a reference plane. In fact, similarly to a common optical image, a (single) SAR image is a two-dimensional projection of the scene and it is not sufficient to determine the 3D location of the objects. Therefore, with regard to the generic position of the sensor along its flight path, all targets within the range beam located along an equidistance curve will be imaged at the same range position. The effect of the loss of 3D sensitivity is explained in Figure 4.6, which shows the SAR geometry in the plane orthogonal to the azimuth direction. As evident, two different targets on the ground scene at different heights, i.e.  $z_1$  and  $z_2$  and at the same distance  $r$  from the radar, i.e.

located along an equirange curve, are imaged in the same position. Hence any information about height is lost.

In other words, the SAR imaging principle does not allow accessing to the third coordinate  $\theta$  of the imaged target in the cylindrical reference system.

Similarly to the human visual system, this limitation can be circumvented by exploiting, at least, two different SAR images of the same area, acquired from a slightly different geometry flight tracks, as depicted in Figure 4.7.

SAR Interferometry (InSAR) [1, 5] is a technique, exploiting the phase of two complex SAR images, acquired from different orbit positions and/or at different times, to estimate the position on the ground of the illuminated targets. In principle, different antenna distributions define different interferometer configurations. In particular, the SAR Interferometry (InSAR) configurations involve two antennas observing the investigated scene:

- flying on two parallel tracks and looking at ground from slightly different positions (*across-track interferometry*);
- flying on the same flight direction, looking at ground from the same position but with a small temporal delay (*along-track interferometry*).

Across Track Interferometry is used to reconstruct Earth topography, providing high precision DEM of Earth surface. The two SAR images can be either collected by means of a *single-pass* imaging system (characterized by the presence of two distinct antennas: the former operating in a receive/transmit mode and the latter in the receive mode, only), or with *repeat-passes* of a single imaging sensor over the same area. A single-pass configuration example are the one of Shuttle Radar Topography Mission (SRTM) in 2001, which allows topography mapping of a whole Earth with a spatial resolution of about 30m, and the Tandem-X (TDX) mission, which has been acquiring data since 2010 to generate global DEM at 12m spatial resolution with absolute height accuracy of 10m. In both cases, only one antenna transmits while the other operates in receiving mode only.

In the thesis, I will focus, in particular, on the across-track repeat-pass interferometry, suitable for space-borne applications, with emphasis on the new generation X-band sensors.

The geometry of an across track interferometric system in the plane orthogonal to the azimuth direction is shown in Figure 4.7. In this plane the two SAR systems are separated by a *spatial baseline*  $b$  (which represents the distance between the flight tracks), which can be decomposed into either parallel/perpendicular ( $b_{//}, b_{\perp}$ ) components, where in particular  $b_{\perp}$  is the component of the baseline orthogonal to the look direction. The sensors can be distinguished as *master antenna* and the *slave antenna*, whose looking angle are respectively  $\theta_1$  and  $\theta_2$ .

In the two SAR images, the target is located at two different range distances, i.e.  $r$  for the first, i.e. master image, and  $r + \delta r$  for the second one, i.e. slave

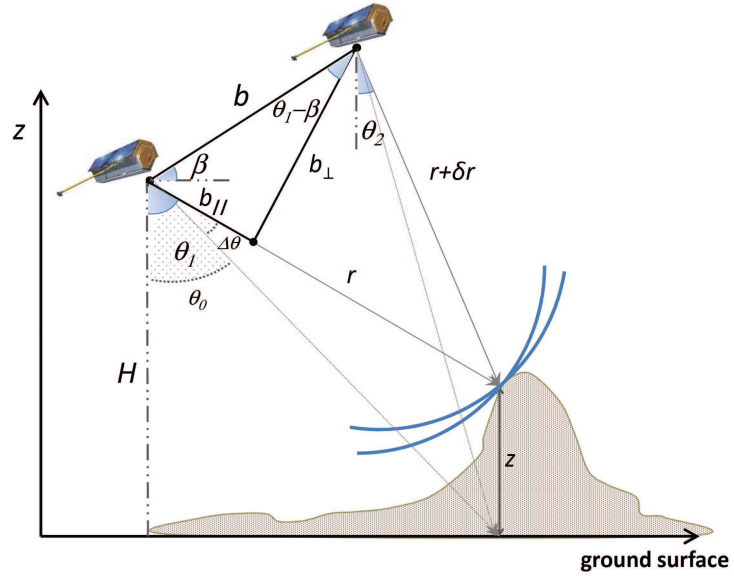


Figure 4.7: Interferometric acquisition geometry

image. Differently from Figure 4.6, there is only one target located on the two different equirange curves corresponding to the master and slave images. With reference to the SAR focused image in (4.27), let assume the sinc( $\cdot$ ) functions could be represented as Dirac ones; the master and slave images, called  $S_m(x, r)$ , and  $S_s(x, r)$ , respectively, for a point target located at  $(x, r)$  will be:

$$\begin{aligned}
 S_m(x, r) &= \rho(x, r) \exp \left[ -j \frac{4\pi}{\lambda} r \right] \\
 S_s(x, r) &= \rho(x, r) \exp \left[ -j \frac{4\pi}{\lambda} (r + \delta r) \right].
 \end{aligned}
 \tag{4.28}$$

The previous couple of images has been obtained after a pre-processing step called *registration*, by means of which the same target on the scene is placed in the same pixel of the two different images, thus allowing working with the same reference geometry. In fact, because in principle the images are acquired from different positions of the sensors, the same target is seen at different ranges ( $r$  for the master image and  $r + \delta r$  for the slave). The registration step aims to resample the second image in order that a physical ground scatterer appears in the same pixel (or almost the same pixel to a subpixel accuracy) in the two images, by preserving at the same time the path difference phase term [1, 2, 6]. By taking into account (4.28), the *interferogram* is generated from the product

of the master image by the complex conjugate of the slave one:

$$\begin{aligned}
 S_{int}(x, r) &= S_m(x, r) \cdot S_s(x, r)^* = \\
 &= |\rho(x, r)|^2 \exp [j(\angle S_m(x, r) - \angle S_s(x, r))] = \\
 &= |\rho(x, r)|^2 \exp [j\varphi] = |\rho(x, r)|^2 \exp \left[ j \frac{4\pi}{\lambda} \delta r \right]
 \end{aligned} \tag{4.29}$$

where the  $(\cdot)^*$  operator denotes the complex conjugate operation, while  $\angle(\cdot)$  refers to the full phase extraction operator. The phase term  $\varphi$ :

$$\varphi = \frac{4\pi}{\lambda} \delta r \tag{4.30}$$

is a very sensitive measure for the range difference and can be directly related to the height of the scene, as will be demonstrated in Section 4.2.1.

However, since a phase term is extracted from a complex data, see (4.29), the interferometric phase difference is restricted (*wrapped*) in the  $(-\pi; +\pi)$  interval, whereas in practical case the absolute phase (*unwrapped*) largely exceeds this interval. In other words, while the topography is linearly related to the absolute phase, the measured one is related to the absolute by a non-linear function that forces the phase to belong to the  $(-\pi; +\pi)$  interval. The Phase Unwrapping (PhU) techniques aim to invert this non-linear mapping in order to retrieve an estimation of the unrestricted phase [7]. This operation, due to the non-linear nature, is one of the most challenging steps in the interferometric SAR processing.

In Figure 4.8 the wrapped interferogram corresponding to the Stromboli volcano derived from data acquired by the DLR-ESAR airborne interferometric system is shown. It has been obtained by an overlay of the interferometric phase signal on a 3D model of topography. Each colour variation from dark to bright is referred to as *fringe*; fringes are interpretable as equi-level curves (locally over wide scenes). They correspond to the  $2\pi$ -phase jumps, hence to a height variation of about 50m.

### 4.2.1 InSAR height sensitivity

By referring to Figure 4.7, let demonstrate how the interferometric phase  $\varphi$  in (4.30) is related to the height.

The incidence angle of the master antenna is  $\theta_1 = \theta_0 + \Delta\theta$ ; hence the variation of topography from  $z = 0$  to  $z$  determines a variation of the look angle equal to  $\Delta\theta$ .

By considering the scatterer at height  $z$ , the difference between the two distances sensor-scatterer  $\delta r_z$  can be written as the projection of the baseline  $b$  on the master antenna LOS:

$$\delta r_z = b \sin(\theta_1 - \beta) = b \sin(\theta_0 + \Delta\theta - \beta), \tag{4.31}$$



**Figure 4.8:** ESAR interferogram relevant to the Stromboli volcano superimposed to the 3D model of topography

where  $\beta$  is the angle between the baseline  $b$  and the horizontal plane and also  $b_{//} = b \sin(\theta_1 - \beta)$  is the parallel baseline.

On the other hand, by applying the parallel ray approximation [8], for the scatterer at height  $z = 0$ , the difference between the two distances sensor-scatterer  $\delta r_0$  is:

$$\delta r_0 = b \sin(\theta_0 - \beta). \quad (4.32)$$

Let see now how the change in height is reflected in the difference of the interferometric phases  $\Delta\varphi$ :

$$\begin{aligned} \Delta\varphi &= \frac{4\pi}{\lambda}(\delta r_0 - \delta r_z) = \frac{4\pi b}{\lambda}[\sin(\theta_0 - \beta) - \sin(\theta_0 + \Delta\theta - \beta)] = \\ &= \frac{4\pi b}{\lambda}[\cos(\theta_0 - \beta)\Delta\theta] \end{aligned} \quad (4.33)$$

where, since  $\Delta\theta$  is very small (hence  $\theta_1 \approx \theta_0$ ), a small angle approximation has been used. The small variation in the looking angle  $\Delta\theta$  is related to  $z$  according to the following relation:

$$\begin{aligned} z &= H - r \cos(\theta_0 + \Delta\theta) = r \cos \theta_0 - r \cos(\theta_0 + \Delta\theta) = \\ &= r(\cos \theta_0 - \cos \theta_0 \cos \Delta\theta + \sin \theta_0 \sin \Delta\theta) = r \sin \theta_0 \Delta\theta \end{aligned} \quad (4.34)$$

where, again, a small angle approximation has been used.

Finally, by substituting (4.34) in (4.35) the relation between the measured

phase and the height can be derived as follow:

$$\Delta\varphi = \frac{4\pi b}{\lambda \sin \theta_0} \cos(\theta_0 - \beta) z = \frac{4\pi b_{\perp}}{\lambda \sin \theta_0} z \quad (4.35)$$

being  $b_{\perp} = b \cos(\theta_0 - \beta)$  the orthogonal baseline.

Hence it is evident that by exploiting SAR images InSAR technique allows reconstructing Digital Elevation Model (DEM) of the observed area.

### 4.2.2 Decorrelation effects

To introduce a measure about the phase quality, it is useful to refer to the cross-correlation factor, defined as follows [5]:

$$\chi = \frac{E[S_m \cdot S_s^*]}{\sqrt{E[|S_m|^2] \cdot E[|S_s|^2]}} = |\chi| \exp(j\varphi), \quad (4.36)$$

where  $E[\cdot]$  stands for the expectation operator. Moreover, practically these operations are replaced by spatial averages, usually referred to as multi-look operation, and the choice of the optimal averaged boxes is set according to the desired multilook degree. The average procedure leads to an improvement of the interferometric phase standard deviation.

It may be observed that the cross-correlation factor can be decomposed in an amplitude and a corresponding phase term, respectively. The amplitude, known as *coherence*, ranges between  $[0, 1]$  and accounts for the similarity of the two images, while the phase corresponds to the multi-looked interferometric phase, directly. A zero coherence stands for a completely uncorrelated scene, whereas a coherence close to 1 corresponds to a noise-free interferogram.

At this stage, the origin for the coherence decrease can be addressed.

The interferometric processing relies on the assumption that the target backscattering coefficient  $\rho$  in (4.29) is the same in the master and slave images. However this assumption is never met in the reality due to several reasons. Changes of the backscattering response between the two passages of the sensor over the illuminated area represent a noise source in the interferogram, which are usually referred to as *temporal decorrelation* effect. It is usually associated with weather changes, that modify the electromagnetic response of the ground, as f.i. in rural or vegetated areas: foliage cover, leaves orientation, seasonal changes, etc. typically introduce a strong decorrelation that “blinds” the interferometric radar system. On the other hand, urban areas with their stable structures, such as buildings and roads, exhibit a long term high correlation degree preserve coherence along time even with very large temporal baselines; also human activities can cause a change of the backscattering response.

Another error source is due to errors in the image registration process (*registration decorrelation*): in this case, the scatterers falling in the same pixel of the master and slave images belongs to different ground locations.

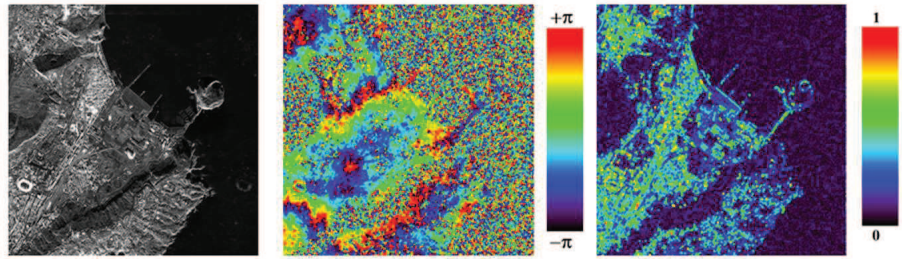


**Figure 4.9:** (left side) A temporal multilook SAR image of the Naples (Italy) bay area (average of 30 CSK images); (center) An interferogram and (right side) the corresponding coherence map

Furthermore the different imaging geometries of the master and slave antennas cause the fact that same ground resolution cell is imaged from two slightly different looking directions. This effect is usually referred to as *geometrical or spatial decorrelation*; it increases with increasing perpendicular baseline. Hence, even if spatial separation between master and slave antennas is required for topography estimation, targets exhibit a slightly different response when imaged from different view angles, thus posing a limitation to the spatial baseline. Coherence maps are useful to get an estimate of this type of decorrelation. In left Figure 4.9 it is shown a temporal multilook SAR image of the Naples (Italy) bay area (average of 30 CSK images), in which it is possible to recognize urban areas (white pixels) and rural areas (dark pixel), as well as the sea on the right.

In the central Figure 4.9 the interferogram relevant to the city of Naples, Italy, is shown. This interferogram has been generated by using a pair of descending COSMO-SkyMed acquisitions with temporal and spatial separations of 105 days and 89m, respectively. It has been obtained by spatially filtering with the standard boxcar multilooking, i.e. with a uniform averaging in a spatial window with dimensions equal to  $16 \times 16$  pixels.

In right Figure 4.9 the associated coherence map is shown: the urban area shows higher coherence (green-orange pixels) with respect to the countryside, where low coherence values are measured (blue pixels). It is worth noting that the use of a boxcar filter implies the averaging of pixels that are associated with different ground structures (forests, fields, street, etc.) and therefore with different behaviour in terms of decorrelation characteristics. Adaptive spatial filtering technique, that spatially average a fixed number of pixels only if they share similar scattering properties, is also possible [9].

Figure 4.10 displays the adaptive spatial filtered interferogram relative to the same image couple of Figure 4.9. The multilooking factor is retained in  $16 = 256$ . The adaptive spatial filtering displays a better quality of the interferometric fringes with respect to the boxcar filtering. Respect to the classical boxcar

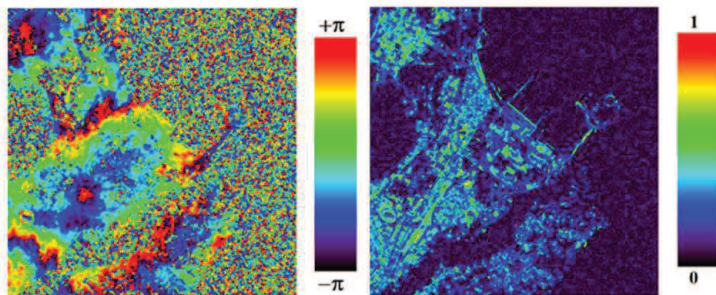


**Figure 4.10:** (left side) Adaptive spatial filtered interferogram and (right side) the corresponding coherence map

averaging (central Figure 4.9), the adaptive filtering allows preserving structures details: In particular, by comparing the interferogram in Figure 4.9 and Figure 4.10, the shape of the structures are well defined and roads, buildings and particularly wharfs are still well recognizable. The corresponding coherence map (right Figure 4.10) also demonstrates that, by selecting only neighbours with similar scattering properties, the adaptive filtering retains high coherence values over the structures and avoid the mixing of low and high coherence pixel classes.

### 4.3 Differential SAR Interferometry

Interferometry can be also effectively used to investigate Earth's surface changes occurring between the two passes of the radar sensor [10]. The interferometric technique exploiting phase difference between SAR images acquired from exactly the same position but at different time instants is known as DInSAR.

In fact, the interferometric phase is related to the difference of the radiation path between the master and slave images (see (4.30)). By assuming the master and the slave images acquired in different time instants but from exactly the same position of the SAR sensor, if a ground displacement has occurred between the two passes of the sensor (f.i. due to an earthquake, a landslide, a subsidence phenomenon,... ) the interferometric phase will be given by:

$$\varphi = \frac{4\pi}{\lambda}(r_2 - r_1) \approx \frac{4\pi}{\lambda}d_{LOS}, \quad (4.37)$$

the equation (4.37) allows retrieving a measurement of the LOS displacement, i.e. the displacement component along the radar LOS, of the order of fractions of wavelength. Indeed, a differential phase change of  $2\pi$  is associated with a

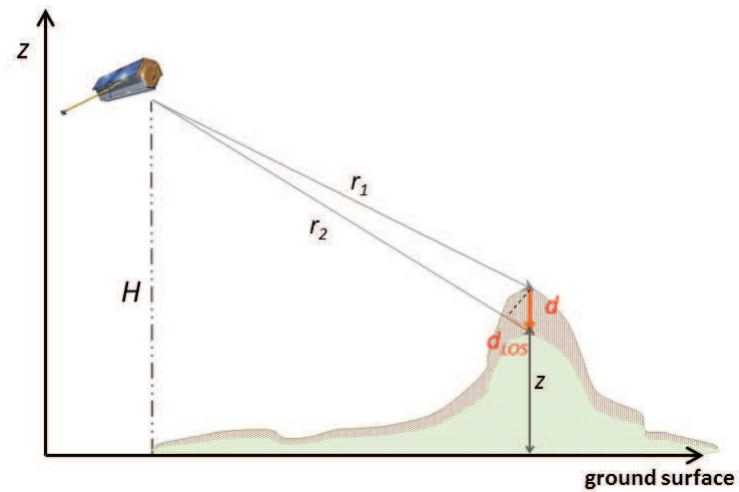


Figure 4.11: DInSAR geometry (zero baseline configuration)

LOS displacement of  $\lambda/2$  that, for the new generation of high-resolution X-Band sensors, reaches about 1.6 cm.

In Figure 4.11 is shown the simplified DInSAR geometry where the master and slave orbital positions are considered to be identical, thus allowing immediately individuating the deformation component. Here the overall scene undergoes a deformation  $d$  (its magnitude has been intentionally exaggerated to better show the geometry of the system), whose component measured by the radar is  $d_{LOS}$ . However, the Phase Unwrapping step is still needed to recover the real, unrestricted, displacement signal.

DInSAR represents a very powerful tool for monitoring displacements caused by, f.i., seismic phenomena. It provides a large scale accurate deformation measurement, which is very useful for understanding the fault movements. Therefore it is a very efficient tool for civil protection and risk management [10–12]. In Chapter 5 it will be shown some DInSAR results concerning the 6.3 Mw earthquake that on 6 April, 2009, stroke the area of L’Aquila, Italy [13].

### 4.3.1 Main limitation of DInSAR technique

The differential interferogram, containing the deformation component, may be affected by residual phase terms, due to different error sources, that may corrupt the deformation measurement accuracy.

Many sources of uncertainty affect the displacement information estimation through a single interferometric couple.

First of all the zero perpendicular baseline assumption is very simplistic and is

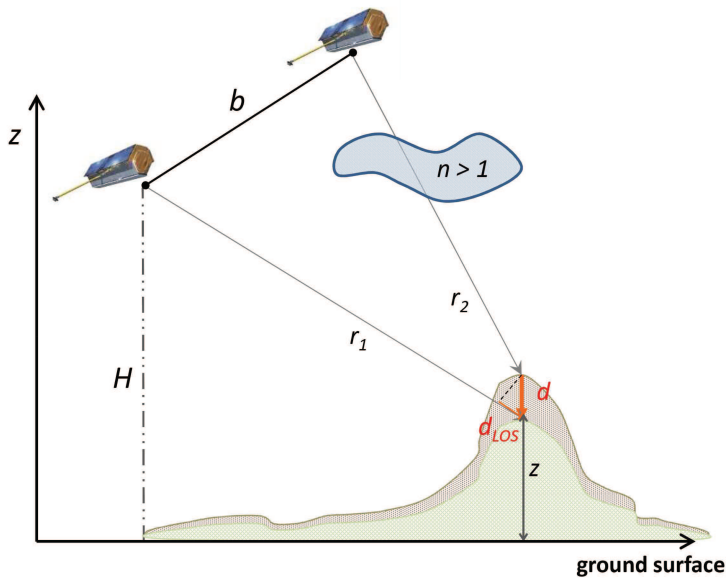


**Figure 4.12:** DInSAR geometry (no zero baseline configuration), where it has been introduced also the atmospheric effect due to possible inhomogeneities of the atmospheric refraction index, which is responsible of an incorrect estimation of the deformation signal.

highly improbable to be verified; it implies that in each passes over the same area the satellites have to fly exactly over the same orbit. Practically, a small perpendicular baseline between the orbits exists. It causes the occurrence of additional topographic fringes in the differential interferogram. However the topographic phase term is not of interest with regard to the surface displacement mapping. For this reason, in order to limit its influence, the discrimination between the topographic and the displacement phase terms, respectively, must be carried out.

This topography component is typically compensated by using an external DEM (two-pass differential interferometry) that represents a digitalized version of the topography profile of the scene. To do this, the DEM has to be transformed in the azimuth-range geometry, scaled by the perpendicular baseline of the interferogram; finally the resulting topographic pattern has to be converted from length to phase units. However, the DEM is known with a certain uncertainty and a certain spatial resolution (spanning from tens to one hundred of meters). Hence the DInSAR interferogram will contain a spurious phase term associated with a residual (with respect to the external DEM) topography. The magnitude of this error source depends on the amplitude of the spatial baseline between passes; it becomes significant when the baseline ex-

ceeds the order of some tens of meters, thus limiting the usage of the available SAR acquisitions. This is a problem, especially in cases of crisis events.

Furthermore orbital parameters estimation can be inaccurate.

Moreover, the presence of atmosphere represents a further error source in DInSAR products. Even if one of the most important features of microwave remote sensing is to operate independently of weather conditions, it may happen that between the two passes of the radar sensor the weather conditions may sensibly change, causing a change of the atmospheric refractive index, and hence of the propagation velocity of the radar pulses (Atmospheric Propagation Delay (APD)). This turns into an additional path delay that afflicts the interferometric products; it is not related to any deformation, but can be misinterpreted as deformation.

In Chapter 5, it will be better analyzed the atmospheric error component.

Figure 4.12 explains the no-ideal DInSAR acquisition geometry: it can be noted the presence of a spatial baseline between the two SAR acquisitions and also the different behaviour of the atmosphere.

Finally, also the phase unwrapping in case of large topography discontinuities or deformation patterns may result in wrong solutions.

All these effects imply the differential interferometric phase expression to be:

$$\varphi_{\text{DInSAR}} = \varphi_{\text{top}} + \varphi_{\text{orbit}} + \varphi_{\text{def}} + \varphi_{\text{atm}} + \varphi_n, \quad (4.38)$$

where:

- $\varphi_{\text{def}}$  is the phase term associated with deformation (that DInSAR aims to measure), corresponding to the displacement occurred between the two flights;
- $\varphi_{\text{top}}$  is the spurious phase term due to residual topography (after the subtraction of an external DEM), due to the error in the knowledge of the scene topography and/or to an incorrect resampling of the used DEM in the SAR coordinates;
- $\varphi_{\text{orbit}}$  is the spurious phase term due to an inaccurate knowledge of the orbital positions of the sensors on the analyzed area;;
- $\varphi_{\text{atm}}$  is the spurious phase term due to the APD, i.e. Atmospheric Phase Screen (APS);
- $\varphi_n$  is the additive noise contribution.

Due to the presence of these limitation factors within a single pair of SAR images interferogram, it is not possible to separate the deformation term from the other, so, it has been introduced more sophisticated processing techniques by exploiting the combination of multiple SAR images.

## 4.4 Multipass SAR Interferometry

DInSAR limitations have encouraged the development of more sophisticated techniques exploiting a large collection of SAR images over the same area [14,15]. The so-called Multipass SAR Interferometry exploits SAR images dataset, i.e. a collection of SAR images acquired in different time instants (Multitemporal) and with different baselines between sensor passes (Multibaseline). They allow retrieving long term measurements, and hence estimating the full temporal evolution (time series) of possible ground deformations.

These approaches rely on the assumption that the imaged target remains stable during the entire time interval spanned by the SAR images dataset. They require that complex processing chains, with a given computational cost, are considered.

From the analytical point of view, given a set of  $N$  SAR images relevant to the same illuminated area, after the selection of the optimal interferometric data pair distribution and the co-registration of each SAR image with respect to a properly identified “*reference master image*” (with respect to which the baseline values are evaluated),  $M$  interferograms are computed. For the generic stable points of coordinates  $(x, r)$  the vector  $\varphi$  collecting the  $M$  interferometric phases, after the subtraction of the external DEM, is usually modelled as:

$$\varphi = \frac{4\pi}{\lambda} (\boldsymbol{\beta} \cdot \mathbf{z} + \mathbf{d}_L + \mathbf{d}_{NL}) + \varphi_{\text{orbit}} + \varphi_{\text{atm}} + \varphi_n, \quad (4.39)$$

where:

- $\boldsymbol{\beta} = \frac{\mathbf{b}_\perp}{r \sin \theta}$  collects the relative orthogonal baseline;
- $\mathbf{z}$  is the residual topography (after the subtraction of an external DEM);
- $\mathbf{d}_L = v_d \cdot \Delta \mathbf{t}$  represents the linear component of deformation, with  $v_d$  the deformation mean velocity and  $\Delta \mathbf{t}$  the temporal epoch vector corresponding to the different passes;
- $\mathbf{d}_{NL}$  accounts for possible non-linear displacement;
- $\varphi_{\text{orbit}}$  is associated with possible orbital track inaccuracies;
- $\varphi_{\text{atm}}$  is the term accounting for the propagation delay variation due to the presence of the atmosphere;
- $\varphi_n$  is the noise contribution that accounts for several decorrelation terms (thermal noise, scattering variations, clutter, temporal scattering changes, etc).

Multipass InSAR algorithms are based on a joint analysis of data acquired in multiple repeated passes (multipass) over the same area with a variety of baselines, to jointly estimate ground deformation and residual topography (and

therefore target localization). In order to introduce the key ideas of the available algorithms, it can be convenient to look at the SAR data acquisition distribution in the temporal/perpendicular baseline plane. Basically, the set of possible algorithms is based on the proper selection of the interferometric data pair distribution. It is known that the larger are the perpendicular and/or temporal baselines value, the more significant will be the decorrelation phenomena. Hence, depending on the choice of the optimal interferometric distribution, the different algorithms will be able to extract different and/or additional information.

The Persistent Scatterer Interferometry (PSI) algorithm [15,16] generates a set of interferograms between each single SAR image and the “*reference master image*”. Nevertheless, it could happen that some of the considered interferograms may have a perpendicular baseline value greater than the critical one and hence can be strongly affected by the decorrelation effects. The key idea of PSI algorithm is to identify and analyze only pixels with a stable phase behavior in time, i.e. targets whose electromagnetic response remains correlated over the time (i.e. in all SAR acquisitions), or better it “*persists*” throughout the observation period and with the angular variation of SAR acquisitions. This assumption is valid only for a limited number of objects (i.e. the Persistent Scatterer (PS)) on which it is possible to apply specific algorithms. They usually correspond to point-like targets, such as buildings, roads or man-made objects.

PS candidates are selected from the study of the amplitude of SAR interferograms, which is almost insensitive to most of the phenomena that contribute to the interferometric phase such as atmospheric effects, DEM errors, and terrain deformation. This technique requires a minimum of 30 images and a proper radiometric calibration for a reliable pixel selection, so that the maximum resolution of the SAR images is preserved.

An iterative approach allows estimating for each PS the residual topography and the linear component of the deformation velocity, together with constant and linear components of the atmospheric artifact. Finally, for each image, the non linear component of the movement and the APS is estimated with a combined spatial-temporal filtering; it is then subtracted from the original interferograms.

PSI demonstrated for the first time that the atmospheric contribution could be tackled by analysing long-term radar sequences, providing very precise deformation measurements. It assumes a dominant scattering mechanism per pixel, it is generally applied to a full resolution scale, i.e. to single look data. However computational load problems when the processing is performed over large areas limit the width of coverage.

Another possible solution is represented by the choice of a set of Small Baseline interferograms only: the Small Baseline Subset (SBAS) [14]. Similarly to the classical single pair DInSAR analysis, Small Baseline Subset (SBAS)

carries out an analysis based on interferogram stacking and process multilook data, i.e. data that have been spatially averaged and are thus characterized by a lower resolution, to easily achieve large coverage. Differently from the PSI technique, the available acquisitions are generally combined in order to achieve a large number of interferograms with small temporal and spatial baselines thus retaining high spatial coherence and limiting the topographic errors. Deformation mean velocity and residual topography products are generated through a joint estimation involving the model in (4.39). A final Single Value Decomposition (SVD)-based inversion allows retrieving an estimation of the time series of displacement. For what concern the APS, it is separated at the very last stage of the processing by applying a cascade of a low-pass filtering step, performed in the spatial domain, and of a high-pass filtering with respect to the time variable.

A third approach, called Enhanced Spatial Differences (Enhanced Spatial Differences (ESD)), exploits the advantages of both the PSI and SBAS [17]. Particularly, as for SBAS technique, multilook data are processed to achieve large coverage. ESD exploits spatial difference, i.e. phase gradients, between adjacent pixels to tackle APS efficiently since spatial difference allows mitigating the effect of atmospheric contribution, almost similar on adjacent pixels. On the other hand, the joint multipass analysis allows only retrieving the gradients of residual topography and deformation mean velocity. A following spatial integration step is required to obtain the point-wise estimation. Subsequently, to reconstruct the whole deformation sequence, spatial differences are enhanced and integrated layer-per-layer on the residual multipass data stack, which encompasses non-linear deformations, via a sparse unwrapping. A final deformation mean velocity and residual topography estimation is performed on the unwrapped stack to feed-back the results on a pixel basis and eliminate possible error propagation in the spatial difference integration operation.



# References

- [1] Franceschetti, G. and Lanari, R., *Synthetic Aperture Radar Processing*. Boca Raton, FL; CRC Press, 1999.
- [2] Curlander, J.C. and McDonough, R. N., *Synthetic Aperture Radar: System and Signal Processing*. Wiley, New York, 1991.
- [3] R. K. Raney, *Radar Fundamentals: Technical Perspective, Chapter 2*. Wiley Interscience: New York., 1998.
- [4] R. Lanari and G. Fornaro, "A short discussion on the exact compensation of the sar range-dependent range cell migration effect," *IEEE Transactions on Geoscience and Remote Sensing*, vol. 35, 1997.
- [5] R. Bamler and P. Hartl, "Synthetic Aperture Radar Interferometry," *Inverse Problems*, vol. 14, no. 4, pp. R1–R54, Aug. 1998.
- [6] E. Sansosti, P. Berardino, M. Manunta, F. Serafino, and G. Fornaro, "Geometrical sar image registration," *IEEE Transactions on Geoscience and Remote Sensing*, vol. 44, no. 10, pp. 2861–2870, Oct 2006.
- [7] D. C. Ghiglia and M. D. Pritt, "Two-Dimensional Phase Unwrapping: Theory, Algorithms and Software," *John Wiley and Sons New York*, 1998.
- [8] H. Zebker and R. Goldstein, "Topographic mapping from interferometric Synthetic Aperture Radar observations," *Journal of Geophysical Research*, vol. 91, no. B5, pp. 4993–4999, 1986.
- [9] G. Fornaro, D. Reale, and S. Verde, "Adaptive spatial multilooking and temporal multilinking in SBAS Interferometry," in *2012 IEEE International Geoscience and Remote Sensing Symposium*, July 2012, pp. 1892–1895.
- [10] D. Massonnet, M. Rossi, C. Carmona, F. Adragna, K. Peltzer, G. and Feigl, and T. Rabaute, "The displacement field of the Landers earthquake mapped by radar interferometry," *Nature*, vol. 364, pp. 138–142, 1993.

- 
- [11] A. K. Gabriel, R. M. Goldstein, and H. A. Zebker, "Mapping small elevation changes over large areas: differential radar interferometry," *Journal of Geophysical Research: Solid Earth (1978–2012)*, vol. 94, no. B7, pp. 9183–9191, 1989.
  - [12] D. Massonnet, P. Briole, and A. Arnaud, "Deflation of mount etna monitored by spaceborne radar interferometry," *Nature*, vol. 375, no. 6532, pp. 567–570, 1995.
  - [13] G. Fornaro, N. D'Agostino, R. Giuliani, C. Noviello, D. Reale, and S. Verde, "Assimilation of gps-derived atmospheric propagation delay in dinsar data processing," *Selected Topics in Applied Earth Observations and Remote Sensing, IEEE Journal of*, vol. 8, no. 2, pp. 784–799, Feb 2015.
  - [14] P. Berardino, G. Fornaro, R. Lanari, and E. Sansosti, "A New Algorithm for Surface Deformation Monitoring Based on Small Baseline Differential SAR Interferograms," *IEEE Trans. Geosci. Remote Sens.*, vol. 40, no. 11, pp. 2375–2383, Nov. 2002.
  - [15] A. Ferretti, C. Prati, and F. Rocca, "Permanent Scatterers in SAR Interferometry," *IEEE Trans. Geosci. Remote Sens.*, vol. 39, no. 1, pp. 8–20, Jan. 2001.
  - [16] ———, "Nonlinear Subsidence Rate Estimation Using Permanent Scatterers in Differential SAR Interferometry," *IEEE Trans. Geosci. Remote Sens.*, vol. 38, no. 5, pp. 2202–2212, Sep. 2000.
  - [17] G. Fornaro, A. Paucullo, and F. Serafino, "Deformation monitoring over large areas with multipass differential sar interferometry: A new approach based on the use of spatial differences," *International Journal of Remote Sensing*, vol. 30, no. 6, pp. 1455–1478, 2009.

## Chapter 5

# Integration of GPS-Derived Atmospheric Propagation Delay in DInSAR Data Processing

*Microwave radiation is almost insensitive in terms of power attenuation to the presence of atmosphere; the atmosphere is however an error source in repeat pass interferometry due to propagation delay variations. This effect represents a main limitation in the detection and monitoring of weak deformation patterns in DInSAR, especially in emergency conditions. Due to the wavelength reduction current, X-Band sensors are even more sensitive to such error sources: procedures adopted in classical advanced DInSAR for atmospheric filtering may fail in the presence of higher revisiting rates. In this chapter, it is shown such an effect on data acquired by the COSMO-SkyMed constellation. The dataset has been acquired with very high revisiting rates. This feature allows clearly showing the inability of standard filtering adopted in common processing chains in handling seasonal atmospheric delay variations over temporal intervals spanning periods shorter than one year. In this chapter it will be discussed a procedure for the mitigation of APD that is based on the integration of data of GPS systems which carry out measurements with large observation angles diversity practically in continuous time. The proposed algorithm allows a robust assimilation of the GPS atmospheric delay measurements in the multi-pass DInSAR processing and founds on a linear approximation with the height of the atmospheric delay corresponding to a stratified atmosphere. Achieved results show a significant mitigation of the seasonal atmospheric variations.*

## 5.1 Atmospheric Propagation Delay Characterization

It is well known that the atmosphere affects microwave propagation in terms of signal delay: firstly, it reduces the wave propagation velocity with respect to the vacuum; secondly, it introduces a bending of the wave path [1]. The second effect is generally much smaller than the first: it is neglected for propagation directions with elevations greater than  $15^\circ$ . This condition is verified for all SAR sensors and therefore the bending effect is neglected in the present study. The first effect is associated with the variation of the refractivity index  $n$ .

For standard radar frequencies the atmospheric (excess with respect to the vacuum) refractivity index in parts per million,  $N = 10^6(n - 1)$ , is composed of three different contributions,  $N_{hyd}$ ,  $N_{wet}$  and  $N_{iono}$ , that are commonly referred to as hydrostatic, wet and ionospheric components, respectively. The ionosphere, which is a region of charged particles with a large number of free electrons, introduces a propagation delay that can be determined and removed by using a linear combination of the GPS double frequencies based on the dispersive nature of the medium [2]. In fact the ionosphere is a dispersive medium in radioband, meaning that the propagation delay is dependent upon the signal frequency. It shows typically weak spatial variations which are more significant with L-Band SAR systems [3]: for C and X-Band systems, ionosphere introduces mainly planar phase components in the interferograms and hence plays the same role as orbital inaccuracies that are compensated at the data processing stage. Accordingly, in the following, this component is neglected, and, so, the neutral atmospheric component can be expressed as:

$$N_{hyd} = k_1 \frac{P}{T} \quad (5.1)$$

$$N_{wet} = k_2 \frac{e}{T} + k_3 \frac{e}{T^2} + k_4 W_{cloud} \quad (5.2)$$

where  $P$  is the total pressure [mbar],  $T$  is the temperature [K],  $e$  is the water vapour partial pressure [mbar], and  $W_{cloud}$  is the liquid (cloud) water content [ $\text{gm}^{-3}$ ]; the coefficients  $k_1$ ,  $k_2$ ,  $k_3$ , and  $k_4$  are derived from [4].

The (one way) total Zenith Delay (ZD) can be expressed as [1, 4]:

$$ZD = 10^{-6} \int_z^h N(s) ds, \quad (5.3)$$

where:

$$N = N_{hyd} + N_{wet}, \quad (5.4)$$

and  $h$  is the height of the atmospheric boundary layer and  $z$  is the height of the point under investigation (i.e., the height of the station for GPS or the height of the image pixel for SAR) and the integration is carried out along the vertical

direction to the point.

Accordingly the total zenith delay can be expressed as:

$$ZD = ZHD + ZWD \tag{5.5}$$

being *ZHD*, the Zenith Hydrostatic Delay (ZHD) and *ZWD*, the Zenith Wet Delay (ZWD).

From above analysis, it is evident that the estimation of the ZD in (5.3) requires the evaluation of two contributions: a larger part depending on the 3-D distribution of the total pressure and a smaller portion which is a function of the 3-D distribution of the water vapor content (wet component) [5, 6]. The hydrostatic delay is due to the dry gases in the troposphere and the nondipole component of water vapour refractivity and can be modeled accurately using surface pressure measurements [7]. On the other hand, the wet delay is associated with the dipole component of the water vapour, heavily present in the troposphere, and it exists up to 10 km from the Earth surface. Water vapour is highly variable in space and time, such that the wet delay cannot be modeled using surface measurements very accurately [8]; however, the wet part of the delay component can only be estimated with an accuracy of 10% ÷ 20%.

It is by far (one order of magnitude) lower than the hydrostatic contribution but much more spatially variable.

### 5.1.1 Hydrostatic Component Models

The hydrostatic component generates errors of order of a few meters: it can reach absolute values as large as 2.3 m. For this reason, several authors provided semiempirical models to achieve an estimation of the hydrostatic contribution starting from surface pressure measurements, such as the Saastamoinen model [6], the Hopfield model [9], and the Davis model [5], which modifies the Saastamoinen model giving the zenith hydrostatic path with an accuracy of better than 1 mm under conditions of hydrostatic equilibrium. Saastamoinen [6] in 1972 introduced the separation between the hydrostatic and wet components, modeled both components and showed that the delay in the zenith direction due to atmospheric constituents in hydrostatic equilibrium is accurately determined by measuring the surface pressure and making corrections for the latitude and height above the sea level of the site from which the observation is being made. In the absence of turbulences, the hydrostatic component can be determined with an accuracy of better than 1 mm under hydrostatic equilibrium [7]. The Saastamoinen model for the estimation of the ZHD component, in meters, is [6], [10]:

$$ZHD = \frac{2.277 \times 10^{-3} \pm 2.4 \times 10^{-6}}{f(\phi, z)} P_s(z) \tag{5.6}$$

where  $P_s(z)$  is the total pressure [mbar] at the Earth's surface,  $z$  is the height above the geoid [km] of the GPS receiving station, and  $f(\phi, z)$  accounts for the

variation in gravitational acceleration and is equal to:

$$f(\phi, z) = 1 - 2.66 \times 10^{-3} \cos 2\phi - 0.28 \times 10^{-6} z \quad (5.7)$$

where  $\phi$  is the latitude. It is therefore evident that ZHD can be described in terms of a single parameter, i.e., the ground total pressure  $P_s$  which must be known to provide the modeled ZHD value. From 5.6 and 5.8, it is noted that ZHD is a function of the height through the function  $f(\phi, z)$  and the total pressure  $P = P_s(z)$ . The total pressure  $P_s(z)$  is maximum at sea level and decreases with higher altitude; this is because the atmosphere is very nearly in hydrostatic equilibrium, so that the pressure is equal to the weight of air above a given point. A reasonable approximation of the change of the pressure with height is given by the following relation:

$$P_s(z) = P_0 e^{-z/H} \quad (5.8)$$

where  $H$  is constant, typically fixed to 8 km,  $P_0$  is the pressure measured at a reference point, which is usually assumed to be the sea level, and  $z$  is the height variable. Furthermore, the pressure exhibits changes over the day and, more important, seasonal [11] so that  $P_0$  must be intrinsically considered time-dependent.

### 5.1.2 Wet Component Models

Although the validity of the hydrostatic model is rather established, the modeling of ZWD is on the contrary a hard task due to the high spatial and temporal variations [2]. Models for the wet component have been proposed in the literature, as well [6, 12, 13]. All models depend on the surface temperature  $T_s$  and surface water vapor pressure  $e_s$ . For instance, the Saastamoinen model proposed in [6] is

$$ZWD = 2.277 \times 10^{-3} \left( \frac{1255}{T_s(z)} + 0.05 \right) e_s(z) \quad (5.9)$$

where  $T_s(z)$  is  $K$  degree and  $e_s(z)$  is in mbar.

Unfortunately, these models are much more critical because, to be properly calibrated, they need different external measurements to follow the high spatial and temporal variations of the wet component. Such measurements are usually carried out via radiosonde, but these data are typically only available in very few areas. Some more recent works have explored the possibility of 3-D reconstruction of the water vapor atmospheric distribution applying a sort of tomography-like technique to dense geodetic networks of GPS receivers [14]. GPS networks are typically unable to spatially sample the wet tropospheric delay for the issue of correcting SAR interferograms. In the following, let consider the case of absence of turbulence, i.e., spatially homogeneous conditions

so that the spatial variations of ZWD are only considered as a variation of the surface water vapor pressure due to changes of the height, i.e.,  $z$ . As for the hydrostatic component, typically  $e_s$  may also show seasonal variations.

## 5.2 GPS Zenith Delay Estimation

The GPS system calculates the position of a receiving station by precisely timing the signals transmitted by the GPS satellites. Receivers determine the transit time from the signal transmitted from at least four satellites and compute the distance to each satellite by using the speed of light. The availability of at least three delays allows evaluating the location of the receiver with accuracies which are in the order of centimeters. Additional phase and code measurements account for inaccuracies of the receiver clocks whose bias is considered as an additional parameter. As pointed out in the previous section when radio signals propagate through the atmosphere, they are however delayed due to different refractivity indices of each layer of the atmosphere. Therefore, similarly to the case of SAR systems, the atmosphere has a significant effect on the propagation of a GPS signal: variations of the refraction index with respect to the vacuum introduce time delays that affect the distance measurements, thus impacting the evaluation of the receiver location.

Atmospheric delay in radio signal propagation is the principal error source in GPS technology: one of the key tasks of GPS processing is to estimate and correct their effects. The APD provided for the GPS stations is normally referred to the zenith direction. GPS signals, however, arrive at the receiver following different slant range paths, and some models are required to map the zenith delay into the line-of-sight direction between the receiver and the GPS satellites. The slant tropospheric delay is the delay mapped into line-of-sight direction and is associated with the ZHD and ZWD through the hydrostatic and wet mapping function,  $m_h(\varepsilon)$  and  $m_w(\varepsilon)$ , respectively, where  $\varepsilon$  is the elevation angle related to the direction of arrival of the signal from the satellite. Hence, the slant tropospheric delay  $SD(\varepsilon)$  at an arbitrary elevation angle can be expressed as:

$$SD(\varepsilon) = m_h(\varepsilon)ZHD + m_w(\varepsilon)ZWD. \quad (5.10)$$

Typically, semiempirical mapping functions are used for this purpose and various forms have been proposed. Different mapping functions may be conveniently used for the hydrostatic and wet component [15]. Assuming a planar atmosphere at geometric elevation  $\varepsilon$ , the simplest mapping function is given by  $1/\sin\varepsilon$ . This is an accurate approximation only for high elevation angles and for a small degree of bending [16]. GPS signals are however acquired typically with elevation angles spanning a wide range. More complex mapping functions have been therefore proposed in GPS literature to handle the problem of

relating slant and zenith delays. They use either surface meteorology measurements and site location (as CFA2.2 [5], MTT [8], [12], and Lanyi [17]) or only site location and time of year, as the Niell mapping function in [15]. The latter have the advantage of not using any parametrization in terms of meteorological conditions, but depend only on the site latitude and can be therefore adopted on a global scale. In modern GPS software, such as the *Gipsy-OASIS* software developed by the Jet Propulsion Laboratory (JPL) which has been exploited in the present work, the user has options for selecting the a priori model for the hydrostatic component evaluation. In order to avoid the necessity to access to external surface pressure measurements the mapping from zenith to slant delay is exploited to evaluate, starting from 5.10 observations collected at different elevation angles, the zenith delay. The Niell mapping functions [15] can be expressed as follows:

$$m(\varepsilon) = m(\varepsilon, a, b, c) + \Delta m(\varepsilon, z) \quad (5.11)$$

where  $m(\varepsilon, a, b, c)$  is the Herring mapping function [18] normalized to unity at zenith and  $\Delta m(\varepsilon, z)$  is the analytic height correction present only for the hydrostatic component. The Herring mapping function can be generally written as:

$$m(\varepsilon, a, b, c) = \frac{1 + \frac{a}{1 + \frac{b}{1+c}}}{\sin \varepsilon + \frac{a}{\sin \varepsilon + \frac{b}{\sin \varepsilon + c}}} \quad (5.12)$$

where  $a_h, b_h$ , and  $c_h$  are the coefficients used for the Hydrostatic component whereas  $a_w, b_w$ , and  $c_w$  are used for the wet component. The hydrostatic parameters  $a_h, b_h$ , and  $c_h$  are time ( $t$ ) and latitude ( $\phi$ ) dependent. The generic parameter  $a_h$  at latitude  $\phi$  and at time  $t$  from January 0.0 (in UT days) is given by

$$a_h(\phi, t) = a_{avg}(\phi) + a_{amp}(\phi) \cos \left[ 2\pi \frac{t - T_0}{365.25} \right] \quad (5.13)$$

where  $T_0$  is taken as Day-Of-Year (DoY) (i.e.,  $T_0 = 28$ ) [15]. The same procedure is followed for the parameters  $b$  and  $c$ . The parameters  $a_{avg}(\phi)$  and  $a_{amp}(\phi)$  in (5.13), as well as  $b_{avg}(\phi)$  and  $b_{amp}(\phi)$  and  $c_{avg}(\phi)$  and  $c_{amp}(\phi)$ , can be evaluated via linear interpolation of the values included in a Table in [15]. The term  $\Delta m(\varepsilon, z)$  is the analytic height correction, which can be expressed as

$$\Delta m(\varepsilon, z) = \left[ \frac{1}{\sin \varepsilon} - m(\varepsilon, a_t, b_t, c_t) \right] z \quad (5.14)$$

being  $z$  as usual the height of the station above the sea level  $m(\varepsilon, a_t, b_t, c_t)$  is the Herring mapping function in (5.12). The parameters  $a_t, b_t, c_t$  which are not latitude dependent are also tabled [15]. GPS is able to resolve atmospheric delays from variations of the position of the station because 1) it carries out quasi continuous measurement over the time, thus being able to

detect path delay changes due to the turbulent component with exhibits large spatial and temporally variable components, 2) separates long terms (seasonal) propagation delay variations from displacements of the station thanks to the availability of measurements corresponding to a set of elevation angles. The latter feature allows writing (5.10) for different values of  $\varepsilon$  for which different measurements of the delay (including the term accounting for the variations of the position of the station) are available. SAR systems on the other hand perform (in the best case) weekly measurements and, more important, use just a single elevation angle. This characteristic determines the impossibility to perform a separation between the atmospheric delay and the desired displacement based on the single measurement (one equation with two unknowns). As a matter of fact, this separation is only possible by using proper filtering (with multiple measurements) based on a different statistical characterization of the two terms (displacement and atmospheric delay) over the time. Such a characterization, as already anticipated and demonstrated in the experimental results, may however be inappropriate for atmospheric delay contributions characterized by seasonal variations whose statistical characterization becomes mixed with the one of the displacement contribution.

### 5.3 Impact of the Atmospheric Propagation Delay on Multipass DInSAR data

DInSAR phase measurements in the generic  $i$ -th pass (referred to a master image), and in a given azimuth-range  $(x, r)$  pixel can be expressed as a sum of different contributions

$$\varphi_i(x, r) = \frac{4\pi}{\lambda} \delta r_i + \varphi_{zi} + \varphi_{ai} \quad (5.15)$$

where  $\lambda$  is the wavelength,  $\delta r_i$  is the (desired) displacement,  $\varphi_{zi}$  is the residual topography (usually affecting the interferometric signal over a local basis), and  $\varphi_{ai}$  is the APD

$$\varphi_{ai} = \frac{4\pi}{\lambda \sin \varepsilon} ZD_i \quad (5.16)$$

where  $\pi/2 - \varepsilon$  is the incidence angle and  $ZD_i$  is the zenith APD difference between the  $i$ -th and the master (reference) acquisition. It should be noted that, as  $\varepsilon$  assumes in the SAR case typically large values, I have considered for the SAR case the approximation of the mapping function to  $1/\sin \varepsilon$ . In Advanced-DInSAR (A-DInSAR) processing, the atmosphere is typically separated (after phase unwrapping) from the displacement component by assuming a low-pass spatial and high-pass temporal statistical characterization behavior. Wide application of DInSAR technique on data acquired by the previous generation of satellite sensors has shown that this assumption is valid for the

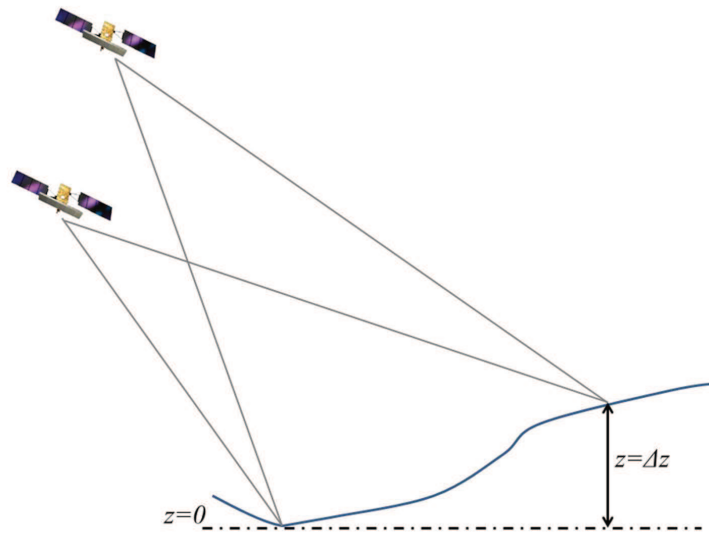


**Figure 5.1:** Diagram schematically showing the observations of points located at different heights on the ground in two passes of the SAR system.

analysis of long-term dataset-spanning decades and acquired with low temporal sampling (typically on a monthly basis). However, new generation SAR sensors and constellations of sensors are capable of acquiring images over a few days and hence are able to collect large data stacks on the basis of the single year or fraction of a year: the assumption on the statistical characterization of the atmosphere is no longer sufficient. In particular, mainly the hydrostatic, but also the wet component may exhibit seasonal variations which introduce in the APD the presence of slowly temporal variations (temporal phase trends) affecting especially regions characterized by high topographic variation. Classical A-DInSAR processing is in this case unable to operate the separation between APD and deformation delay on the basis of the fast temporal change behavior. For the aim of the derivation of the robust procedure for the assimilation of the GPS measurements in the SAR processing chain, it has been assumed that the atmospheric delay is linearly varying with the height. I investigate first this point with reference to the slant hydrostatic delay component. From the Saastamoinen hydrostatic model, expressed in formula (5.6), it is clear that ZHD directly depends on the height of the receiving station and on the value of surface pressure. First of all, the pressure distribution may show horizontal variations that can introduce spatial variations of the ZHD. However, the variations of the total pressure are typically distributed over areas which are much larger than the size of scenes acquired by current SAR sensors. InSAR is based on double differences: i.e., differences along the time performed at

the interferogram generation stage, and spatial differences (spatially constant phase signals are cancelled out by the operation of referencing the results to the deformation of a reference, typically not moving, point). For interferometric purposes, the variation of the propagation delay between the acquisition dates, namely,  $t_1$  and  $t_2$ , associated with acquisitions  $i$  and  $j$  is of interest. Figure 5.1 shows the double differencing operation involving two observations and two points on ground at a height 0 and  $z$ . The differential ZHD between a given satellite at time instant  $t_1$  and  $t_2$  and points located at 0 and  $z$ , hereafter referred to as  $\Delta ZHD_{z,ij}$ , is given by

$$\Delta ZHD_{z,ij} = (ZHD_{z,j} - ZHD_{z,i}) - (ZHD_{0,j} - ZHD_{0,i}) \quad (5.17)$$

where  $ZHD_{z,i}$ , is the hydrostatic delay in the zenith direction measured at the epoch corresponding to the  $i$ -th acquisition at height  $z$ . By exploiting the Saastamoinen model in (5.6), (5.17) can be written as the sum of two components. The first one is depending on the topographic variation  $z$  between the two corresponding points; the second one depends on the pressure variations between the first and second dates of two generic points with respect to a common reference point. In [19], an analysis of the hydrostatic delay variation has been conducted: It has been showed that the contribution related to a topographic change is typically negligible, whereas the contribution related to pressure changes is relevant for interferometric processing purposes. Hence, by considering the presence of pressure variation between the two acquisition dates, the associated hydrostatic delay component can be written as

$$\Delta ZHD_{z,ij} = \frac{2.278 \times 10^{-3}}{1 - 2.66 \times 10^{-3} \cos 2\phi} [\Delta P_{sj}(z) - \Delta P_{si}(z)] \quad (5.18)$$

where the generic  $\Delta P_{si}(z) = P_{si}(0)$  is the pressure variation between the point located at height 0 and  $z$ , at a generic time instant corresponding to the  $i$ -th acquisition. Accordingly, the pressure variation between the receivers is

$$\Delta P_{s,j}(z) - \Delta P_{s,i}(z) = [P_{0j} - P_{0i}](e^{-\frac{z}{H}} - 1). \quad (5.19)$$

By assuming  $\frac{z}{H} \ll 1$ , the relation in (5.17) can be written as

$$\Delta ZHD_{z,ij} = \frac{2.278 \times 10^{-3}}{1 - 2.66 \times 10^{-3} \cos 2\phi} [P_{0j} - P_{0i}] \frac{z}{H} \quad (5.20)$$

hence, the vertical structure of the hydrostatic delay component related to pressure variation is dependent on the vertical profile of the total pressure and can be approximated as a linear model with respect to the height variable  $z$ . A temporal variation of the pressure at the reference height (i.e., 0) is linearly scaled with the height  $z$ . Water vapor shows faster variations with the height [7]; nevertheless, for the scope of integration of GPS ZD measurements in the SAR processing chain, this component can be approximated as a linear

function of the height. Higher order expansions could be carried out to better fit such a variation. However, the simple linear approximation between APD and topography is well supported by experimental evidence, as it will be shown in section 5.5. In fact, the simple linear model, adopted in this work, shows that even with the first-order expansion, it is possible to take benefit of GPS delay measurements for the correction of the delay excess due to the atmosphere in DInSAR processing. The linear approximation is also supported by specific investigations of the total zenith delay measurements derived by the GPS measurements. It is worth noting that the linear approximation between atmospheric delay and topography can be also exploited for performing a “blind” removal of the atmospheric component in DInSAR products, especially in areas where a dense GPS network is not present. However, this “blind” compensation involves some critical issues, as it will be discussed later.

## 5.4 Integration of GPS Tropospheric Delay Measurement in DInSAR Data Processing

The delay measured by GPS can be used to compensate the APD disturbance in the DInSAR processing. However, GPS delay measurements are sampled spatially only in correspondence of the available stations; therefore, a strategy for the extrapolation of the APD contribution at the SAR pixel level is necessary. The procedure adopted for the integration of GPS atmospheric measurement in DInSAR data processing is based on two steps. In the first step, the GPS data are used to extract the coefficient that describes the ZD component associated with the vertical stratification of the troposphere. This step is carried out by using, thanks to the approximations discussed in the previous section, a simple linear model for the vertical structure of the APD component

$$ZD_i(x, r) = \alpha_{0i} + \alpha_{1i}z(x, r) \quad (5.21)$$

where  $z(x, r)$  is the topography of the area in the pixel  $(x, r)$  and  $\alpha_{1i}$  is the constant characterizing the vertical structuring of the tropospheric delay. The coefficients  $\alpha_{1i}$  and  $\alpha_{0i}$  are estimated from the GPS data via a simple Least Square approach on the  $K_i$  available stations at the time corresponding to the  $i$ -th acquisition

$$(\alpha_{0i}, \alpha_{1i}) = \arg \min_{u_{0i}, u_{1i}} \left[ \sum_{l=1}^{K_i} (ZD_i(x_l, r_l) - u_{0i} - u_{1i}z(x, r)) \right]^2. \quad (5.22)$$

The subsequent step is aimed at the comparison between the ZD, estimated from the GPS data with the stratification assumption, and the radar data. The estimated path delays patterns from (5.21) are translated in the atmospheric phase delay through the (5.16) and then compared at the level of wrapped phase

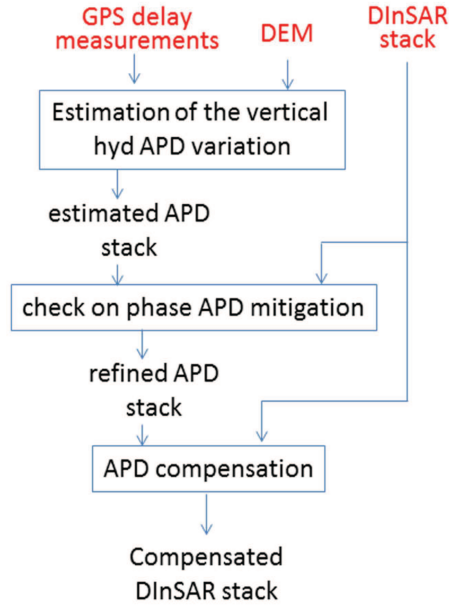


Figure 5.2: Block diagram of the compensation procedure.

on the interferogram set, to check if the modeled delay introduces mitigation of the atmospheric component. In particular, for the generic  $q$ -th interferogram, the following phase variation mitigation index is used:

$$I_q = \left\| G \left\{ e^{-j(\varphi_{wq}(x,r) - \varphi_{aq}(x,r))} \right\} \right\|^2 \left\| G \left\{ e^{-j\varphi_{wq}(x,r)} \right\} \right\|^2 \quad (5.23)$$

where  $\varphi_{wq}(x, r)$  is the wrapped phase of the  $q$ -th interferogram and  $\varphi_{aq}(x, r) = \varphi_{aj}(x, r) - \varphi_{ai}(x, r)$  is the estimated atmospheric delay evaluated from the  $j$ -th and  $i$ -th acquisitions involved in the  $q$ -th interferogram and  $G\{\cdot\}$  is an operator that carries out a spatial low-pass filtering. The variations  $\kappa = \alpha_{1j} - \alpha_{1i}$  for which  $I_q > 0$  are then inverted to retain the final estimation of the vertical stratification parameters, according to the following equation:

$$\mathbf{A}\boldsymbol{\alpha} = \boldsymbol{\kappa} \quad (5.24)$$

where the vector  $\boldsymbol{\kappa}$  collects the  $\kappa_q$  coefficients, the vector  $\boldsymbol{\alpha}$  collects the refined (final) stratification coefficients  $\alpha_{1i}$ , and  $\mathbf{A}$  is the incidence matrix that describes the interferogram related to the acquisition coupling, see [20] for further details.

Since spatially constant phase signals are canceled out by the operation of referencing the results to a common, not moving, reference point, for each acquisition coupling the coefficients  $\alpha_{0i}$  is not considered in the system of equations

defined in (5.24). It is now worth to note that a different option based on a simple “blind” removal of a phase component correlated with the interferogram measurements could be implemented, that is an estimation of the coefficients  $\alpha_{1i}$  directly from SAR data [21] thus avoiding the use of GPS data. However, such an approach could be critical in cases where the deformation signal (of tectonic as well as volcanic nature) is correlated with the topography as well: such a useful signal component would be in fact filtered out together with the atmospheric contribution by the “blind” removal of topographic components. Our approach aims on the other hand to integrate the GPS, which is able to separate atmosphere and deformation based on observation carried out with different elevation angles, as additional information to overcome this limitation. As a matter of fact, (5.23) is used only to check whether the signal corresponding to a stratified atmosphere estimated by the GPS network is consistent with the observed interferometric SAR phase measurements. The block diagram of the GPS aided APD compensation is shown in Figure 5.2. All the GPS measurements (for a generic interferometric acquisition pair) are used together with the DEM to estimate the vertical hydrostatic APD variation; hence, the APD stack estimated with the aid of GPS measurements is generated. Thus, the estimated APD screens are checked, via a proper phase mitigation variation index, to eliminate incorrect APD estimations; finally, a refined stack is generated and hence used to carry out the final compensation. It should be noted that the use of external GPS data for APD compensation should reduce the problems relative to the cancelation of topographic displacements, with respect to an estimation carried out by using only the interferometric SAR data.

## 5.5 Experimental Results

The case study analyzed in this work concerns the 2009 L’Aquila earthquake occurred in the region of Abruzzo in central Italy. The main shock happened on April 6, 2009 and was rated 6.3 Mw; its epicenter was near L’Aquila, the capital of Abruzzo, which together with surrounding villages suffered most damage. The GPS-aided APD compensation algorithm, described in section 5.4, has been tested on two SAR datasets acquired on ascending and descending passes of the COSMO-SkyMed constellation over the area hit by the earthquake. Due to the emergency phase, Italian Space Agency (ASI) adopted a priority acquisition program on L’Aquila area; in fact, the COSMO-SkyMed constellation was able to acquire data with a 5 days (on average) temporal separation: the resulting dataset has unique characteristics for scientific use. The ascending COSMO-SkyMed dataset, composed of 33 acquisitions acquired in about 6 months from April 4, 2009 to October 10, 2009 (see Table 5.1), 32 of which in a postseismic phase of the main shock occurred on April 6. Tropospheric delays were calculated from continuous or episodic GPS stations already in place or installed shortly after the main shocks using the GIPSY-OASIS soft-

## CSK ASCENDING DATASET

Date	Temporal baseline [d]	Spatial baseline [m]	Date	Temporal baseline [d]	Spatial baseline [m]
04 Apr 2009	-120	550	25 Jul 2009	-8	-136
12 Apr 2009	-112	119	02 Aug 2009	0	0
13 Apr 2009	-111	84	03 Aug 2009	1	361
20 Apr 2009	-104	-300	10 Aug 2009	8	106
29 Apr 2009	-95	-470	18 Aug 2009	16	-127
06 May 2009	-88	-717	19 Aug 2009	17	-90
14 May 2009	-80	-391	26 Aug 2009	24	-258
30 May 2009	-64	-16	03 Sept 2009	32	-212
31 May 2009	-63	-138	04 Sept 2009	33	-149
07 June 2009	-56	-211	11 Sept 2009	40	-120
15 June 2009	-48	282	19 Sept 2009	48	160
16 June 2009	-47	213	20 Sept 2009	49	305
23 June 2009	-40	127	27 Sept 2009	56	487
02 July 2009	-31	-226	05 Oct 2009	64	392
09 July 2009	-24	-250	06 Oct 2009	65	299
17 July 2009	-16	-373	13 Oct 2009	72	40
18 July 2009	-15	-189			

**Table 5.1:** Description of the dataset acquired by the COSMO-SkyMed constellation in ascending mode. Temporal and spatial baselines are measured with respect to the acquisition of August 2, 2009. The spatial baselines refer to the perpendicular baselines exploited to compute the interferograms; they are measured in meters [m]. Temporal baselines are measured in days [d] elapsed from the reference acquisition.

ware. In the time interval covered by the InSAR acquisitions, a number of 24 and 40 stations were available on average within the distances of 50 and 100 km, respectively. In Figure 5.3, the distribution of the GPS stations, overlaid on a DEM of L’Aquila area, is shown. In order to estimate ZWD, the GPS data were analyzed separately for each UTC day using the *Gipsy-OASIS II* software package in Precise Point Positioning mode [22]. ZWDs were determined together with the site daily average position and receiver clocks. The receiver’s clock was modeled as a white noise process with updates at each measurement epoch, and ZWD was modeled as a random walk with an accuracy of  $10.2 \text{ mm } h^{-1/2}$ . Satellite final orbits and clocks were obtained via anonymous FTP (<ftp://sideshow.jpl.nasa.gov/pub>) from the Jet Propulsion Laboratory and  $15^\circ$  cutoff was employed. For more details, see [23]. The Niell Mapping Function was used in the processing because of its independence from surface meteorology, small bias, and low seasonal error [15, 24]. Niell et al. evaluated the impacts of the uncertainties of the Niell hydrostatic and wet mapping functions on ZWD. The uncertainty of the hydrostatic mapping function at  $5^\circ$  elevation angle is 1%, and results in an uncertainty in the estimated ZWD of about 3 mm (about 0.5 mm of precipitable water vapor Precipitable Water Vapour (PWV)) for the lowest elevation angle 24-h solutions when the site positions are estimated along with ZWD. For the wet mapping function, the uncertainty at  $5^\circ$  elevation angle is 0.5%. To show the effects of the atmospheric component, the tropospheric phase delays estimated by the GPS stations are reported in Figure 5.4. They are sampled in correspondence to the SAR image acquisition times of the ascending COSMO-SkyMed SAR dataset, which has been exploited in the experimental part of this work. In particular, the wet delays shown in Fig-

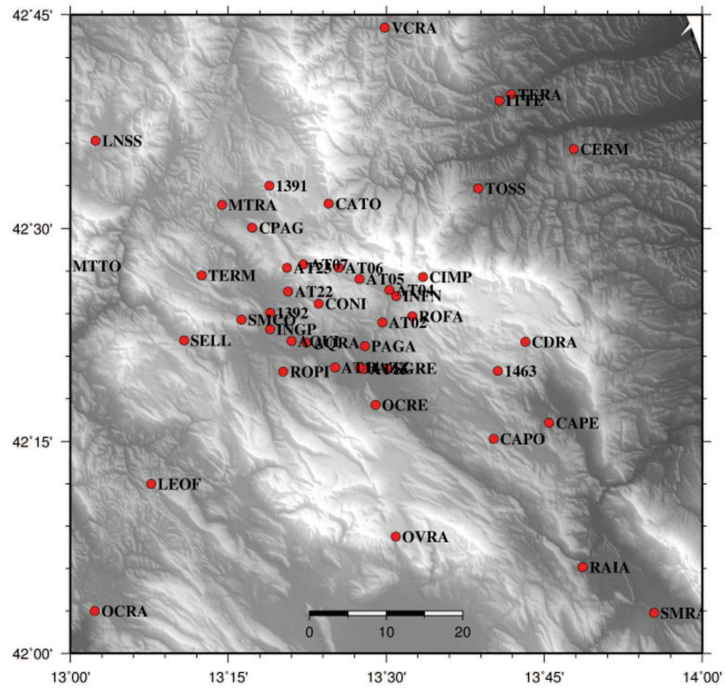


**Figure 5.3:** Distribution of the GPS stations (red dots) overlaid on a DEM of L'Aquila area.

Figure 5.4 are associated with two stations (respectively the AQRA and CATO station, as evidenced on the top of each plot), which have been chosen for their different altitude positions, in order to demonstrate the different behavior of the atmospheric delay with different altitude values. On the top annotations of each plot are reported (from left) the name of the GPS station, its latitude and longitude coordinates, its altitude and the standard deviation of the GPS measurement, respectively. It can be noted that for both stations, the tropospheric delay has a variation over the time characterized (on average) by an increase of the delay going from winter to summer, thus emphasizing a seasonal change of the zenith delay values. Moreover, it is evident that the altitude dependency of the atmospheric delay component estimated at each station: for the AQRA GPS station (upper image), located at a height of 747 m, the delay values are characterized by a variation (range interval) higher than that of the CATO station located at 1385 m of altitude. In fact, the standard deviation for the AQRA station has a value of 4.24 cm, whereas for CATO, it assumes a lower value of 3.85 cm. An analysis of the behavior of the GPS atmospheric delay along the vertical direction has also been carried out to test the soundness of

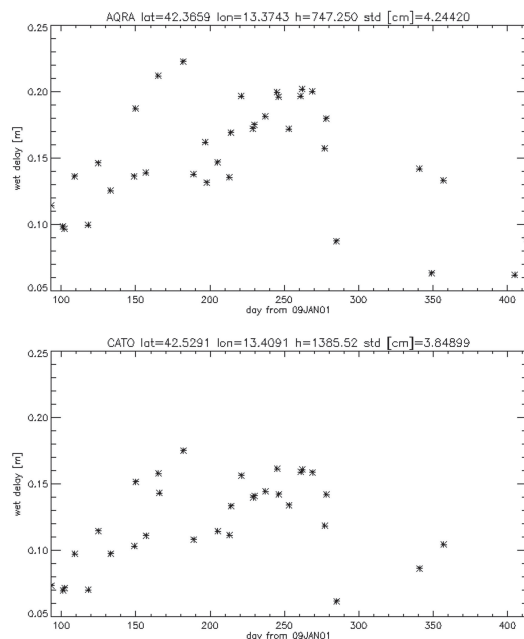


**Figure 5.4:** Atmospheric (zenith) wet delays measured by two GPS stations; on the horizontal axis are reported the days from the 1st Jan. 2009

the linear approximation in (5.21). In Figure 5.5 (upper image), it is shown an example of GPS-derived atmospheric signal for a certain acquisition time (October 5, 2009). The Figure has been obtained by a scaling of the DEM according to a linear regression of the measurements with the height. The dots in the Figure correspond to the GPS stations. In Figure 5.5 (bottom image), it is shown the estimated GPS delay versus the height derived for the same acquisition time. The color of each dot corresponding to GPS station is set according to the wet delay map in the upper image of Figure 5.5. It is worth to note that the agreement with the linear model is good. Similar results have been observed also in most of the acquisitions: In Figure 5.6, other examples of representation of the GPS delay versus the height for some epochs are shown. All the plots show a reasonable fit with the linear model: an evidence that was found on almost all the processed epochs. As already pointed out in section 5.4, the validity of the linear model assumption also proves that the “blind” option of using the linear regression between InSAR phase and height to estimate and compensate the stratified APD component directly on SAR data, as in [21], is viable. This would be helpful particularly in areas where a dense GPS network is not available. However, it is again stressed that in this case a filtering of any signal component correlated with the topography would be



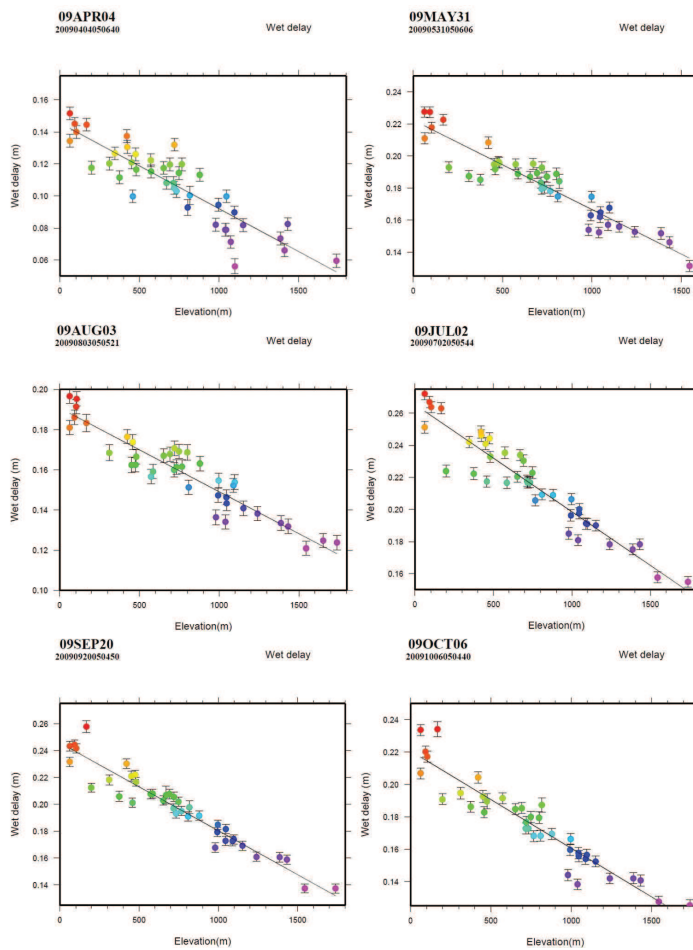


**Figure 5.6:** Plots of the estimated GPS delay over the different stations with respect to the height. The different images correspond to different days

ble [25]. The multipass DInSAR processing has been carried out by exploiting the enhanced spatial differences (ESD) approach [26], which is an extension of the original SBAS algorithm [20] based on the incorporation of a model using spatial differences for the preliminary estimation of the residual topography and mean deformation velocity directly from the wrapped phase values to improve the final phase unwrapping stage. The procedure described in section 5.3 has been incorporated into the ESD processing chain and applied to the available dataset. In Figure 5.7, it is shown an example of APD compensation on a postseismic interferogram generated from the acquisitions of April 20, 2009 and July 2, 2009, acquired in the ascending mode. The compensated interfer-

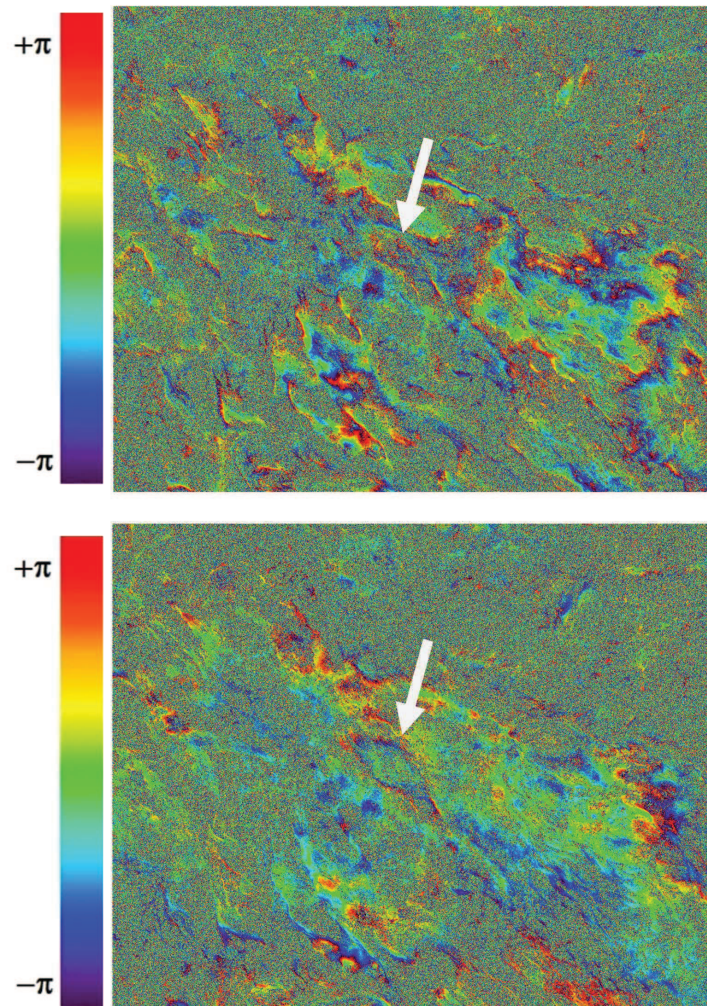


**Figure 5.7:** Postseismic interferogram (April 20, 2009 and July 2, 2009) before (upper image) and after (lower image) the compensation of the atmospheric phase delay from GPS data. Azimuth is vertical and is approximately coincident with the S-N direction, range is horizontal and is approximately coincident with the W-E direction: the area covered is of about  $40 \text{ km} \times 40 \text{ km}$ .

ogram (lower image) resulting from the integration of the GPS tropospheric delay measurements shows a dramatic reduction of the phase variations due to the APD component with respect to the original interferogram. Moreover, the weak (compared to the coseismic) pattern describing the postseismic ground displacement in the area of L'Aquila highlighted by the white arrow in both

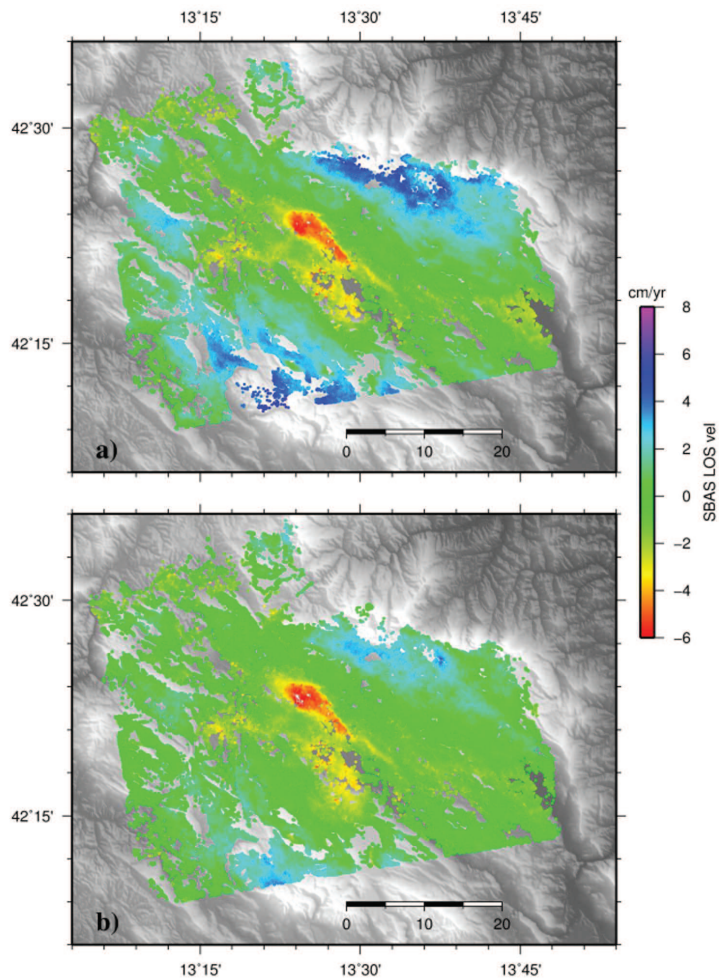


**Figure 5.8:** Postseismic velocity maps, overlaid on a grayscale DEM, corresponding to the DInSAR processing of the ASCENDING COSMO-SkyMed dataset (a) without and (b) with the GPS-aided compensation module. The axes report longitude and latitude values of the imaged area.

interferograms is much more evident and easily detectable in the interferogram compensated with the aid of GPS data. The uncompensated and compensated interferometric stacks were both processed via the classical ESD processing chain to derive the deformation time series. For both cases, comparison with GPS deformation measurements showed, as in [27], an excellent match in the deforming area of L'Aquila and Paganica. Figure 5.8 shows the (postseismic) mean velocity maps, evaluated from the deformation time series, superimposed

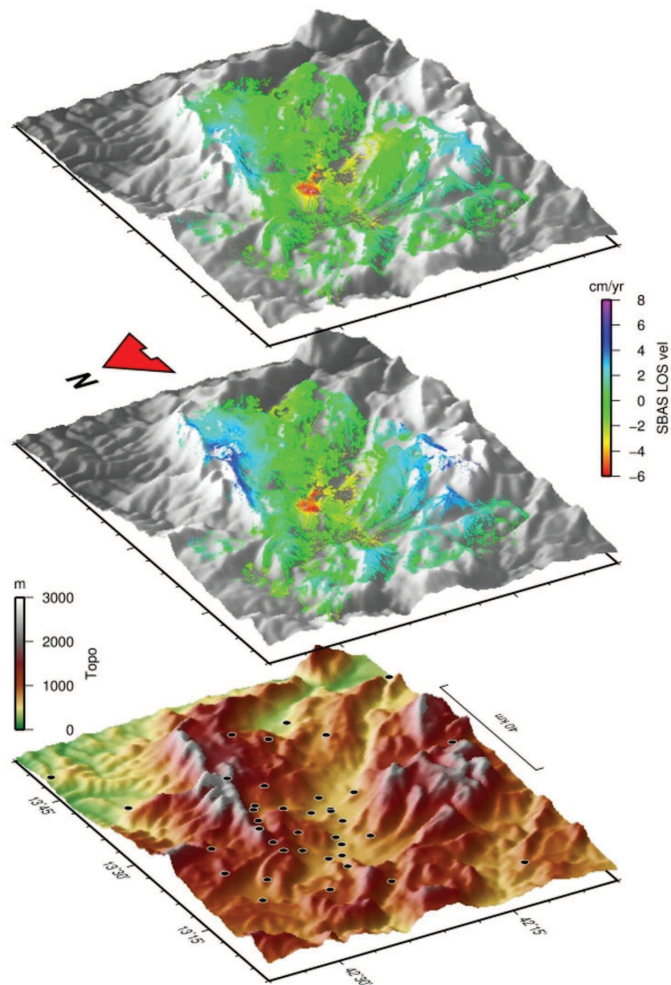


**Figure 5.9:** (Upper image) The same postseismic velocity map of 5.9(b) corresponding to the GPS-aided processing overlaid to a DEM in grayscale; (middle image) the same as the upper image but for the velocity map of Figure 5.9(a) corresponding to the result obtained without the integration of GPS measurements; (bottom image) distribution of the GPS stations on the 3-D map in which colors encode the height according to hypsometric tints. The axes report longitude and latitude values of the L'Aquila area.

on a grayscale DEM of L'Aquila territory. The results indicate for the uncompensated stack, shown in Figure 5.8(a), the presence of a significant inflation

## CSK DESCENDING DATASET

<i>Date</i>	<i>Temporal baseline [d]</i>	<i>Spatial baseline [m]</i>	<i>Date</i>	<i>Temporal baseline [d]</i>	<i>Spatial baseline [m]</i>
08 Apr 2009	-104	-695	21 July 2009	0	0
16 Apr 2009	-96	-251	30 July 2009	9	-501
10 May 2009	-72	61	06 Aug 2009	16	-513
11 May 2009	-71	216	14 Aug 2009	24	-362
18 May 2009	-64	399	30 Aug 2009	40	-75
27 May 2009	-55	-88	31 Aug 2009	41	-144
03 June 2009	-48	86	07 Sept 2009	48	-82
12 June 2009	-39	-674	15 Sept 2009	56	-184
19 June 2009	-32	-466	16 Sept 2009	57	-351
28 June 2009	-23	-83	23 Sept 2009	64	-514
05 July 2009	-16	48	01 Oct 2009	72	-501
13 July 2009	-8	70	02 Oct 2009	73	-434
14 July 2009	-7	-9	09 Oct 2009	80	-174

**Table 5.2:** Description of the dataset acquired by the COSMO-SkyMed constellation in descending mode. Temporal and spatial baseline are measured with respect to the acquisition of 21st July 2009. The spatial baselines refer to the perpendicular baselines exploited to compute the interferograms and are measured in meters [m]. Temporal baselines are measured in days [d] elapsed from the reference acquisition.

signal in the mountainous areas: this effect is due to the reduction of the propagation delay on areas with higher topographic level. On the other hand, for the APD compensated stack in 5.8(b), the results show overall a substantial reduction of the anomalous signal, thus confirming the beneficial effect of the integration of GPS measurements in the DInSAR processing. Figure 5.9 displays the same postseismic mean velocity maps of Figure 5.8 superimposed on a 3-D DEM of L'Aquila area in grayscale. In this case, it can be even better appreciated with respect to Figure 5.8, the mitigation of the atmospheric contribution achieved thanks to the GPS-aided compensation module. The area exhibiting the most significant postseismic deformation signal, reaching a value of about  $-6$  cm/yr, matching the red pattern in figures 5.8(a) and 5.8(b) and hence also in Figure 5.9 (middle and upper image, respectively), corresponds to the Paganica-San Demetrio fault. The bottom image in Figure 5.9 shows the dense GPS stations network overlaid on a 3-D physical relief map of the imaged area, in which colors encode different elevation values according to hypsometric tints. The multipass DInSAR processing has been also carried out on a descending COSMO-SkyMed dataset, composed of 26 SAR images, acquired in about 6 months from April 8, 2009 to October 9, 2009 (see table 5.2). All acquisitions have been acquired in a postseismic phase. Figure 5.10 shows the postseismic mean velocity maps, superimposed on a grayscale DEM relative to L'Aquila area, which have been evaluated from the deformation time series obtained through the DInSAR processing of the descending COSMO-SkyMed dataset (see table 5.2). Figure 5.10(a) displays the postseismic mean velocity map of the uncompensated stack, whereas Figure 5.10(b) shows the postseismic mean velocity map obtained via the DInSAR processing with the GPS aided compensation module. Figure 5.11 displays the same postseismic mean velocity maps of Figure 5.10, but superimposed on a 3-D grayscale DEM relative to

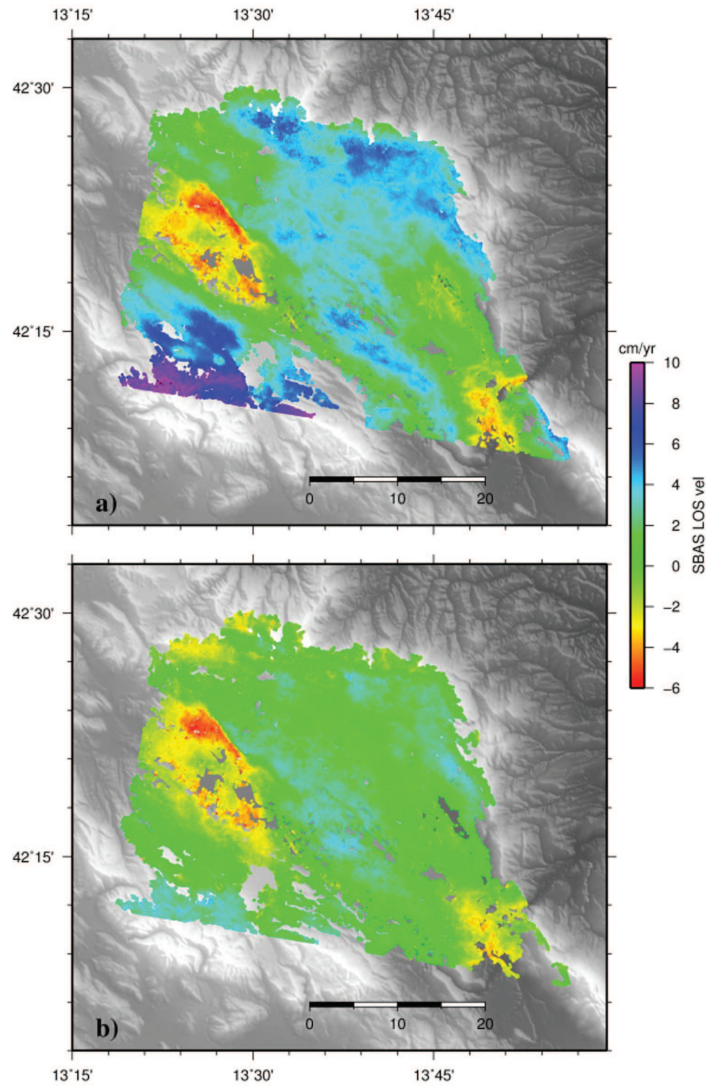


**Figure 5.10:** Postseismic velocity maps, overlaid on a grayscale DEM, corresponding to the DInSAR processing of the DESCENDING COSMO-SkyMed dataset (a) without and (b) with the GPS-aided compensation module. The axes report longitude and latitude values of the imaged area.

L'Aquila area. The bottom image in Figure 5.11 shows again the dense GPS stations network overlaid on a 3-D physical relief map of the imaged area. It is well evident in Figure 5.10(a), as well as in the middle image of Figure 5.11,

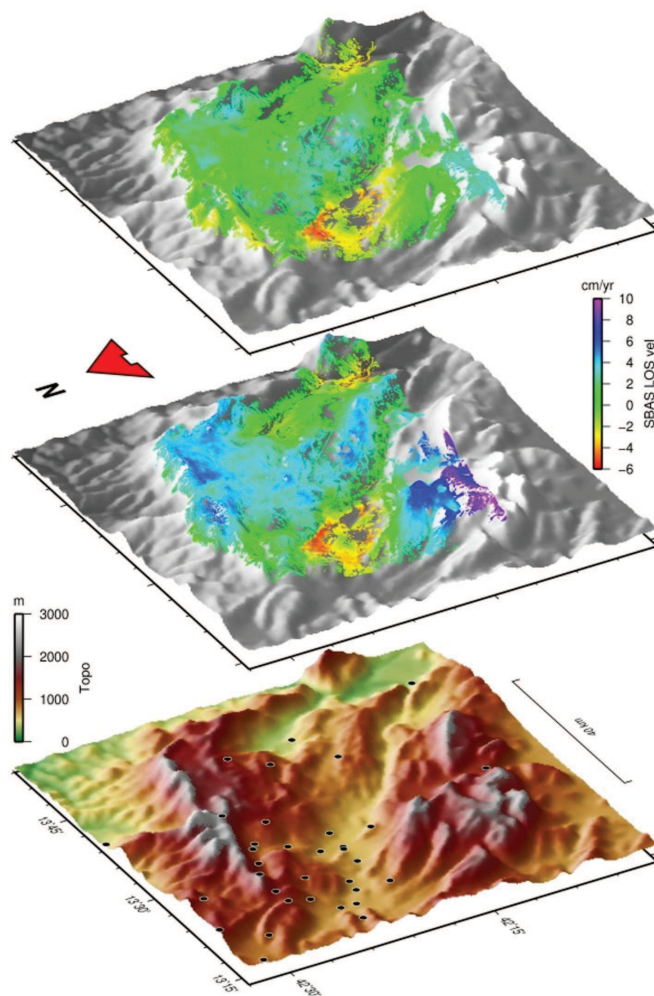


**Figure 5.11:** (Upper image) The same postseismic velocity map of Figure 5.10(b) corresponding to the GPS-aided processing overlaid to a DEM in grayscale; (middle image) the same as the upper image but for the velocity map of Figure 5.10(a) corresponding to the result obtained without the integration of GPS measurements; (bottom image) distribution of the GPS stations on the 3D map in which colors encode the height according to hypsometric tints. The axes report longitude and latitude values of the imaged area.

a deformation pattern in the mountainous region. This is due again to the atmospheric artifacts which impair to some level the geophysical interpretation

of the measured deformations. The DInSAR processing with the GPS-aided compensation module strongly mitigates this significant inflation signal, as it can be clearly seen in Figure 5.10(b), as well as in the upper image of Figure 5.11, thus assessing that the observed inflation was indeed associated with the APD effects. Finally, also in this case the post-seismic deformation pattern (the red area), which is associated with the Paganica-San Demetrio fault, is well recognizable. It is possible to obtain an independent validation of the results presented here by comparison with results of the geophysical modeling obtained using completely independent data. Reference [28] presents the results of the inversion of coseismic and postseismic deformations following the L'Aquila event using Advanced Land Observation Satellite (ALOS), ENVISAT, and high-precision leveling. These data show that the coseismic and postseismic deformation signals are aligned along the Paganica-San Demetrio Fault with a minor, subtle signal on the Campotosto Fault. Inversion of the deformation data shows that both the coseismic and postseismic deformation is well reproduced by slip on the PDF and the CF elements. This observation strongly supports the hypothesis that the topographic correlated signal observed in the COSMO-SkyMed time series is an atmospheric artifact that is effectively removed in the lower images in Figures 5.8 and 5.10 by using the additional information on the troposphere gained by GPS.

## 5.6 Acknowledgment

The author would like to thank the Italian Space Agency (ASI) for providing the COSMO-SkyMed dataset used in this work to the Italian Department of Civil Protection in the framework of the L'Aquila earthquake emergency.

# References

- [1] R. F. Hanssen, *Radar interferometry: data interpretation and error analysis*. Springer, 2001, vol. 2.
- [2] M. Bevis, S. Businger, T. A. Herring, C. Rocken, R. A. Anthes, and R. H. Ware, "Gps meteorology: Remote sensing of atmospheric water vapor using the global positioning system," *J. Geophys. Res.*, vol. 97, no. D14, pp. 15 787–15 801, 1992.
- [3] F. Meyer, R. Bamler, N. Jakowski, and T. Fritz, "The Potential of Low-Frequency SAR Systems for Mapping Ionospheric TEC Distributions," *IEEE Geoscience and Remote Sensing Letters*, vol. 3, no. 4, pp. 560–564, Oct 2006.
- [4] B. Puysségur, R. Michel, and J.-P. Avouac, "Tropospheric phase delay in interferometric synthetic aperture radar estimated from meteorological model and multispectral imagery," *Journal of Geophysical Research: Solid Earth (1978–2012)*, vol. 112, no. B5, 2007.
- [5] J. L. Davis, T. A. Herring, I. I. Shapiro, A. E. Rogers, and G. Elgered, "Geodesy by radio interferometry: Effects of atmospheric modelling errors on estimates of baseline length," *Radio Sci.*, vol. 20, no. 6, pp. 1593–1607, Dec. 1985.
- [6] J. Saastamoinen, "Atmospheric correction for the troposphere and stratosphere in radio ranging of satellites," *Geophys. Monograph Ser.*, vol. 15, pp. 247–251, Mar. 1972.
- [7] V. B. Mendes and R. B. Langley, "Zenith wet tropospheric delay determination using prediction models: Accuracy analysis," *Cartografia e Cadastro*, vol. 2, pp. 41–47, Jun. 1995.
- [8] M. Bevis, S. Businger, S. Chiswell, T. A. Herring, R. A. Anthes, C. Rocken, and R. H. Ware, "GPS meteorology: Mapping zenith wet delays onto precipitable water," *J. Appl. Meteorol.*, vol. 33, pp. 379–386, 1994.
- [9] H. Hopfield, "Two-quartic tropospheric refractivity profile for correcting satellite data," *Journal of Geophysical research*, vol. 74, no. 18, pp. 4487–4499, 1969.

- [10] G. Elgered, J. Davis, T. Herring, and I. Shapiro, "Geodesy by radio interferometry: Water vapor radiometry for estimation of the wet delay," *Journal of Geophysical Research: Solid Earth (1978–2012)*, vol. 96, no. B4, pp. 6541–6555, 1991.
- [11] K. E. Trenberth, "Seasonal variations in global sea level pressure and the total mass of the atmosphere," *Journal of Geophysical Research: Oceans (1978–2012)*, vol. 86, no. C6, pp. 5238–5246, 1981.
- [12] I. Ifadis, *The atmospheric delay of radio waves: modeling the elevation dependence on a global scale*. School Electrical Computer Engineering, Chalmers Univ. Technol., Gothenburg, Sweden, Tech. Rep, 1986.
- [13] J. Askne and H. Nordius, "Estimation of tropospheric delay for microwaves from surface weather data," *Radio Science*, vol. 22, no. 3, pp. 379–386, 1987.
- [14] A. Flores, G. Ruffini, and A. Rius, "4d tropospheric tomography using gps slant wet delays," in *Annales Geophysicae*, vol. 18, no. 2. Springer, 2000, pp. 223–234.
- [15] A. Niell, "Global mapping functions for the atmosphere delay at radio wavelengths," *Journal of Geophysical Research: Solid Earth (1978–2012)*, vol. 101, no. B2, pp. 3227–3246, 1996.
- [16] A. E. Niell, "Improved atmospheric mapping functions for VLBI and GPS," *Earth Planets and Space*, vol. 52, no. 10, pp. 699–702, 2000.
- [17] G. Lanyi, "Tropospheric delay effects in radio interferometry," *TDA Prog. Rep. 42-78, vol. April*, pp. 152–159, 1984.
- [18] T. A. Herring, "Modeling atmospheric delays in the analysis of space geodetic data," *Proceedings of Refraction of Transatmospheric signals in Geodesy*, eds. JC De Munck and TA Spoelstra, Netherlands Geodetic Commission Publications on Geodesy, vol. 36, 1992.
- [19] G. Fornaro and L. Paglia, "A comparison of atmospheric phase delay estimated by asar and meris over the campania area," *International Journal of Remote Sensing*, vol. 33, no. 5, pp. 1507–1528, 2012.
- [20] P. Berardino, G. Fornaro, R. Lanari, and E. Sansosti, "A new algorithm for surface deformation monitoring based on small baseline differential sar interferograms," *Geoscience and Remote Sensing, IEEE Transactions on*, vol. 40, no. 11, pp. 2375–2383, 2002.
- [21] F. Chaabane, A. Avallone, F. Tupin, P. Briole, and H. Maître, "A multi-temporal method for correction of tropospheric effects in differential sar interferometry: Application to the gulf of corinth earthquake," *Geoscience and Remote Sensing, IEEE Transactions on*, vol. 45, no. 6, pp. 1605–1615, 2007.

- [22] J. Zumberge, M. Heflin, D. Jefferson, M. Watkins, and F. Webb, "Precise point positioning for the efficient and robust analysis of gps data from large networks," *Journal of Geophysical Research: Solid Earth (1978–2012)*, vol. 102, no. B3, pp. 5005–5017, 1997.
- [23] Z. Li, E. J. Fielding, P. Cross, and J.-P. Muller, "Interferometric synthetic aperture radar atmospheric correction: medium resolution imaging spectrometer and advanced synthetic aperture radar integration," *Geophysical Research Letters*, vol. 33, no. 6, 2006.
- [24] A. Niell, A. Coster, F. Solheim, V. Mendes, P. Toor, R. Langley, and C. Upham, "Comparison of measurements of atmospheric wet delay by radiosonde, water vapor radiometer, gps, and vlbi," *Journal of Atmospheric and Oceanic Technology*, vol. 18, no. 6, pp. 830–850, 2001.
- [25] M.-P. Doin, C. Lasserre, G. Peltzer, O. Cavalié, and C. Doubre, "Corrections of stratified tropospheric delays in sar interferometry: Validation with global atmospheric models," *Journal of Applied Geophysics*, vol. 69, no. 1, pp. 35–50, 2009.
- [26] G. Fornaro, A. Paucullo, and F. Serafino, "Deformation monitoring over large areas with multipass differential sar interferometry: A new approach based on the use of spatial differences," *International Journal of Remote Sensing*, vol. 30, no. 6, pp. 1455–1478, 2009.
- [27] P. Webley, R. Bingley, A. Dodson, G. Wadge, S. Waugh, and I. James, "Atmospheric water vapour correction to insar surface motion measurements on mountains: results from a dense gps network on mount etna," *Physics and Chemistry of the Earth, Parts A/B/C*, vol. 27, no. 4, pp. 363–370, 2002.
- [28] D. Cheloni, R. Giuliani, E. D'Anastasio, S. Atzori, R. Walters, L. Bonci, N. D'Agostino, M. Mattone, S. Calcaterra, P. Gambino *et al.*, "Coseismic and post-seismic slip of the 2009 l'aquila (central italy) m<sub>i</sub> sub<sub>j</sub> w<sub>i</sub>/sub<sub>j</sub> 6.3 earthquake and implications for seismic potential along the campotosto fault from joint inversion of high-precision levelling, insar and gps data," *Tectonophysics*, vol. 622, pp. 168–185, 2014.



# Appendix A

The relationship between the Doppler centroid and the beating frequency is derived in this appendix. To do that, I will consider two range compressed looks defined in (25) and (26), in particular, fixing the two frequencies  $f_1 = f_0 - \Delta f/2$  and  $f_2 = f_0 + \Delta f/2$  the range envelopes can be approximated as follow:

$$\mathfrak{L}_1(t) = \text{rect} \left( \frac{t}{T_{obs}} \right) \exp -j4\pi \left( \frac{f_0 - \frac{\Delta f}{2}}{c} \right) R(t) \quad (25)$$

$$\mathfrak{L}_2(f, t) = \text{rect} \left( \frac{t}{T_{obs}} \right) \exp -j4\pi \left( \frac{f_0 + \frac{\Delta f}{2}}{c} \right) R(t) \quad (26)$$

If I consider the phase terms (25) and (26) and the second order polynomial approximation of  $R(t)$ :

$$\Phi_1(t) = 4\pi \left( \frac{f_0 - \frac{\Delta f}{2}}{c} \right) (R_0 + v_r t + a_r t^2) \quad (27)$$

$$\Phi_2(t) = 4\pi \left( \frac{f_0 + \frac{\Delta f}{2}}{c} \right) (R_0 + v_r t + a_r t^2) \quad (28)$$

The beat product between the two range compressed looks becomes equal then to:

$$S_b(t) = \mathfrak{L}_1(t)\mathfrak{L}_2^*(t) = \left| \text{rect} \left( \frac{t}{T} \right) \right|^2 e^{+j(\Phi_2(t) - \Phi_1(t))} \quad (29)$$

The beating frequency can then be calculated by differentiating the phase of the signal represented in (29), as follow:

$$\begin{aligned} f_b(t) &= \frac{1}{2\pi} \frac{\partial}{\partial t} \angle S_b(t) = 2 \frac{\Delta f}{c} (v_r + 2a_r t) = \\ &= \frac{\Delta f}{f_0} \left( 2 \frac{v_r}{\lambda} + 4 \frac{a_r}{\lambda} t \right) = \frac{\Delta f}{f_0} (f'_{DC} + f_{DR} t) \end{aligned} \quad (30)$$

where  $\angle S_b(t)$  is the phase term of (29).



# Appendix B

The cross-correlation function result in (3.27) is derived in this appendix. Let the signal in (31) represent the range compressed profile after the radial motion compensation:

$$S_R''(f, t) = W(f, t) e^{-j2\pi \frac{2f}{c} (R_0 + v_r t + a_r t^2)} e^{-j2\pi \frac{2f}{c} (\widehat{v}_r t + \widehat{a}_r t^2)} \iint \rho(\xi_1, \xi_2) e^{-j2\pi (\xi_1 \sin \theta(t) + \xi_2 \cos \theta(t))} d\xi_1 d\xi_2 \quad (31)$$

I will now consider the following assumption:

- $\widehat{v}_r = v_r$
- the target is composed of a single scatterer  $\rho(\xi_1, \xi_2) = \sigma_0 \delta(\xi_1, \xi_2)$ .
- The constant term  $R_0$  is neglected (it only causes a range shift in the ISAR image).

The signal in (31) can be approximated as follows:

$$S_R''(f, t) \approx \sigma_0 W(f, t) e^{-j2\pi \frac{2f}{c} \Delta a_r t^2} \quad (32)$$

where  $\Delta a_r = a_r - \widehat{a}_r$  is the acceleration estimation error. If I also assume that the range migration due to the residual quadratic term  $\Delta a_r$  is negligible, the frequency range  $f$  can be replaced by the carrier frequency  $f_0$  as follows:

$$S_R''(f = f_0, t) = S_R''(t) = \sigma_0 W(t) e^{-j2\pi \frac{2f_0}{c} \Delta a_r t^2} \quad (33)$$

It should be noted that by posing  $f = f_0$ , the signal dependence on the frequency variable can be neglected. The two sub-apertures can be derived by posing  $t_1 = T/4$  and  $t_2 = -T_{obs}/4$  and by defining two new signals:

$$S_{l1}(t) = \sigma_0 \text{rect} \left( \frac{t - T_{obs}/4}{T/2} \right) e^{-j2\pi \frac{2}{\lambda} \Delta a_r t^2} \quad (34)$$

$$S_{l2}(t) = \sigma_0 \text{rect} \left( \frac{t + T_{obs}/4}{T/2} \right) e^{-j2\pi \frac{2}{\lambda} \Delta a_r t^2} \quad (35)$$

It should be remarked that  $f_{DR} - f'_{DR} = \frac{2}{\lambda} \Delta a_r$  represents the residual Doppler rate. For the sake of convenience I will rename  $\delta = \frac{2}{\lambda} \Delta a_r$ . Moreover, since  $\delta T_{obs} \ll 1$ , the expression in (34) (35) can be approximated by their first order polynomial around the points  $t_1$  and  $t_2$ , as follows:

$$S_{l1}(t) \approx \sigma_0 \text{rect} \left( \frac{t - T_{obs}/4}{T_{obs}/2} \right) e^{-j2\pi\delta \frac{T_{obs}}{4} t} \quad (36)$$

$$S_{l2}(t) \approx \sigma_0 \text{rect} \left( \frac{t + T_{obs}/4}{T_{obs}/2} \right) e^{+j2\pi\delta \frac{T_{obs}}{4} t} \quad (37)$$

The two Doppler profiles can be obtained by FT of (36) and (37). The results can be shown below:

$$\Gamma_{l1}(f_d) = \frac{T_{obs}}{2} \sigma_0 \text{sinc} \left( \frac{f_d - \delta T_{obs}/4}{2/T} \right) e^{-j2\pi f_d \frac{T_{obs}}{4}} \quad (38)$$

$$\Gamma_{l2}(f_d) = \frac{T_{obs}}{2} \sigma_0 \text{sinc} \left( \frac{f_d + \delta T_{obs}/4}{2/T} \right) e^{+j2\pi f_d \frac{T_{obs}}{4}} \quad (39)$$

# Conclusions and Future Developments

In this thesis the following two relevant topics for radar remote sensing have been addressed:

- focusing of moving targets using the Inverse Synthetic Aperture Radar (ISAR) imaging technique;
- correction of the atmospheric propagation delay in multipass Differential Interferometry Synthetic Aperture Radar (DInSAR).

Related to the first issue, an ISAR autofocusing technique based on Doppler parameter estimation has been proposed. The estimation procedure is based on the re-use of Doppler parameter estimation tools available in classical SAR focusing and adapted to perform the ISAR focusing of moving targets. The proposed technique is a parametric methods: it has been assumed that the relative distance between a focusing point taken as reference on the target and the sensor can be approximated by a second order Taylor polynomial; the coefficients of the polynomial function physically represent the radial velocity and the radial acceleration of the target. The proposed method estimates the Doppler signal parameters: the Doppler centroid and the Doppler rate which are mathematically binding to the radial target motion parameters. The effectiveness of the proposed Doppler Parameter Estimation Algorithm (DPEA) has been proven by testing it with a real dataset and by comparing the results with a well-established ISAR autofocus technique: the Image Contrast Based Technique (ICBT), which carries out an exhaustive search aimed at improving a quality parameter: the contrast. The Doppler estimation parameters tool has been adopted firstly for refocusing moving targets in SAR images, and then for focusing moving target sensed by a static ISAR system. From a visual point of view and in terms of image contrast and entropy, the DPEA has shown very good results, which are comparable with those obtained by the ICBT. Furthermore, the DPEA seems to produce consistently a higher image peak value and it runs at lower computational cost, making it a strong candidate for a nearly real-time ISAR imaging. It is worth pointing out that the comparison

between the two techniques was carried out in the presence of maritime targets where the signal to clutter ratio is sufficiently high. In case of ground moving targets, the proposed Doppler Parameters Estimation Algorithm may suffer for the presence of strong clutter. This effect is however common to all available estimation techniques, including those based on contrast maximization, which have been used in this thesis as benchmark.

Possible future works may be the development of a cross-range scaling procedure and interferometric algorithms for the 3-D reconstruction of the targets. The cross-range scaling procedure consists of firstly estimating the angular variation  $\Omega$  of target with respect to the sensor, and, then scaling the target from the range-Doppler domain to the range-cross-range domain; this procedure is a necessary step before the target classification. As matter of fact, the cross-range scaling carries out the representation of the ISAR image in an homogenous spatial coordinates which allow to evaluate the distance between points belonging to the target to be measured and therefore allows the estimation of important geometrical features, such as target's size, shape position and dominant scatterers. The developments of interferometric algorithm is a very hard task but it will allow to evaluate the volume of the target and, therefore, it could be a very important feature especially for remote control system.

With regard to the second issue, it has been addressed the problem of using Global Positioning System (GPS) data to improve atmospheric phase delay compensation in multitemporal interferometric SAR data processing techniques. In fact, the new SAR sensors and constellation of sensors, characterized by low revisiting time, allow frequent acquisitions of interferometric data. Interferometric stacks useful for multipass differential analysis techniques are available on relatively short (with respect to the previous generation satellite) temporal interval. As matter of fact, seasonal variation of the atmospheric conditions can introduce contributions that cannot be compensated by using standard multipass interferometric techniques, that assume uncorrelated temporal behavior of the atmospheric delay. In this thesis, a new method for the robust assimilation of the GPS atmospheric delay measurements in the SAR data processing chain has been discussed and tested on real data acquired by the COSMO-SkyMed constellation over the Abruzzi region hit by the 2009 earthquake. Furthermore, it is based on a linear approximation of the atmospheric delay with respect to the height. Achieved results have confirmed the effectiveness of the proposed method.

Possible future works in this area are the testing of the proposed technique with further and more complicated datasets, f.i. by processing a dataset in presence of a larger altitude difference where the variation of the atmospheric pressure would produce a greater variation of the atmospheric propagation delay, or, a greater challenge could be applying the proposed technique in the presence of a volcanic island where the presence of the sea would determine a huge variation of the wet component of the atmospheric propagation delay. These case studies

would allow to better analyze the limitations of this technique and, therefore, to carry out the necessary improvements in order to ensure a better reliability of the measures, especially in areas characterized by high natural risks.



# Acknowledgments

I would like to express my special appreciation and thanks to my two advisors: Professor Dr. Ernesto Conte and Dr. Gianfranco Fornaro; you have been an excellent mentors for me and you strongly believed in me and in my research skills. I would like to thank you for encouraging my research and for allowing me to grow as a research scientist. Your advice on both research as well as on my career have been priceless. Thank you so much.

I would also like to thank Professor Dr. Marco Martorella and Dr. Paolo Braca for providing the ISAR data and your useful suggestion for this thesis.

I also want to thank Dr. Antonio Pauciullo, Professor Dr. Antonio De Maio, Dr. Augusto Aubry for your interesting, useful hints and your brilliant comments, thanks to you.

I would also like to thank my working roommates in IREA: Diego, Virginia and Simona, who supported and encouraged me to strive towards my goal and also shared with me this amazing experience.

I want also to thank all other IREA colleagues: Pasquale, Antonio, Giovanni, Chandra, Claudio, etc.. that make me smile, especially in difficult times.

A special thanks to my family. Words cannot express how grateful I am to my mother, my father my brother and my sister-in-law for all of the sacrifices that you have made on my behalf. Your prayer for me was what sustained me thus far.

A special thank also to all my friends and my family-in-law who have been close to me during this hard task.

At last but not least, as Latins said: “Dulcis in fundo”, I would like express appreciation to my beloved girlfriend Marina who spent all nights and days encouraging me and she was always my support in the moments when there was no one to answer my queries, your words and smiles drove me to the end of this hard work.

Thank you my love, “I did it!”.



# Short form Curriculum Vitae

Carlo Noviello was born in Naples, Italy, on October 31, 1982. He received the M.S. degree in telecommunication engineering from the University of Naples Federico II, Naples, Italy, in 2011.

Since 2012, he has been collaborating with the Institute for Electromagnetic Sensing of the Environment (IREA), National Research Council (CNR), Naples, Italy.

His research interests include statistical signal processing, with emphasis on inverse and direct synthetic aperture radar processing.

## List of journal publications:

- **C. Noviello**, G. Fornaro, and M. Martorella, “Focused SAR Image Formation of Moving Targets based on Doppler Parameter Estimation,” *IEEE Transactions on Geoscience and Remote Sensing*, vol. 53, no. 6, pp. 3460-3470, June 2015.
- G. Fornaro, N. D’Agostino, R. Giuliani, **C. Noviello**, D. Reale, and S. Verde, “Assimilation of GPS-Derived Atmospheric Propagation Delay in DInSAR Data Processing,” *IEEE Journal of Selected Topics in Applied Earth Observations and Remote Sensing*, vol. 8, no. 2, pp. 784-799, Feb 2015.

## List of conference publications:

- **C. Noviello**, G. Fornaro, M. Martorella, and D. Reale, “ISAR add-on for focusing moving targets in very high resolution spaceborne SAR data,” *Proc. of the 2014 IEEE International Geoscience and Remote Sensing Symposium (IGARSS) Conf.*, pp.926-929, Quebec City, Canada, 13-18 July 2014.

- **C. Noviello**, G. Fornaro, M. Martorella, and D. Reale, "A Novel approach for Motion Compensation in ISAR System," *Proc. of the 10th European Conference on Synthetic Aperture Radar*, pp.1-4, Berlin, Germany, 3-5 June 2014.
- N. D'Agostino, G. Fornaro, R. Giuliani, **C. Noviello**, D. Reale, and S. Verde, "GPS Aided Atmospheric Phase Delay Mitigation In Differential SAR Interferometry: Experiences From The 2009 L'Aquila Earthquake", *Proc. of the IEEE 2013 International Geoscience and Remote Sensing Symposium (IGARSS) Conf.*, pp. 1853-1856, Melbourne, Australia, 21-26 July 2013.
- **C. Noviello**, and G. Fornaro, "Inverse and Direct Synthetic Aperture Radar Data Processing," *Proc. of the 2012 IEEE International Gold Remote Sensing Conf.*, pp.134-136, Rome, Italy, 4-5 June 2012.

